A synthesis of observations of aerosol-cloud interactions over the pristine, biologically active Southern Ocean and the implications for global climate model predictions.

Isabel L. McCoy

A dissertation

submitted in partial fulfillment of the

requirements for the degree of

Doctor of Philosophy

University of Washington

2020

Reading Committee:

Robert Wood, Chair

Christopher S. Bretherton

Roger Marchand

Program Authorized to Offer Degree:

Atmospheric Sciences

University of Washington

Abstract

A synthesis of observations of aerosol-cloud interactions over the pristine, biologically active Southern Ocean and the implications for global climate model predictions.

Isabel L. McCoy

Chair of the Supervisory Committee:
Professor Robert Wood
Department of Atmospheric Sciences

The change in planetary albedo due to aerosol-cloud interactions (aci) during the industrial era is the leading source of uncertainty in inferring Earth's climate sensitivity to increased greenhouse gases from the historical record. Examining pristine environments such as the Southern Ocean (SO) helps us to understand the pre-industrial (PI) state and constrain radiative forcing associated with aci (RFaci). Cloud droplet number concentration (N_d) is a key aci indicator variable. Using global climate models (GCMs), this study finds that the hemispheric contrast in N_d of liquid clouds between the pristine SO and the polluted Northern Hemisphere observed in the present-day (PD) can be used as a proxy for the increase in N_d from the PI. The hemispheric difference

constraint and MODIS satellite observations suggest that PI N_d may have been higher than previously thought and provide an estimate of RFaci between -1.2 and -0.6 Wm^{-2}.

Southern Ocean liquid clouds can reach N_d levels comparable to the polluted outflows of East Asia and the United States despite persistent precipitation depletion associated with mid-latitude storm systems. This high N_d in one of the most pristine regions on Earth motivates further investigation of the mechanisms driving N_d in the real world and better inclusion of the mechanisms in models. In this study, aerosol and cloud microphysical data from the 2018 Southern Ocean Cloud Radiation Aerosol Transport Experimental Study (SOCRATES) aircraft campaign are used to identify a novel and potentially important mechanism missing or poorly represented in models: production of new particles through synoptic uplift. The small, Aitken mode particles produced in this process dominate the free tropospheric atmosphere in the summertime SO. We find it is likely that entrainment of free tropospheric Aitken aerosols is a leading contributor to sub-cloud cloud condensation nuclei and thus may be a key control on N_d. The free tropospheric Aitken reservoir may maintain the persistently high N_d observed across the SO against precipitation depletion. Finally, our observational comparisons with nudged Community Atmosphere Model (CAM6) hindcasts highlight large aerosol number and composition discrepancies that may significantly and negatively impact the ability of current climate models to capture aci in pristine, PI environments.

TABLE OF CONTENTS

LIST OF FIGURES

ACKNOWLEDGEMENTS

I wish to extend my heartfelt thanks to my advisor, Rob Wood, who has been an inspiring mentor, a thoughtful advocate, and a supportive friend for as long as I have known him. Thank you for helping me to find my scientific voice, for giving me the freedom and support to pursue my own ideas, and for making graduate school and research a lot of fun. I would also like to thank Chris Bretherton, who has been like a second advisor to me and has changed how I think about and approach scientific problems. Thank you for helping to foster a supportive and scientific environment, both at UW and in the field. I additionally owe my thanks to my committee members: Roj Marchand, Twit Conway (GSR), Frida Bender, Dargan Frierson, and Dennis Hartmann. I have valued our invigorating scientific discussions over the years and the opportunity to learn from all of you. I also owe a debt of gratitude to Dave Raymond, Tom Ackerman, and, especially, Daniel McCoy for encouraging me to pursue Atmospheric Sciences.

Thank you to my many collaborators and co-authors who have taken the time to help me in our pursuit of knowledge and to expand my scientific ideas. I also owe my thanks to the funding agencies who have supported my education and research over the last many years: the American Meteorological Society through their Graduate Fellowship, the National Science Foundation through their Graduate Research Fellowship Program and their support of the SOCRATES campaign, and the National Aeronautics and Space Administration through various grants.

I would not have overcome the struggles that one encounters almost every day in graduate school without the help of a few special people: Marc Michelsen, the 7th floor super-computer and

coding guru; Peter Blossey and Matt Wyant, experts on the inner workings of clouds and codes who also made the time to talk to me about life whenever I needed it; and my office mates, Pornampai (Ping-Ping) Narenpitak and Kuan-Ting (Andy) O, my lifesavers throughout the whole graduate school process who were always ready to have in-depth, philosophical discussions about science and the peculiarities of the world at any moment. I also owe my thanks to the Wood group, especially Ryan Eastman and Sam Pennypacker, and the cloud community, especially my SOCRATES-compatriots. My conversations with you all, both scientific and personal, enriched my time at UW. The atmospheric science department has been like a second family to me. I am indebted to the many friends I have made while part of this community, their support and good cheer bolstered me throughout this journey.

Finally, my deepest thanks go to my family. Thank you to my parents, for supporting my dreams, being there for me in the highs and lows, and for encouraging me to pursue science from the very beginning. And to my brother, who will always be my best and most senior co-author and friend. Thank you for setting me on this path and for being a constant inspiration. Here's to the rest of our careers working to understand clouds and climate together.

DEDICATION

To my family, for believing in me, and to the many explorers who came before me and strived to elucidate the mysteries of the Southern Ocean.

Chapter 1. INTRODUCTION

The Southern Ocean (SO) plays a key role in understanding our past and present climate. Because of the pristine nature of its aerosol, this region is the closest present-day (PD) analog we have to the pre-industrial (PI) state [*Hamilton et al.*, 2014]. The change in reflected shortwave radiation between the PI and the PD due to anthropogenic emissions of aerosols, known as aerosol radiative forcing (which includes aerosol cloud interactions), is the leading cause of uncertainty in inferring climate sensitivity from the observational record [*Andreae et al.*, 2005; *Forster*, 2016]. As a community, we strive to understand the PI environment so that we can both estimate the change in climate due to industrialization and improve the accuracy of our predictions for our future climate under the influence of global warming.

The influence of anthropogenic and biomass burning aerosol is mostly negligible over SH oceans, particularly in the summertime, leaving sea spray and biologically sourced aerosols as the primary contributors to the aerosol budget. Aerosols fall roughly into three modes: nucleation or Aitken (diameters between 0.005 and 0.1 μm), accumulation (diameters between 0.1 and 2.5 μm), and coarse (diameters > 2.5 μm) [*Seinfeld and Pandis*, 2006]. The number concentration of particles in the SO is dominated by Aitken mode and small accumulation mode particles while the mass is dominated by coarse mode particles [*Ayers et al.*, 1997].

In the summertime SO and other biologically active pristine marine regions, phytoplankton emissions of dimethyl sulfide (DMS) play a key role in both production of Aitken mode particles and growth of CCN [*Charlson et al.*, 1987; *Ayers and Gras*, 1991; *Ayers et al.*, 1997; *Ayers and Gillett*, 2000]. CCN grow from coagulation of smaller Aitken or accumulation mode particles; from vapor deposition onto preexisting particles [*Seinfeld and Pandis*, 2006]; and from the

addition of non-sea-salt sulfate derived from aqueous-phase oxidation of DMS products in cloud droplets that subsequently evaporate, contributing to the accumulation mode budget [*Hobbs*, 1971; *Charlson et al.*, 1987].

Accumulation mode aerosols, the main cloud condensation nuclei (CCN), change the radiation reflected back to space by liquid clouds in two ways:

I. by modulating the number concentration of cloud droplets (N_d), which changes cloud reflectivity even without any changes to cloud macrostructure [*Twomey*, 1977],

II. by changing N_d, cloud microphysical processes are altered that have various impacts on cloud macro-physical properties (e.g., cloud cover or liquid water content [*Albrecht*, 1989]).

These effects are referred to as radiative forcing due to aerosol-cloud interactions (RF_{aci}) and cloud adjustments to aerosol, respectively [*Boucher*, 2013]. The combined forcing from aerosol-cloud adjustments and RF_{aci} is referred to as the effective radiative forcing due to aci (ERF_{aci}). The net aerosol forcing is the sum of ERF_{aci} and a similar quantity for aerosol direct interactions, ERF_{ari}.

A recent survey identified the dominant contributor to the uncertainty in global-mean aerosol radiative forcing as aerosol-cloud interactions (aci) in liquid clouds [*Bellouin*, 2019]. RF_{aci} is non-linearly dependent on the change in N_d over the industrial period [*Carslaw et al.*, 2013]. This is because clouds in a pristine, PI state are more susceptible (i.e. have a larger increase in cloud albedo) to an increase in aerosol than clouds in PD, polluted environments [*Carslaw et al.*, 2013]. Natural aerosols, or aerosols in the PI state, are the largest cause of uncertainty in aerosol forcing over the industrial period because the cloud response to industrialization is very sensitive to this initial, pristine state [*Carslaw et al.*, 2013; *Regayre et al.*, 2014]. While we cannot measure

PI aerosol, we *can* examine aerosol-cloud interactions in the few remaining pristine locations in the PD in order to reduce the associated uncertainty in indirect and thus total radiative forcing.

In Chapter 2, I focus on providing an observational constraint for the change in N_d and RF_{aci} with industrialization. The forcing due to aerosol-cloud adjustments is uncertain in both sign and magnitude [*Gryspeerdt et al.*, 2016; *Malavelle et al.*, 2017; *Toll et al.*, 2017; *Sato et al.*, 2018; *Bender et al.*, 2019; *Gryspeerdt et al.*, 2019; *Toll et al.*, 2019], but is expected to scale with changes in N_d (e.g. big changes in N_d will correspond with big adjustments) [*Bellouin*, 2019]. Narrowing the possible range of changes in N_d and resulting RF_{aci} will narrow uncertainty in ERF_{aci} and, by extension, improve our inference of climate sensitivity [*Andreae et al.*, 2005; *Bellouin*, 2019]. The PD N_d is observable, but we must infer PI N_d using other means. I use the pristine Southern Hemisphere (SH) [*Hamilton et al.*, 2014] as a proxy for the PI and examine the contrast between the SH and the polluted Northern Hemisphere (NH) to estimate the anthropogenic perturbation to N_d and what that tells us about RF_{aci}. I further highlight the complexity inherent in the aci occurring in the SO from the interplay of aerosol sources and sinks. A lack of this complexity in GCMs may be leading to the under estimation of N_d and the over estimation of RF_{aci}. This work is summarized in *McCoy et al.* [2020].

In Chapter 3, I expand my examination of the complex mechanisms involved in SO aci using observations from the 2018 Southern Ocean Clouds Radiation and Aerosol Transport Experimental Study (SOCRATES) campaign. SOCRATES sampled clouds and aerosols in the cold sectors of Southern Ocean cyclones between 45-62°S during austral summer. In SO cyclone cold sectors, global weather and climate models tend to simulate low clouds that do not reflect enough radiation to space [*Bodas-Salcedo et al.*, 2012; *Williams et al.*, 2013; *Bodas-Salcedo et al.*, 2014; *Bodas-Salcedo et al.*, 2016]. Excessive glaciation of mixed-phase clouds is one explanation,

but another contributor may be biases in CCN concentrations, N_d concentrations, and aci driving these populations [*Bodas-Salcedo et al.*, 2019; *Revell et al.*, 2019; *McCoy et al.*, 2020].

The marine boundary layer (MBL) in SO cyclone cold-sectors is a regime in which large concentrations of small aerosols [*Covert et al.*, 1996] with sulfuric acid composition signatures have been observed, consistent with new particles observed in the free troposphere (FT) [*Weber et al.*, 2001]. These FT aerosols are likely essential for driving the MBL SO CCN setting N_d [*Korhonen et al.*, 2008] but observational evidence of their impact is limited. My work finds observational support for: i) widespread recent particle formation occurring in the summertime free tropospheric air due to particle generation through synoptic uplift, ii) linkages between FT volatile, sulfuric acid particles and the primarily sulfur-based composition of influential sub-cloud CCN, and iii) the trivial sea-salt aerosol contributions to the sub-cloud aerosol controlling N_d in the real world. It is likely, based on these observations, that a buffering mechanism occurs in the summertime SO involving the FT reservoir of small, Aitken aerosol acting as a CCN source and maintaining high N_d despite notable precipitation depletion. Lack of aerosol production and aci pathways in current models (particularly the nudged CAM6 model tested in this study) may be contributing to biases in pristine N_d and thus RF_{aci}. This work is summarized in *McCoy and Toohey* [2020 submitted].

Chapter 2. CONSTRAINING AEROSOL FORCING WITH THE HEMISPHERIC CONTRAST IN CLOUD MICROPHYSICAL PROPERTIES

2.1 INTRODUCTION

Previous studies have discussed the hemispheric contrast in cloud properties created by anthropogenic aerosol emissions in the NH. The effective radius of droplets (r_e) is smaller in the NH than in the SH [*Han et al.*, 1994; *Feng and Ramanathan*, 2010]. *Feng and Ramanathan* [2010] found that a chemical transport model driven by reanalysis meteorology was able to produce a difference in N_d between the NH and SH consistent with hemispheric contrasts in satellite retrievals of r_e and cloud optical depth (τ). *Boucher and Lohmann* [1995] used the hemispheric difference in r_e to evaluate the robustness of the RF_{aci} simulated in instances of the LMD and ECHAM global climate models (GCMs) when a prescribed relationship between sulfate mass and N_d was implemented. As in these pioneering works, we use hemispheric differences in cloud microphysics to evaluate modeled aerosol-cloud interactions. Our approach differs from previous work in the following ways. First, r_e, which can be retrieved (with some important caveats) by remote sensing, is a function of the number concentration of cloud condensation nuclei (CCN), the width of the droplet size distribution, and the liquid water content of clouds. The differences in cloud liquid water content between hemispheres [*Feng and Ramanathan*, 2010; *Seethala and Horvath*, 2010] will weaken any r_e-based constraint on hemispheric CCN difference. N_d can be calculated from r_e and τ retrievals by satellite visible and near-infrared imagers. Including both r_e and τ helps to account for cloud liquid water contributions as outlined in *Grosvenor et al.* [2018b]. We use this calculated N_d to constrain RF_{aci} because it is the key variable linking cloud

microphysical and aerosol properties [*Wood*, 2012]. Second, we analyze output from a large collection of GCMs designed to quantify aerosol forcing alongside a million-member ensemble from a single model that samples uncertainty in 26 aerosol processes [*Yoshioka et al.*, 2019]. This enables us to robustly quantify and then constrain the uncertainty in the change in N_d and RF_{aci}.

The N_d derived from satellite retrievals has been shown to be reasonably unbiased in comparison with aircraft measurements [*Painemal and Zuidema*, 2011; *Painemal et al.*, 2012; *Bennartz and Rausch*, 2017; *Grosvenor et al.*, 2018b; *McCoy et al.*, 2018; *Witte et al.*, 2018] and to agree well in both the remote Southern Ocean (SO) [*Ahn et al.*, 2018] and the NH [*McCoy et al.*, 2018]. Biases between *in situ* and N_d calculated based on Moderate Resolution Spectroradiometer (MODIS) data are on the order of 1-20 cm^{-3}, depending on geographic region and boundary-layer stratification, and systematic bias does not scale strongly with N_d [*Bennartz and Rausch*, 2017; *Ahn et al.*, 2018; *McCoy et al.*, 2018]. The hemispheric contrast in N_d is a difference, so this should moderate the effects of any systematic biases in N_d. Our understanding of the relationship between hemispheric contrast in N_d and anthropogenic perturbations to N_d is facilitated by insight into the uncertainty in the PI atmosphere provided by GCMs. We combine analysis of structural model uncertainty from CMIP5 models participating in the Aerocom phase II project [*Ghan et al.*, 2016] and several simulations made during the development of the atmosphere-only climate model configuration, HadGEM3-GA7.1 [*Mulcahy et al.*, 2018] with analysis of parametric uncertainty within a perturbed parameter ensemble (PPE) in HadGEM3-GA4-UKCA. The PPE is based on 235 individual simulations in which combinations of 26 aerosol processes and emissions were perturbed [*Yoshioka et al.*, 2019]. The output from these 235 simulations was used to train Gaussian process emulators to enable a million model variants to be generated, facilitating more robust statistical analysis [*Watson-Parris et al.*, 2020]. We show that

uniting this growing confidence in satellite-derived N_d with state-of-the-art modelling experiments directed at evaluating aci in warm clouds allows us to bound anthropogenic perturbations to N_d and RF_{aci} over the industrial period.

2.2 Materials and Methods

In this paper we contrast N_d predicted by GCMs with satellite data and *in situ* observations. N_d is always presented in-cloud, not averaged across cloudy and cloud-free regions. The central remote sensing data set used in this study is MODIS Aqua C5.1 utilizing the 3.7 μm channel [*King et al.*, 2003] during the period 2003-2015 [*Grosvenor*, 2018]. The calculation of N_d from MODIS retrievals of cloud optical depth (τ) and cloud droplet effective radius (r_e) is not always reliable. The retrieval criteria presented in [*Grosvenor and Wood*, 2014] are used to select for times and places consistent with the assumptions made in the retrievals of τ and r_e from satellite radiances (which, among other restrictions, limits data to confidently cloudy pixels and excludes cloud edge pixels) as well as in the calculation of N_d resulting from these quantities. Briefly, these criteria are that solar zenith angles are below 65°; cloud tops are within 3.2 km of the surface; and liquid cloud fractions are greater than 80% in a 1°x1° region [*Grosvenor and Wood*, 2014; *Grosvenor et al.*, 2018a; *Grosvenor et al.*, 2018b]. Data are filtered using these criteria based on individual Level-2 swaths (as opposed to daily averages) that have been averaged to 1°x1°. The majority of observations occur in the sub-tropical cloud decks and the mid-latitudes (Figure SI 2- 1). While this does not impact the calculation for the hemispheric contrast (which uses the consistently sampled 30-60° bands), it may influence the zonal comparisons in the sub-tropics (Figure 2-1 a and b).

Satellite derived N_d values in the SO are evaluated using observations from a variety of campaigns and ground stations. *In situ* CCN observations from McMurdo Station [*Liu et al.*, 2018]

and King Sejong Station [*Kim et al.*, 2017] are drawn from the reported monthly and seasonal mean values in the literature. MODIS N_d for these regions is shown averaged across a 4° box centered at the respective stations (Figure SI 2- 6a). RITS total aerosol concentration was obtained from data provided to the Global Aerosol Synthesis and Science Project (GASSP) [*Reddington et al.*, 2017]. ORCAS N_d data measured between the surface and 3 km is obtained from the Earth Observing Laboratory (EOL) at the National Center for Atmospheric Research (NCAR) [*Laboratory*, 2018]. Sea ice cover was interpolated to the ORCAS flight track. The sea ice cover used in this analysis was from the Operational Sea Surface Temperature and Sea Ice Analysis (OSTIA) provided with the MERRA2 data product [*Donlon et al.*, 2012]. The N_d calculated by MODIS is sorted as a function of sea ice vs. open water and compared to similarly separated observations from ORCAS. For the comparison in Figure SI 2- 6d, MODIS N_d from 2003-2015 was restricted to only the days of the year and 1° regions where ORCAS measured N_d.

The GCM N_d examined in this study is provided by models participating in the Aerocom phase II indirect experiment [*Ghan et al.*, 2016]; sensitivity experiments conducted in the development of HadGEM3-GA7.1 [*Mulcahy et al.*, 2018]; and a perturbed parameter ensemble (PPE) within HadGEM3-GA4-UKCA [*Yoshioka et al.*, 2019]. The Aerocom phase II models considered are CAM5, CAM5-CLUBB, CAM5-MG2, CAM5-CLUBB-MG2, ECHAM6.1.0-HAM2.2, SPRINTARS, and SPRINTARSKK. The model variants of the UM examined in *Mulcahy et al.* [2018] shown here are GA7.0, GA7.1, GA7.0_dms (DMS in sea water set to 170% of climatology), GA7.0_act (changes to the activation scheme), and GA7.0_comb (GA7.1 with no cloud tunings). Following standard experiment protocols for determining the anthropogenic aerosol ERF [*Myhre et al.*, 2013; *Andrews*, 2014], the model simulations and subsequent change in N_d, do not account for climate-driven changes in natural aerosol emissions (e.g. wind speed

changes) over the PI to PD period that may influence the N_d concentration in the Southern Ocean [*Korhonen et al.*, 2010].

Multi-model ensembles (such as Aerocom) are invaluable for quantifying the magnitude of differences between models due to choices of physical process representations. However, this type of ensemble neglects the uncertainty within individual models. Perturbed parameter ensembles (PPEs) provide a useful means of quantifying single model uncertainty [*Collins et al.*, 2010], however they neglect uncertainty caused by particular choices of process representations. We represent single model uncertainty using output from a PPE of the HadGEM-GA4-UKCA global climate model. In this PPE, 26 aerosol process, emission, and deposition parameters were simultaneously perturbed, allowing for assessment of a broad range of model behavior (Figure SI 2- 4). The PPE contains 235 model variants, each with a unique combination of the parameter values. Each PPE member simulated PD N_d resolved in space and time, PI global-mean N_d, and top-of-the-atmosphere radiative fluxes (used to calculate RF_{aci}). Horizontal winds and temperature fields were relaxed [*Telford et al.*, 2008] towards 2008 meteorology from the European Centre for Medium-Range Weather Forecasts (ECMWF) ERA-Interim reanalyses and forced with year 2008 anthropogenic aerosol emissions from the MACCity emission inventory [*Granier et al.*, 2011]. To quantify uncertainty in changes over the industrial period, each of the 235 simulations has a partner simulation with identical parameter values, but with anthropogenic emissions from 1850 prescribed instead of PD emissions. A double call configuration to the radiation codes is used to calculate radiative fluxes in the PPE with and without simulated aerosols (see section 2.4.1 in *Yoshioka et al.* [2019] for more detail). In this way the model was configured so that the first indirect effect of aerosols could be quantified in the absence of aerosol-cloud adjustments. Variations in N_d over the ensemble are caused entirely by differences in aerosol size distributions

due to combinations of the 26 parameter values. We use the 235 member PPE to build statistical emulators of N_d and RF_{aci}. A sample of one million model variants (parameter combinations) is drawn from the emulator for each variable [*Watson-Parris et al.*, 2020]. Creation of the emulator assumes trapezoidal priors developed using expert solicitation [*Yoshioka et al.*, 2019]. This makes the sample members more centralized in the multi-dimensional parameter space compared to the uniform priors assumed in earlier works [*Johnson et al.*, 2018; *Regayre et al.*, 2018; *Johnson et al.*, 2019; *Regayre et al.*, 2019]. If these uniform priors, which assume the entire range for all parameters are equally likely, are used in our analysis instead, the range of possible RF_{aci} consistent with estimated $\Delta N_{d(NH-SH)}$ is between -1.4 and -0.5 Wm^{-2} (Figure SI 2- 9).

Hemispheric contrast in N_d ($\Delta N_{d(NH-SH)}$) is calculated as the difference in the annual mean of the area-weighted N_d concentrations over oceans 30-60°N and 30-60°S. N_d data in months and latitudes where MODIS retrievals are unavailable are removed from the GCM data before calculating the hemispheric contrast to avoid biases in comparing estimates from MODIS and modeled N_d. The region 30°S-30°N is excluded because the retrieval of N_d by MODIS in convection is less robust [*Grosvenor et al.*, 2018b]. The random uncertainty in N_d calculated from MODIS is relatively small once it is averaged across a 30° latitude band [*Grosvenor et al.*, 2018b]. The 95% confidence on the hemispheric contrast was calculated by taking the standard error in the annual hemispheric contrast in the years 2003-2015 and assuming a normal distribution using each yearly average as a sample. Evaluation of N_d calculated from MODIS data has shown small systematic error [*Grosvenor et al.*, 2018b]. Further, by examining the difference between hemispheres, we expect any systematic bias in the MODIS retrievals will be reduced.

Finer temporal matching between MODIS and modeled N_d is not possible given only monthly model output is currently available. We hope this study makes the case for routinely

producing N_d as a model variable which will increase the availability of higher temporal output for later studies. This would facilitate more detailed model-observation comparisons in the future. For example, it would enable testing of model biases associated with dynamical regimes such as have been identified for radiation biases associated with cyclone cold sectors [*Williams et al.*, 2013; *Bodas-Salcedo et al.*, 2014]. In the real world, N_d does not appear to vary significantly across dynamical regimes [*McCoy et al.*, 2018] but further examination is warranted of both how broadly this applies and how models capture this behavior.

The best fit line relating $\Delta N_{d(NH-SH)}$ to $\Delta N_{d(PD-PI)}$ and RF_{aci} was calculated using least-squares regression on the PPE sample members. The prediction band on the best fit line was used to quantify the possible range of N_d and RF_{aci} because all PPE sample members are considered to be equally valid representations of the real world. The prediction band about the best fit line was calculated by fitting the 95th percentile of PPE members in 30 quantiles of hemispheric contrast.

To quantitatively estimate the impact of marine boundary layer (MBL) precipitation on the seasonal climatology of N_d over the SO, we use the source and sink aerosol budget model developed in [*Wood et al.*, 2012], hereafter W12. The model was developed for use over those parts of the global oceans where cloud condensation nuclei concentration loss rates are driven primarily by coalescence scavenging in MBL cloud systems [*Wood*, 2006a]. Modeled mean MBL CCN estimates from the model appropriate for describing the monthly mean climatology of N_d were shown to agree well with the observed N_d off the coast of Chile [*Wood et al.*, 2012] and between California and Hawaii [*Mohrmann et al.*, 2018].

We apply the W12 model to estimate the impact of MBL cloud precipitation on the summertime meridional gradient of N_d over the SO. Using the equilibrium number concentration from the model (W12 eq. 2), we construct a ratio between N_d with precipitation loss and N_d

computed with no precipitation loss. This is found to be inversely proportional to the precipitation rate:

$$\frac{N_d(precip)}{N_d(no\ precip)} = \left(1 + \frac{hKP_{CB}}{Dz_i}\right)^{-1} \qquad eq.\ 2\text{-}1$$

As in W12, h is the cloud thickness (derived from MODIS LWP using the adiabatic assumption); K is a constant [*Wood*, 2006b]; P_{CB} is cloud base precipitation rate derived from CloudSat [*Wood et al.*, 2012]; D is the surface divergence for low cloud scenes; and z_i is the planetary boundary layer depth. Because of the difficulty isolating surface divergence for low cloud scenes over the midlatitude storm tracks, we note that $D*z_i$ is the subsidence rate at cloud top, which we assume to be equal to the entrainment rate, which we estimate as 4 mm/s, consistent with typical values found in low clouds in the subtropics and midlatitudes. We estimate the coalescence-scavenging sink using the CloudSat-derived precipitation rate product [*Haynes et al.*, 2009]. This product attempts to estimate precipitation from all cloud systems, not only those arising from MBL clouds.

Previous applications of this model examined the eastern ocean subtropical systems [*Wood et al.*, 2012; *Mohrmann et al.*, 2018] where precipitation was primarily derived from low cloud systems. In contrast, across the SO there is considerably more precipitation emanating from deeper precipitating systems [*Wang et al.*, 2015]. This is accounted for by only considering CloudSat precipitation estimates with detectable echo tops below 3 km altitude. This attempts to ensure that only precipitation that has a significant contribution to the coalescence scavenging of MBL CCN is used as input to the CCN and N_d budget models. This choice is based on data from the Azores, which straddles the boundary between the subtropics and the midlatitudes (~40ºN), showing that between 15% and 30% of all precipitation reaching the surface originated from clouds with tops below 3 km [*Wood et al.*, 2015]. Similarly, between 30°S and 70°S, with weak dependence on

latitude, we find that 15-35% of all precipitation reaching the surface originates from clouds with tops below ~3 km (Figure SI 2- 8a-e).

The observational and remote sensing datasets supporting this analysis are available either in previously published works or at supporting websites. This includes the central dataset in our analysis, the multi-year MODIS N_d product which is hosted at the Centre for Environmental Data Analysis [*Grosvenor*, 2018]. All relevant citations and supporting sites are noted in the descriptions of these datasets in the Materials and Methods section. Aerocom model simulations are similarly available from their support website (https://aerocom.met.no). Raw simulation output data from the HadGEM-UKCA PPE ensembles are available from the JASMIN data infrastructure (http://www.jasmin.ac.uk). Some of the climate-relevant fields are derived and stored for all ensemble members and made available as a community research tool.

2.3 RESULTS

2.3.1 *Definition and Application of a Hemispheric Contrast*

Comparing satellite-derived, maritime N_d from MODIS with Aerocom phase II and HadGEM3-GA7.1 development simulations reveals major discrepancies between GCMs and MODIS N_d in the PD. GCMs consistently overestimate tropical and NH midlatitude N_d (Figure 2-1a, b). They consistently underestimate summertime N_d in the SH mid-latitude (30-60°S) (Figure 2-1a). GCMs also underestimate summertime marine N_d poleward of 60^o in both hemispheres, especially in the SH where MODIS N_d increases significantly towards Antarctica (Figure 2-1a, Figure 2-2a). Intriguingly, the mean MODIS summertime N_d near Antarctica is close to values found in continental outflows from heavily industrialized regions [*McCoy et al.*, 2018]. The remote SO is among the most pristine regions in the world [*Hamilton et al.*, 2014] with emissions from ocean biology controlling aerosol and N_d seasonality [*Ayers and Gras*, 1991; *McCoy et al.*, 2015].

The NH mid-latitude has both polluted and pristine aerosol influences. The magnitude of the summertime Arctic MODIS N_d increase is smaller than the summertime Antarctic increase, possibly due to the closer proximity to large continental and anthropogenic sources of aerosol in the NH (and the non-linear relationship between CCN and N_d [*Carslaw et al.*, 2013]). While more complex to disentangle, the natural sources of NH aerosol have a significant seasonal cycle driven by ocean biology [*O'Dowd et al.*, 2004; *Sanchez et al.*, 2018; *Zheng et al.*, 2018]. These high summertime mid- and high-latitude values in the SH and high-latitude values in the NH are not captured by GCMs, but, as discussed below, appear in *in situ* observations of cloud condensation nuclei (CCN) and N_d, which supports its appearance in satellite-derived N_d.

PPE model members show similar discrepancies compared with MODIS although NH values are less overestimated on average (Figure SI 2- 4). Some of the PPE model members are also able to capture high SO N_d (although near Antarctic values are still deficient). Because there are some parameter combinations in the PPE that are able to produce a sufficiently near-real world simulation to overlap with observations, we will be able to use the MODIS N_d hemispheric contrast as a constraint on the PPE later on in our study. Ideally, future GCMs will produce simulated N_d in closer correspondence to the real-world and will be viable to use with this hemispheric contrast constraint.

Note that MODIS N_d observations are uniformly distributed in the mid-latitudes, but they are more concentrated in the cloud decks to the west of continents in the sub-tropics (Figure SI 2-2). This may have some influence on the disagreement in the sub-tropics although the significant N_d in these cloud decks [*McCoy et al.*, 2018] would be expected to bias observed N_d high rather than low. One would further expect that this would bring observations into closer agreement with the high biased GCMs (Figure 2-1a, b) if the model-observation disagreement was *only* from a

discrepancy in observation versus model cloud sampling. Thus, it is likely there are deeper, underlying model biases responsible for the GCM overestimation in this region.

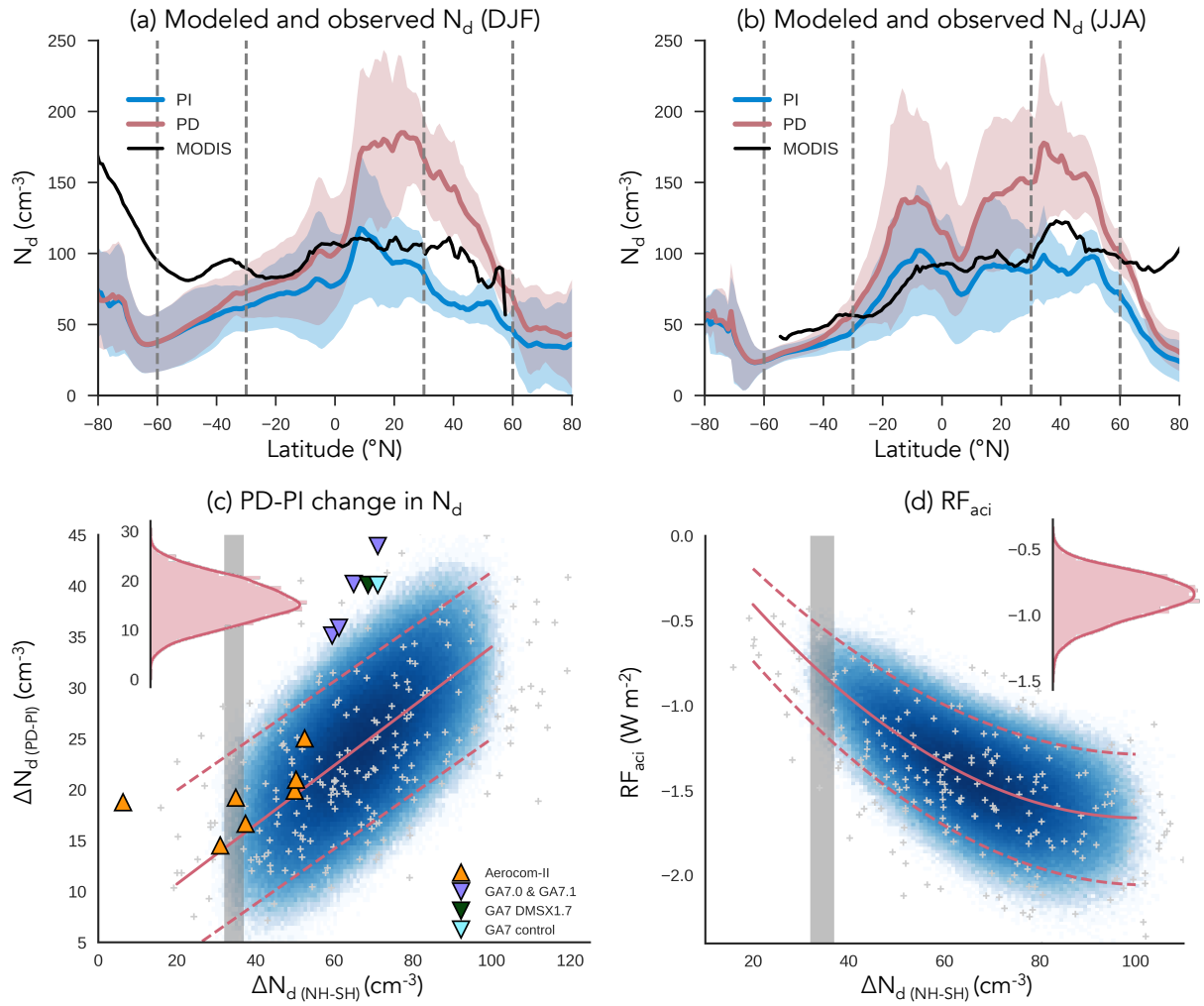

Figure 2-1 *Constraints on aerosol-cloud interactions (aci) from satellite estimated hemispheric contrast in N_d over oceans ($\Delta N_{d(NH-SH)}$). (a,b) Oceanic Pre-Industrial (PI, blue) and Present Day (PD, red) N_d modeled by Aerocom-II models and HadGEM3-GA7.1 development models. Thick lines show the multi-model mean, corresponding shading shows the standard deviation across models. Data from DJF and JJA are shown separately in (a) and (b). In Southern Ocean winter the Aerocom-II NCAR models are missing data due to lack of low, liquid cloud, leading to discontinuity in the multi-model mean at 70°S. Zonal means from each model are shown in Figure SI 2- 3. $\Delta N_{d(NH-SH)}$ is calculated as the difference in annual, area-weighted mean N_d over the ocean between 30-60°N and 30-60°S (averaging boundaries shown as vertical dashed lines). (c) Change*

in oceanic N_d between the PI and PD ($\Delta N_{d(PD-PI)}$) as a function of $\Delta N_{d(NH-SH)}$ in PPE members (gray crosses for individual model members, blue shading for N_d values sampled from a statistical emulator), in Aerocom-II (orange triangles), and HadGEM-GA7.1 development models (purple, blue, and dark green triangles). HadGEM-GA7.0 with enhanced DMS is shown in dark green and the control HadGEM-GA7.0 in blue. The linear fit to the PPE data and 95% prediction bands on the fit are shown as red solid and dashed lines. The 95% confidence on the interannual range of $\Delta N_{d(NH-SH)}$ estimated by MODIS is shown in gray. (d) as in (c) but showing the relation between RF_{aci} and the hemispheric contrast calculated from the PPE sample members along with a second-order polynomial fit between $\Delta N_{d(NH-SH)}$ and RF_{aci}. The PDF of the emulated PPE member values within the observationally constrained range of $\Delta N_{d(NH-SH)}$ is shown in the top left for $\Delta N_{d(PD-PI)}$ (c) and top right for RF_{aci} (d).

As there are no observations of pre-industrial N_d, the accuracy of modeled PI N_d cannot be evaluated directly. However, we are able to draw three qualitative conclusions regarding the PI and PD N_d from the models. First, in the GCMs the majority of the PD-PI change is in the NH. This is consistent with the zones of maximum anthropogenic emissions and direct aerosol forcing [*Schulz et al.*, 2006; *Feng and Ramanathan*, 2010]. Second, sources of CCN over the SO are largely marine with very small contributions from continents, and levels that are mostly unchanged from the PI to the PD [*Hamilton et al.*, 2014]. Third, our analysis of the Aerocom phase II and HadGEM3-GA7.1 development simulations show the PI N_d is fairly similar in the NH and SH, with a difference in the 30°-60° latitude bands over oceans for these simulations of 16 ± 7 cm^{-3} at 95% confidence. In contrast, simulated PD N_d difference between these bands is 43 ± 8 cm^{-3} at 95% confidence. The larger PI N_d in the NH compared to the SH is primarily due to biomass burning emissions in the NH [*Hamilton et al.*, 2018]. However, the relative hemispheric symmetry in PI N_d is consistent with modelling studies of aerosol sources over oceans in the PI, where marine sources contribute a large fraction of marine CCN in both hemispheres [*Stier et al.*, 2006; *Carslaw et al.*, 2017].

Based on our ability to estimate N_d in the PD from remote sensing retrievals and the aforementioned inferences from GCMs, we can use the hemispheric PD N_d difference between the polluted NH and the pristine SH oceans to gain insight into the change in global-mean area-weighted N_d between PD and PI over land and ocean ($\Delta N_{d(PD-PI)}$). We find that there is a positive correlation between $\Delta N_{d(PD-PI)}$ and the differences in marine N_d between 30°-60°N and 30°-60°S ($\Delta N_{d(NH-SH)}$) within the various GCMs examined in this study and the members of the PPE (Figure 2-1c). Examination of the million member sample shows that $\Delta N_{d(NH-SH)}$ is approximately linearly correlated with $\Delta N_{d(PD-PI)}$ ($R^2 = 0.3$). The Aerocom phase II models fall within the 95% prediction interval of the best fit to the PPE sample members except for ECHAM6. This may be due to ECHAM6's imposed minimum N_d of 40 cm^{-3}, which is near the mean PI N_d in the GCMs surveyed here (Figure 2-1a, b). MODIS estimates $\Delta N_{d(NH-SH)}$ to be between 32 and 37 cm^{-3} with 95% confidence. To agree with the satellite estimated range and the linear fit to the PPE, $\Delta N_{d(PD-PI)}$ is predicted to be 8 to 24 cm^{-3} at 95% confidence (Figure 2-1c).

The $\Delta N_{d(PD-PI)}$ predicted by the HadGEM3-GA7.1 development models is on the upper end of what is predicted by the PPE. This is consistent with the stronger ERF_{aci} in GA7 model versions (-2.75 Wm^{-2} in GA7.0, -1.45 Wm^{-2} in GA7.1) compared to the weaker aerosol forcing in the GA4.0 model version used in the PPE (-1.51 Wm^{-2} on average with a 95% credible range of -2.04 to -0.96 Wm^{-2}) [*Regayre et al.*, 2018; *Yoshioka et al.*, 2019]. The spread of $\Delta N_{d(PD-PI)}$ between the PPE, Aerocom, and HadGEM3-GA7 models demonstrates the importance of examining multiple GCMs to consider structural differences. Because few of the GCMs (3 of the 8 Aerocom models and none of the HadGEM3-GA7 models) are consistent with MODIS N_d, we also demonstrate the usefulness of sampling uncertainty within a single model by using the PPE. Using the million member sample helps us to avoid the equifinality issues raised by examining a single model variant [*Lee et al.*,

2016; *Carslaw*, 2018] and produces a small subset of model variants within the observational range. Further investigation of the aerosol parameters important in this subset of member variants may help us to understand the processes that are key to producing values of N_d that are consistent with satellite data.

We have constrained changes in $\Delta N_{d(PD-PI)}$ using satellite estimated $\Delta N_{d(NH-SH)}$. A similar constraint can be applied to RF_{aci}. The Aerocom phase II and HadGEM3-GA7.1 development models include aerosol-cloud adjustments, so for this analysis we rely on our million member sample from the PPE which has no aerosol-cloud adjustments. We find that the RF_{aci} is negatively correlated with $\Delta N_{d(NH-SH)}$ (Figure 2-1d). We fit the relationship between RF_{aci} and $\Delta N_{d(NH-SH)}$ in the million member sample using a second order polynomial. For large values of $\Delta N_{d(NH-SH)}$, the spread in RF_{aci} from the PPE is very broad. However, when N_d is more symmetric between hemispheres, the range of RF_{aci} produced by different members of the PPE narrows. The prediction interval of the fit combined with the satellite estimated $\Delta N_{d(NH-SH)}$ constrains RF_{aci} to be between -1.2 and -0.6 Wm^{-2} at 95% confidence.

One caveat to our constraint on RF_{aci} and $\Delta N_{d(PD-PI)}$ is that our methodology may suffer from the same limitations that all single-observation constraints suffer from, which is producing an overly tight constraint on model behavior by not accounting for the structural uncertainty of the GCM [*Johnson et al.*, 2018]. This structural uncertainty is better constrained when more independent observations and their associated uncertainties are used simultaneously [*Johnson et al.*, 2018]. Thus, combining this methodology with other observational constraints may avoid these single observation issues (e.g. as in the multi observation constraint on ERF_{aci} in *Johnson et al.* [2018] and *Regayre et al.* [2019]) as well as help to constrain uncertainty associated with other processes in the models not captured by $\Delta N_{d(NH-SH)}$ (e.g. the aerosol optical depth constraint on

RF_{ari} presented in [*Watson-Parris et al.*, 2020]). We have chosen to only use satellite data over oceans in calculating $\Delta N_{d(NH-SH)}$ because it is more extensively evaluated against aircraft measurements [*Grosvenor et al.*, 2018b]. This broadens the constraint on global-mean PI to PD changes in cloud properties ($\Delta N_{d(PD-PI)}$ and RF_{aci} in the insets of Figure 2-1c, d) by ignoring information from satellite data over land. However, we choose to use more robust satellite data at the cost of a broader, but more reliable, constraint on global-mean changes.

2.3.2 *Evaluating Southern Ocean N_d*

The hemispheric constraint depends on the accuracy of the satellite-derived values of PD N_d. As noted in the introduction, MODIS N_d has been extensively validated against aircraft measurements in the NH and parts of the SH [*Ahn et al.*, 2018; *Grosvenor et al.*, 2018b; *McCoy et al.*, 2018]. Because aircraft observations of N_d are not as plentiful in the more remote regions of the SO, we use other datasets to provide additional assessment of the quality and the believability of the surprising SO MODIS N_d pattern (Figure 2-2).

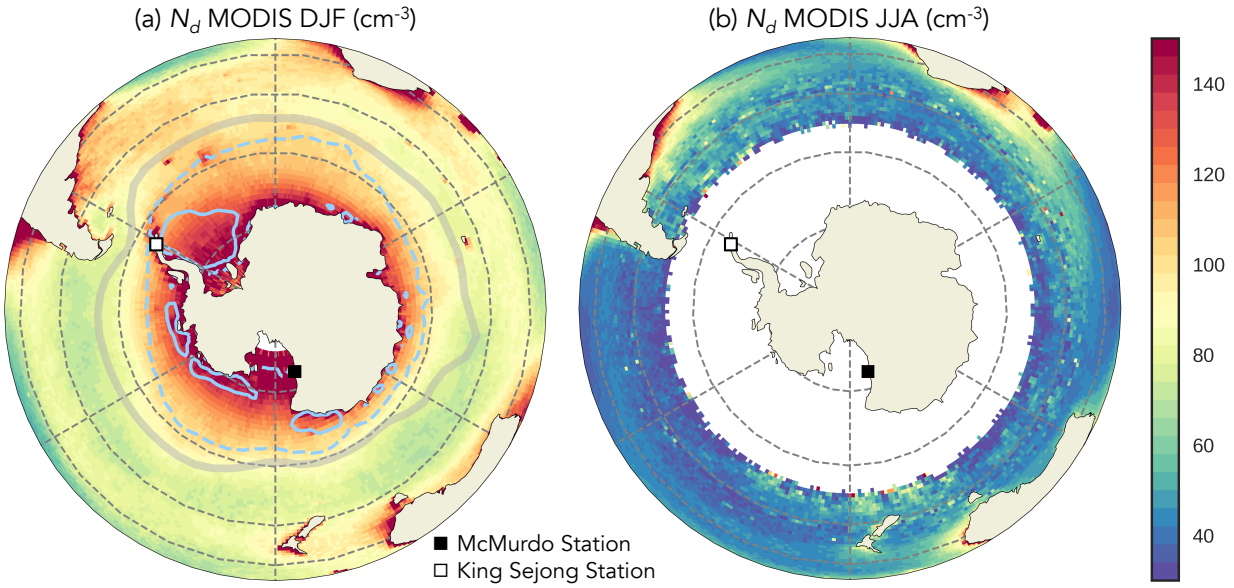

Figure 2-2 *Mean N_d calculated from MODIS data in summer (a, DJF) and winter (b, JJA). Seasonal-mean sea ice contours from OSTIA fractional sea ice are shown as dashed (1%) and solid blue lines (50%). Locations are shown for McMurdo Station [Liu et al., 2018] (solid square) and King Sejong Station [Kim et al., 2017] (empty square). The position of the DJF lower tropospheric storm track [Hoskins and Hodges, 2005] is shown with a gray line.*

The latitudinal and seasonal patterns of MODIS N_d are supported by the multi-year records of CCN from Antarctic ground sites at King Sejong Station (62°S) [*Kim et al.*, 2017] and McMurdo Station (77°S) [*Liu et al.*, 2018] (Figure 2-2, Figure SI 2- 6a). Comparison of MODIS N_d within 4° of each station to the CCN station data shows matching summertime peaks and an increase with poleward latitude between King Sejong and McMurdo (Figure SI 2- 6a). Summertime CCN measured at King Sejong was classified as largely biogenic [*Jang et al.*, 2019; *Kim et al.*, 2019]. This is consistent with measurements taken during cruises in the SO that observed increases in CCN, biogenic CCN-precursor gases (i.e. phytoplankton emissions of dimethyl sulfide or DMS which can be oxidized in the atmosphere to form either sulfate, an efficient CCN [*Ayers and Gras*, 1991; *Fitzgerald*, 1991; *Pandis et al.*, 1994; *Boucher and Lohmann*, 1995; *Ayers et al.*, 1997; *Ayers*

and Gillett, 2000], or precursors for particle nucleation) [*Schmale et al.*, 2019], and concentrations of small particles that grow into CCN (i.e. nucleation mode aerosols, often newly formed from biogenic precursor gases [*Katoshevski et al.*, 1999; *Kerminen et al.*, 2018]) [*Humphries et al.*, 2016] near Antarctica. The RITS (*Radiatively Important Trace Species*) campaign [*Covert et al.*, 1996; *Quinn et al.*, 1996] also observed a summertime increase in total aerosol concentration (including nucleation and CCN size aerosols) between its winter '93 and summer '94 cruises along the coast of Antarctica (Figure SI 2- 6 map, b).

We suspect that the summertime peak in N_d near Antarctica is linked to increases in biological activity as sea ice retreats in these regions. The seasonal sea ice zone's high productivity and frequent, large phytoplankton blooms [*Smith and Nelson*, 1986; *Sullivan et al.*, 1988; *Petrou et al.*, 2016] lead to enhanced emissions of biogenic CCN precursor gases. Recent observations found increased concentrations of trace gases associated with DMS oxidation in the seasonal sea ice zone [*Schmale et al.*, 2019], nucleation mode particles at ice-edge [*Lachlan-Cope et al.*, 2019], and nucleation mode particles in biologically active basins near Antarctica [*Jang et al.*, 2019; *Kim et al.*, 2019]. The 2016 ORCAS (*O_2/N_2 Ratio and CO_2 Airborne Southern Ocean*) flight campaign sampled N_d over both open water and broken ice in the seasonal sea ice zone in the Amundsen and Weddell seas. ORCAS observed higher N_d over marginal sea ice than over open water (based on estimates of sea ice fraction [*Donlon et al.*, 2012] interpolated to the flight track; Figure SI 2- 6c). The high N_d over marginal sea ice observed during ORCAS (median ~140 cm^{-3}) is consistent with the N_d observed during the OFCAP flights across the Antarctic peninsula [*Lachlan-Cope et al.*, 2016] (Figure SI 2- 6c) and with the MODIS N_d. The increase in N_d over regions with marginal sea ice is also supported by MODIS N_d over the period 2003-2015 sampled along the ORCAS flight track (Figure SI 2- 6d). Examination of the entire Southern Ocean region by MODIS shows

that as the sea ice begins to retreat (October-November), N_d increases sharply over recently opened water (Figure SI 2- 7) potentially linked to increases in phytoplankton productivity. Open water produces more sea spray emissions than ice-covered regions. This may also contribute to increased N_d, but with limited seasonality. In summary, in-situ measurements of aerosol concentrations and aircraft measurements of N_d quantitatively support the seasonal and spatial patterns of satellite-derived N_d in the SO.

2.3.3 *What does pristine PD N_d tell us about GCM discrepancies in aerosol-cloud interactions?*

We have demonstrated that the PD N_d hemispheric contrast is a useful framework for interpreting GCM behavior. We have also motivated that MODIS N_d is a reliable estimate of SH N_d as well as NH N_d. We further showed that summertime high latitude N_d can be a factor of three smaller in GCMs than in satellite estimates (Figure 2-1a, b). This leaves us with an important question: how can we use the information contained in estimates of PD N_d in pristine regions to understand what processes are currently missing or poorly captured in GCMs? Resolving these discrepancies is important to accurately represent aerosol-cloud interactions occurring in the PD and PI.

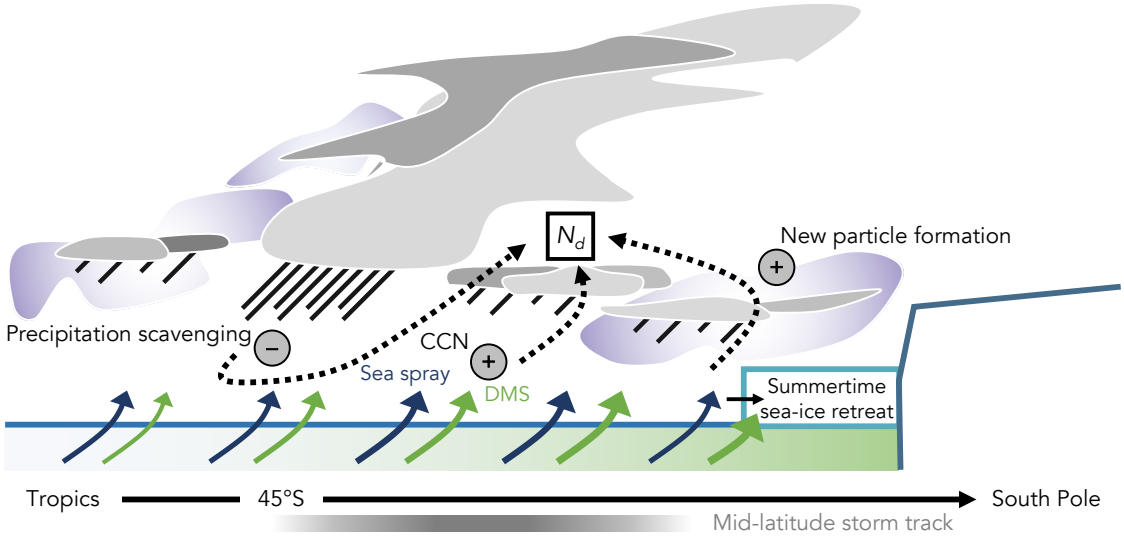

Figure 2-3 *Schematic depicting main sources (+) and sinks (-) of aerosol affecting the cloud droplet number concentration (N_d) in the Southern Ocean. Approximate location of the climatological mid-latitude storm track is shown for reference.*

In answering this question, it is important to remember that the amount of aerosol available to be activated into cloud droplets is a function of both aerosol sources and sinks. The amount of cloud droplets, N_d, will also be a function of these sources and sinks. The SO is a pristine environment where aerosol sources are analogous to the PI. However, both aerosol sources and sinks vary across the SO (see diagram in Figure 2-3). Sources of SO CCN are a combination of sea spray and biogenic sources and depend upon surface and free-tropospheric physical and chemical processes [*Korhonen et al.*, 2008]. Emissions from ocean biology also influence NH maritime N_d and are known to control NH marine CCN and nucleation mode seasonality [*O'Dowd et al.*, 2004; *Sanchez et al.*, 2018; *Zheng et al.*, 2018]. Sea-spray emissions in the SH vary a small amount during the year [*Korhonen et al.*, 2008; *McCoy et al.*, 2015] and are unlikely to be contributing to the seasonal cycle of N_d [*McCoy et al.*, 2015]. The dominant contributor to biogenic

CCN is thought to be DMS emissions from phytoplankton with regional contributions from primary emissions of organically-enriched sea-spray [*Burrows et al.*, 2014; *McCoy et al.*, 2015].

It is thought that nucleation and growth of new particles results in between 40-70% of global CCN [*Dunne et al.*, 2016]. DMS-oxidation products along with other stabilizing compounds can act as precursors for gas to particle conversion and form new, nucleation mode aerosols [*Katoshevski et al.*, 1999; *Kerminen et al.*, 2018]. New particle formation has been documented in the free troposphere, coastal regions, at ice edges, near clouds, and in the boundary layer if conditions are favorable [*Kerminen et al.*, 2018]. Biogenic free tropospheric new particles are known to influence boundary layer CCN in both the NH [*Sanchez et al.*, 2018] and across the SH [*Covert et al.*, 1996; *Humphries et al.*, 2016]. SO air masses observed at the edge of Antarctica have signatures of sulfate-based new particle formation, contributing to high summertime and strongly seasonal nucleation and CCN concentrations [*Humphries et al.*, 2016; *Kim et al.*, 2017; *Herenz et al.*, 2019; *Lachlan-Cope et al.*, 2019]. In the Antarctic and Arctic, particle formation events are typically connected to emissions from biological activity or iodine emitted from melting ice [*Kerminen et al.*, 2018; *Lachlan-Cope et al.*, 2019]. In the Arctic, where seasonal ice melt increases biological activity initiating bursts of new particle formation, a ~20% summertime increase in CCN concentration can occur [*Dall Osto et al.*, 2017]. In the Antarctic, a similar summertime increase in new particle formation over the seasonal ice zone occurs [*Lachlan-Cope et al.*, 2019]. Increasing concentrations of new particles during sea ice melt may be contributing to increases in N_d over retreating sea ice (Figure SI 2- 6d, Figure SI 2- 7).

The primary sink of CCN is coalescence scavenging associated with the formation of precipitation [*Wood et al.*, 2012]. The rapid decrease in N_d off the coast of Antarctica may be related to enhanced precipitation scavenging associated with mid-latitude storms (Figure 2-3). This

idea is supported by the location of the minima in MODIS N_d coinciding with the climatological position of the SH storm track in austral summer (Figure 2-2a) [*Hoskins and Hodges*, 2005]. *In situ* measurements of trace gases and aerosol number concentration indicate that the biogenic CCN may be enhanced near Antarctica [*Humphries et al.*, 2016; *Schmale et al.*, 2019] possibly resulting from a weakening in precipitation scavenging, an increase in biological activity near ice edge, or a combination of both effects.

To assess the role of precipitation sinks in the Southern Ocean, we apply a simple source and sink budget model for CCN and equivalently N_d [*Wood et al.*, 2012]. The ratio between N_d and N_d computed with no precipitation loss is inversely proportional to the precipitation rate and is insensitive to the aerosol source term (see Methods). Unsurprisingly, the strongest precipitation sink is in the heavily precipitating SH storm track (~50°S, see N_d decrease in Figure 2-1a), and the budget model shows that coalescence scavenging drives down N_d to ~30% of the values that would occur without a precipitation sink (exact values shown in Figure SI 2- 8k-o). Poleward of the storm track, at 65°S, N_d is only reduced to ~70% of the value without a precipitation sink (Figure SI 2-8k). This may be a reflection of MBL depth being shallower over the cold waters near Antarctica and decreasing the clouds capacity to support significant boundary layer cloud precipitation [*Chan and Wood*, 2013]. The budget model also shows us that the fractional reduction of N_d by precipitation has only a weak seasonal cycle and is therefore not a major determinant of the seasonal N_d cycle over the SO region. This is consistent with the conclusion from previous studies that seasonal variability in N_d over the SO is driven primarily by biogenic aerosol sources [*Ayers and Gras*, 1991; *Ayers et al.*, 1997; *Meskhidze and Nenes*, 2006; *McCoy et al.*, 2015].

Based on our budget model assessment, we conclude that precipitation (i.e. coalescence scavenging) acts as a strong sink of CCN in the midlatitude storm track and drives the decrease in

N_d equatorward of Antarctica. There is evidence that models precipitate too much in this region, possibly creating too strong a sink of N_d in the storm track in GCMs [*Stephens et al.*, 2010]. Discrepancies between satellite estimates and modeled N_d near Antarctica, where precipitation sinks of aerosol are weak, indicate that aerosol production processes are not well represented in GCMs either. It is likely that the same aerosol processes that are important near Antarctica (i.e. those linked to ocean biology) influence midlatitude regions that have stronger precipitation sinks. Missing or incomplete mechanisms for producing CCN in the biologically active region near Antarctica have implications for CCN across the SH. Disagreement between modeled and satellite estimates in summertime midlatitude N_d in the NH, which has similar marine biogenic aerosol sources, suggests that these model discrepancies are not relegated to the SH alone. GCMs may be additionally suffering from equifinality issues [*Lee et al.*, 2016; *Carslaw*, 2018]. Thus, representation of the mechanisms leading to high near-Antarctic and summertime SO N_d as well as more accurate representations of precipitation sinks are important for advancing estimations of N_d in the PI and N_d in PD pristine regions.

What factors could be leading to the GCM underestimations of SO N_d? One possibility is that GCMs do not emit enough DMS into the SO, stalling particle formation and growth processes. The amount of DMS in SO seawater and the exchange of DMS between water and air are uncertain [*Lana et al.*, 2011]. Enhancement of global DMS concentrations by 70% in HadGEM3-GA7.0 did not substantially alter SO N_d or the hemispheric contrast, $\Delta N_{d(NH-SH)}$ (Figure 2-1, Figure SI 2- 3). Uncertainty in air-sea exchange processes complicates this evaluation [*Bodas-Salcedo et al.*, 2019]. However, sensitivity tests in HadGEM3-GA7.1 demonstrate that inclusion of more complete sulfate chemistry processes (relevant for summer CCN) and improved parametrizations of sea salt production (relevant for winter CCN) brings modeled N_d into closer agreement with

MODIS N_d in the SO [*Revell et al.*, 2019]. Another possibility is that nucleation of new particles, particularly from DMS-oxidation products, is less efficient in GCMs. If natural new particle formation mechanisms are not included in GCMs then it is likely that models systematically overestimate the strength of aerosol-cloud radiative forcing [*Gordon et al.*, 2016]. This would result in an RF_{aci} that is too strong in models, consistent with our constraint of the PPE members by $\Delta N_{d(NH-SH)}$.

2.4 Conclusions and Discussion

The hemispheric contrast in oceanic N_d ($\Delta N_{d(NH-SH)}$) offers a constraint on changes in global-mean N_d between the preindustrial (PI) and present day (PD) ($\Delta N_{d(PD-PI)}$) and, by extension, on radiative forcing due to aerosol cloud interactions (RF_{aci}) (Figure 2-1c, d). Based on the satellite derived $\Delta N_{d(NH-SH)}$ and output from GCMs, $\Delta N_{d(PD-PI)}$ is constrained to be between 8 and 24 cm^{-3}. RF_{aci} is constrained to be between -1.2 and -0.6 Wm^{-2}. This constraint on RF_{aci} agrees with the most probable range of -1.2 to -0.3 Wm^{-2} developed in *Bellouin* [2019]. The range developed in *Bellouin* [2019] utilized observational studies relating aerosol variance to N_d variance. Our analysis is insensitive to aerosol observations and provides an important confirmation of this range using a different approach. Our analysis also suggests that the weaker RF_{aci} in the *Bellouin* [2019] range is not consistent with the N_d calculated from satellite data. However, an important caveat to this study and other studies seeking to offer an observational constraint on GCM behavior using a single criterion is that it may result in an overly tight constraint on model behavior due to structural uncertainties in the GCM [*Johnson et al.*, 2018; *Regayre et al.*, 2018]. Future analysis will combine the hemispheric contrast in N_d with other constraints on model behavior to reinforce its robustness.

A key finding of this study is that models generally simulate larger hemispheric N_d differences than are calculated from satellite retrievals (Figure 2-1c). Satellite derived $\Delta N_{d(NH-SH)}$ is relatively low partly due to high local summertime N_d over the SH midlatitudes (Figure 2-1a). MODIS N_d near Antarctica was found to be even higher, reaching values close to those in outflows from North America and East Asia. Evaluation of in-situ data from cruises, flight campaigns, and stations on the Antarctic continent confirms the accuracy of satellite-derived SO N_d (Figure 2-2). Evaluation of SH CCN precipitation sinks suggests that high summertime N_d near Antarctica is in part due to low removal rates by precipitation scavenging on the poleward flank of the storm track (Figure 2-3). None of the GCMs surveyed here or the 235 original PPE ensemble members come near to reproducing the high near-Antarctic values in summertime (Figure 2-1, individual models and PPE members shown in Figure SI 2- 3, Figure SI 2- 4 respectively), suggesting models are missing key processes and/or emission sources important for CCN near Antarctica and potentially across the SH.

Ultimately, N_d is the variable that controls aerosol-cloud interactions (aci) in liquid clouds. This quantity is the product of aerosol emissions, removal, transport, processing, and nucleation, and it serves as a key assessment of GCM skill in portraying aci. This reinforces the need to continue to create N_d datasets from new satellites and in new ways. We propose that future evaluations of GCM aerosol-cloud interactions use the information contained within the contrast between pristine and polluted regions as an important test of realism in addition to evaluation of predicted N_d within anthropogenically-perturbed regions.

Chapter 3. RECENT PARTICLE FORMATION AND AEROSOL VARIABILITY NEAR SOUTHERN OCEAN LOW CLOUDS

3.1 INTRODUCTION

The Southern Ocean Clouds, Radiation, Aerosol Transport Experimental study (SOCRATES) was designed to expand our knowledge of the aerosol sources and sinks in cyclone cold sectors and help us better understand the complexities of SO aci. I pose three questions in my analysis: what is the mechanism for producing the copious quantities of Aitken mode sized particles over the SO? How do these small aerosols influence the clouds in this pristine environment? How do these aci mechanisms inform state of the art climate models? Before addressing these, however, let us look at the sources of pristine aerosols in the SO in more detail.

Aitken mode particles form through homogeneous nucleation of precursor gases [*Seinfeld and Pandis*, 2006]. Two major precursor gases in the marine environment are sulfuric acid (H_2SO_4) and methane sulfonic acid (MSA), both oxidation products of DMS [*Fitzgerald*, 1991; *Ayers et al.*, 1997]. For gas to particle conversion to occur, precursor gases must be present and the total aerosol surface area (primarily from coarse and accumulation mode sized aerosols) must be low enough to discourage vapor deposition on preexisting particles (<10-20 $\mu g\ cm^{-3}$) [*Covert et al.*, 1996]. The latter is more likely in the free troposphere (FT) [*Clarke*, 1993]. SO observations indicate particles with diameters $\leq 0.5\ \mu m$ are primarily non-sea-salt sulfate, indicating formation was assisted by DMS oxidation products [*Fitzgerald*, 1991]. Along with sulfuric acid, ions, organics, and other compounds can also play a role in particle formation [*Gordon et al.*, 2017].

Sea spray aerosol production mechanisms contribute to the upper end of the accumulation mode size range and the coarse mode [*Grythe et al.*, 2014]. In the wintertime, sea spray dominates the boundary layer aerosol signature as biogenic sources are inactive. However, most of the aerosol particles with diameters ≤ 0.2 μm are not composed of sea spray or organics in the summertime but are dominated by non-sea-salt sulfate [*Bigg*, 2007; *Bigg and Leck*, 2008; *Fossum et al.*, 2018]. From a synthesis of observations and modeling studies, entrainment of new particles from the FT is thought to be the main source of aerosol number in marine regions at low and middle latitudes [*Kerminen et al.*, 2018].

Taken together, these studies broadly suggest that the majority of Aitken mode particles in marine regions are produced through gas to particle conversion of DMS oxidation products, that these particles may be forming in the FT, and that they are likely important in controlling the summertime Southern Ocean CCN number concentrations. These three ideas are the fundamental basis for our analysis and have been the subject of many other papers.

There is evidence for new particle formation occurring aloft in the SH during austral summer associated with DMS-oxidation products. Aitken and even smaller ultra-fine mode particles originating in the FT were observed repeatedly in the marine boundary layer during two ship cruises [*Covert et al.*, 1996]. SH (20-70°S) sampling showed that the aerosol size distributions were dominated by the Aitken and ultra-fine mode aerosol, with variability in the SO aerosol concentrations associated with the passage of frontal systems (40-70°S). Aitken and ultra-fine mode particles rapidly subsided from the FT after the passage of a front in these cases and had not grown to larger sizes as they had spent little time in the marine boundary layer (MBL). Because there was no positive correlation between aerosol surface area and the concentrations of ultra-fine particles, it is likely that these particles were formed elsewhere before they were carried into the

boundary layer [*Covert et al.*, 1996]. More recent ship observations showed similar behavior: high concentrations of aerosols associated with air descending from the free troposphere over Antarctica [*Humphries et al.*, 2016]. Two SO aircraft transects (August 2016 and February 2017) also found high concentrations of new particles (diameters between 3-7 nm) occurring between altitudes of ~ 3 and 9 km but few new particles in the MBL [*Williamson et al.*, 2019].

How are these new particles produced aloft? One possibility is the occurrence of cloud outflow particle production. These mechanisms have been observed in many regions of the world and across a variety of cloud types (as reviewed in *Kerminen et al.* [2018]). Particle generation results when air masses rich in precursor gases are cleansed of their accumulation and coarse mode aerosol by cloud droplet scavenging and precipitation processes, reducing aerosol surface area enough to enable new particle formation once the air mass exits the cloud. Only the less water-soluble gases (e.g. DMS [*Seinfeld and Pandis*, 2006]) will survive cloud processing, so it is likely that oxidation of gases to particle precursors happens upon exiting the cloud. Large eddy scale (LES) simulations of new particle formation in cumulus cloud outflow in the South East Pacific demonstrate how gases are processed in these events before gas to particle conversion takes place [*Kazil et al.*, 2011]. Based on this study, in marine environments it is likely that DMS fluxed from the surface is lifted through clouds before oxidizing into precursor gases (e.g. SO_2 and then H_2SO_4 and MSA) upon exiting the cloud and being exposed to oxidizing compounds such as OH. Gas to particle conversion will happen shortly thereafter, assisted by the exposure to increased actinic flux, colder temperatures, and high relative humidity [*Seinfeld and Pandis*, 2006] in cloud outflow regions.

Ultra-fine and Aitken mode aerosols formed in cloud outflows can subsequently descend, grow, and be incorporated into the MBL to contribute to the CCN budget. *Clarke et al.* [1998]

made an important comparison between particle generation in outflows from SO shallow cumulus and from deeper convective clouds in the tropics, arguing that in the tropics, particles descend from higher and more slowly, allowing time for coagulation and growth. This factor, along with residence time in the MBL [*Covert et al.*, 1996], affects how many aerosols grow to CCN sizes.

Deep convective clouds have been found to be an important source of new particles in numerous locations across the world [*Kerminen et al.*, 2018]. An examination of deep convective clouds associated with a mesoscale convective system spanning the United States estimated that new particles formed subsequent to cloud uplift in such systems contribute substantially to upper tropospheric aerosol concentrations in the mid-latitudes [*Twohy et al.*, 2002]. In the SO, particle formation, likely from nucleation of co-occurring sulfuric acid, has been observed at the edges of frontal cloud systems [*Weber et al.*, 2001]. We posit that deep stratiform cloud types in the Southern Ocean might also be producing new particles, which suggests that deeper clouds may be contributing significantly to the persistently high concentrations of small particles observed throughout the depth of the SO free troposphere.

3.2 Materials and Methods

3.2.1 *Aircraft Sampling*

In the SOCRATES campaign [*McFarquhar et al.*, 2020 submitted], the National Science Foundation Gulfstream-V (GV) aircraft flew out of Hobart, Tasmania, over the SO. Fifteen flights (Figure 3-1a) were designed to sample low clouds in the cold sectors of cyclones. Each research flight (RF) had a similar sampling strategy (Figure 3-1b). Initially, the GV flew a high (~6 km altitude) survey leg into a region forecast to be dominated by low clouds until a southernmost latitude was reached, typically 60-62°S. The cloud radar, lidar, and dropsondes were used to probe the underlying cloudy boundary layer. After descending to an altitude above cloud (typically ~3

km), the GV returned to Hobart while sampling the boundary layer through repetitions of a flight module. Each module consisted of 10-minute level legs above cloud, in cloud, and below cloud at 150 m above the sea surface, followed by sawtooth profiling through the boundary layer. Module sampling was continued as long as operational constraints allowed, after which the plane climbed back above the boundary layer to return to Hobart. There were two exceptions to this method during the campaign: RF11 and 15 had flight paths customized for targeting cumulus cloud tops to sample mixed-phase microphysics. The limited observations obtained north of 45° S are affected by proximity to Tasmania. Thus, our analysis focuses on the SO sampled between 45 and 62°S.

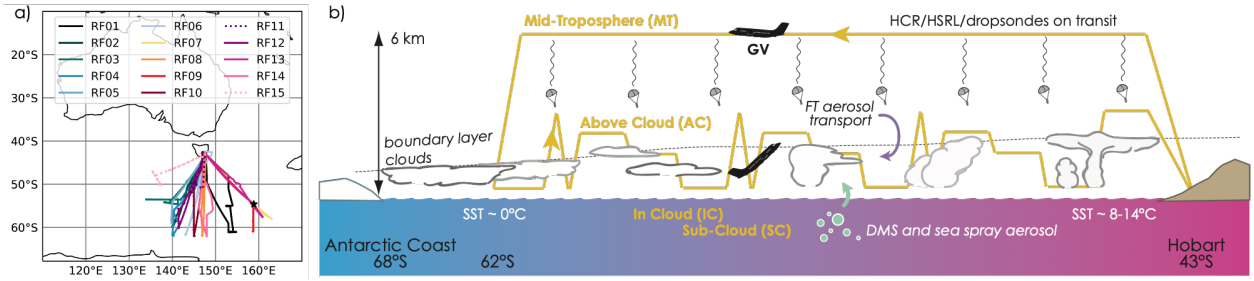

Figure 3-1 *a) Flight locations from SOCRATES (dashed lines for cumulus targeting flights, solid for standard modules) and b) standard flight module plan with identified leg components. Macquarie Island ,a coordinated site for ground observations as detailed in McFarquhar et al. [2020 submitted] is marked with a star in (a).*

The GV was equipped with a wide array of instrumentation [*McFarquhar et al.*, 2020 submitted]. The low-rate, 1 Hz flight, state, and microphysical data from the GV was used in this analysis [*Laboratory*, 2019]. The cloud droplet number concentration (N_d) is from the cloud droplet probe (CDP). Aerosol number concentrations are taken from two instruments for our analysis, a condensation nuclei counter (CN, all aerosols with diameters larger than ~0.011 μm) and a ultra-high sensitivity aerosol spectrometer (UHSAS or UHSAS100 when adjusted to the accumulation size range of 0.1 – 10 μm from the nominal size range of 0.085 – 1 μm). The models

used were a TSI-3760A condensation nucleus counter on a HIAPER modular inlet and DMT UHSAS-A, S/N 001. The UHSAS provides both size-resolved and integrated concentrations within this range. Size resolved number concentrations for coarse mode aerosol are from the CDP (2 – 50 μm). The surface area reported in this paper is computed from the coarse and accumulation mode size distributions, accounting for particles with diameters between 0.085 and 50 μm. Because UHSAS reports a dried aerosol diameter, surface area is adjusted for swelling associated with the environmental relative humidity. We use the growth factor reported for extinction coefficients, f_{grow}, in eq. 3 of *Chand et al.* [2012]. We then scale this factor by 2/3 to account for surface area growth instead (*personal communication Mike Reeves, NCAR*):

$$SA_{UHSAS} = (\pi D_{UHSAS}^2)\left(1 + f_{grow}^{2/3}\right) \qquad \textit{eq. 3-1}$$

As in *Chand et al.* [2012], the values assumed in calculating f_{grow} are for sulfate aerosols which have a growth factor between sea salt and pollution aerosols. This is not an unreasonable assumption as sulfate or sulfur-based aerosols were the most frequently occurring throughout the campaign (3.3.1.3).

All aerosol measurements are subject to screening by a cloud and rain mask based on the CDP and the two-dimensional optical array probe (2D-C). Aerosol observations were discarded when our empirically chosen thresholds were exceeded: liquid water content from the CDP ≥ 0.01 g m^{-3} or precipitation droplets from the 2DC ≥ 1 L^{-1} [*Bretherton et al.*, 2019]. Samples were removed for 10 seconds following detection of cloud or drizzle to avoid measurement contamination. Measured temperature and pressure are used to adjust aerosol concentrations to mg^{-1} from cm^{-3} to account for volume changes at different levels in the atmosphere. Cumulative size distributions are calculated from the drizzle and cloud screened aerosol number concentration for CN, size resolved UHSAS, and size resolved CDP.

We use aerosol measurements behind a counterflow virtual impactor (CVI) [*Noone et al.*, 1988; *Twohy et al.*, 1997] to understand aerosol composition using two approaches: i) scanning transmission electron microscopy (STEM) and X-ray analysis of particles impacted on formvar carbon grids for particles above, in, and below cloud as in *Twohy et al.* [2013], and ii) reconstructed particle volatility estimates from comparing CVI heated CN (using a TSI-3010 condensation nucleus counter, CN_{CVI}) and UHSAS100 (using a UHSAS-G, S/N 15 as in *Kupc et al.* [2018], $UHSAS100_{CVI}$) measurements to un-heated CN, UHSAS100 measurements for free tropospheric particles. Specific examples from the SOCRATES STEM analysis will be highlighted here; for complete details see *Twohy et al.* [2020 submitted]. Normally, the CVI preferentially separates cloud droplets using a counterflow out the tip. For out of cloud, ambient aerosol measurements the counterflow is turned off. The CVI has two primary heaters that can affect particle volatility, one on the probe and one on the long sample line. The CVI probe was heated to ~50-60°C for the majority of the flights to evaporate water and prevent icing when sampling inside supercooled clouds. Because of the instrument and inlet configuration required on the GV, a 4.5m line heated to ~40°C was run between the inlet of the CVI and the instrument rack. The total residence time in the CVI probe and sample line is 2.3 seconds. During their passage through the heated probe and sample line, smaller, more volatile ambient aerosol particles are evaporated. The result of this setup is that for the majority of flights during the campaign the instruments behind the CVI sampled only particles not volatile at ~50°C. During the second half of the campaign, the temperature of the CVI instrument was varied between ~25-60°C to allow for a more detailed investigation of the particle volatility observed. Particles have volatilized in this arrangement when their diameter is reduced to below the CN_{CVI} detection limit (11 nm). Since the CVI has two primary heated regions, the instrument (probe and tip) and sample line, and they behave differently

when the heaters are turned off, the maximum of these three temperatures is used for estimating the volatility temperature (i.e. CVI tip, probe, and sample line). Because this analysis approach was not foreseen, the volatilization estimates produced are inexact but still useful.

We use observations from the 2015 Cloud System Evolution in the Trades (CSET) campaign [*Albrecht et al.*, 2019] in the North East Pacific (NEP) to provide a sub-tropical comparison for SOCRATES. This comparison follows in the footsteps of *Clarke et al.* [1998] in establishing the uniqueness of Southern Ocean observations. CSET sampled the stratocumulus to trade cumulus transition between California and Hawaii using a similar modular strategy as in SOCRATES for sampling the cloudy boundary layer. In CSET, the GV used similar wing-mounted instrumentation to SOCRATES, including the CN, UHSAS, CDP, and 2DC [*Laboratory*, 2017]. This allows a parallel data screening and analysis methodology to be applied to both campaigns.

The CSET and SOCRATES flight paths approximately fall along common distance axes. During CSET, this axis was a diagonal line between the coast of California and Hawaii [*Bretherton et al.*, 2019]. During SOCRATES, the axis was roughly a north-south line between Hobart, Tasmania and the coast of Antarctica (Figure 3-1a). Average structures describing the mean profiles along these axes are developed for analysis. Observations for each flight are sorted into 500 m altitude layers, projected along the appropriate axis, and the median value for the variable in question is computed for each 2.5° bin. Only bins with at least ten 1 Hz flight observations are considered and aerosol samples are subject to the same precipitation and cloud screening as described above. Along with deriving individual flight composites, these individual composites are averaged together to develop a mean campaign composite as in *Bretherton et al.* [2019]. These

gridded structures are particularly useful in comparing variables not sampled simultaneously, such as cloud droplet number and aerosol concentrations.

3.2.2 *Air-mass Back Trajectories*

Interpreting SOCRATES aerosol observations requires knowledge of their air mass histories. We used the Hybrid Single Particle Lagrangian Integrated Trajectory (HYSPLIT) model [*Stein et al.*, 2015] to provide this context. HYSPLIT back trajectories were based on Global Data Assimilation System (GDAS) meteorology on a 0.5° by 0.5° grid. Seventy-two hour back-trajectories were calculated for each 10-minute flight segment, based on the aircraft altitude, latitude, and longitude at the mean segment time. The maximum CN concentration for the flight segment (CN_{Max10}) was used to identify likely instances of recent particle formation (RPF) since very high CN is indicative of RPF events in this pristine environment. We split the campaign trajectories by CN_{Max10} quartiles: the upper quartile ($CN_{Max10} \geq 2500$ mg^{-1}) is considered to be comprised of RPF cases and the lower three quartiles ($CN_{Max10} < 2500$ mg^{-1}) are considered unclear or non-RPF cases. This RPF identification method allows us to statistically analyze air mass histories. *Clement et al.* [2002] assessed timescales for sulfuric acid particle formation and growth to observable sizes (> 11 nm) and found that recently formed particles in the upper troposphere will be observable (~12.5-30 nm) within ~5-10 hours. This study was conducted using different instrumentation and occurred in the outflow of a mid-latitude storm system so there are likely differences with the FT events observed during SOCRATES. However, this estimate is useful in interpreting time-scales of particle growth during SOCRATES.

3.2.3 *Nudged Global Climate Model Simulations*

A goal of both the SOCRATES and CSET campaigns was to evaluate the fidelity of current global climate models (GCMs). One central strategy was to compare campaign observations with reanalysis-nudged hindcasts from GCMs, as applied by *Bretherton et al.* [2019] for CSET. This approach is applied for SOCRATES to evaluate version 6 of the Community Atmosphere Model (CAM6), which uses the MAM4 aerosol scheme detailed in *Liu et al.* [2016]. CAM6 SOCRATES simulations and microphysics are described in detail by [*Gettelman et al.*, 2020 submitted]. CAM6 is nudged by wind, temperature, and surface pressure fields from MERRA2 reanalysis [*Gelaro et al.*, 2017] with a 1-day relaxation timescale. This ensures the large-scale structure of simulated storms are close to the reanalysis, enabling simulation of similar profiles of clouds, humidity, and aerosols in the model when compared to aircraft observations at a given location and time. Clouds, humidity, and aerosols are not nudged in CAM6, allowing a critical appraisal of their accuracy using the GV measurements. CCN at ~0.6% super-saturation is determined to be the nearest analog to UHSAS100 (which was measured at a fixed super saturation close to ~0.6% during SOCRATES) for these simulations. CN is the sum of aerosol number concentration for coarse, accumulation, and Aitken mode. Both aerosol variables include in and out of cloud values from the model. Cloud droplet number concentration is reported as in cloud. Here we focus on comparing the measured aerosols and cloud droplet number concentrations with CAM6.

3.3 RESULTS

3.3.1 *Synoptically Generated Recent Particle Formation*

3.3.1.1 Observations of Recent Particle Formation in the Southern Ocean and Sub-Tropics

Frequent high concentrations of small aerosol particles were observed in SOCRATES throughout the depth of the SO free troposphere. Bursts of high CN concentrations with simultaneously low UHSAS100 concentrations were observed in the mid troposphere (~6 km) and above cloud (~3 km) on many of the flights. The high total aerosol concentrations are dominated by predominantly small particles with diameters of 0.01 to 0.1 μm, observed as the difference between CN and UHSAS100, which provides evidence for relatively recent particle formation.

Two example flight segments have been selected to highlight typical signatures that we interpret as evidence for RPF: one segment from a mid-tropospheric survey leg (Figure 3-2b, 6 km altitude, 1200 km long) and the other from an above cloud leg (Figure 3-2a, 3 km altitude, 300 km long). The first signature of RPF events is high CN (often exceeding 2500 mg^{-1}) that is rapidly varying, often with up to tenfold changes in concentration over a few km. The CN variability may be a marker of bursts of particle formation or boundaries between different air masses at different stages of nucleation [*Clement et al.*, 2002]. This is often accompanied by an anticorrelation between UHSAS100 accumulation mode and CN concentrations, a sign of particle formation events [*Covert et al.*, 1996]. Finally, particle surface area estimated from the coarse and accumulation mode is below 10 μm^2 mg^{-1} in these segments, a threshold associated with new particle formation [*Covert et al.*, 1996]. This low surface area is common in the SO free troposphere but very uncommon in the underlying boundary layer. Note that RPF events identified by the CN_{Max10} criteria (3.2.2) are marked for reference.

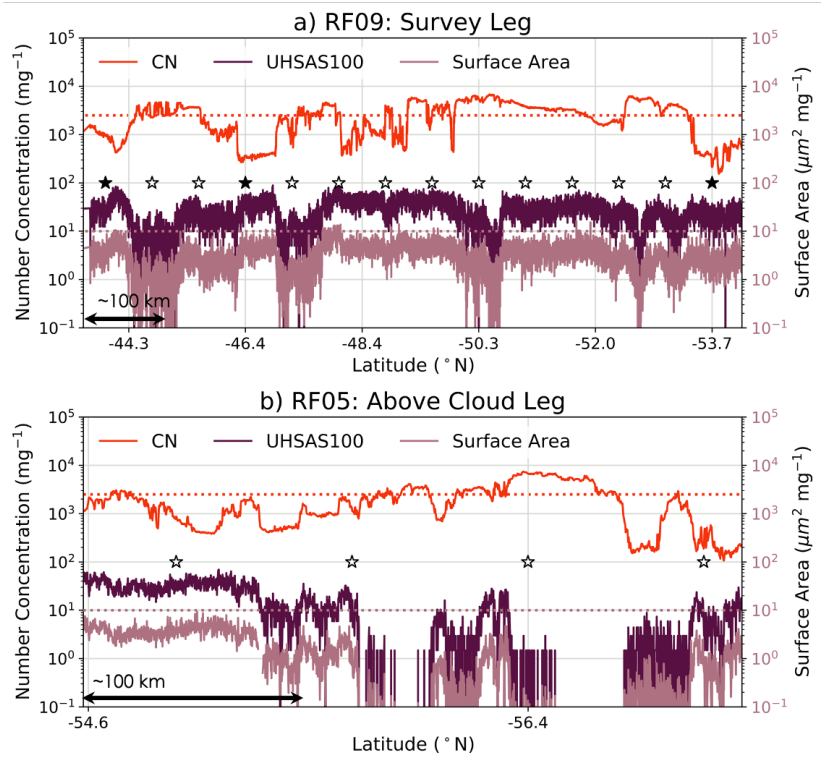

Figure 3-2 *Example cases for suspected RPF events observed in (a) survey-leg sampling in the mid-troposphere during RF09, and (b) above cloud leg sampling during RF05. Observations are shown against time as flight proceeded south (note difference in length scale between a and b). Number concentrations (left) for total (CN, orange) and accumulation mode (UHSAS100, purple) particles. Surface area for coarse and accumulation mode aerosol (right, pink). Dotted lines for 2500 mg^{-1} (orange) and 10 μm^2 mg^{-1} (pink) are included for reference. HYSPLIT trajectory initial locations are marked, solid stars for likely non-RPF events (CN_{Max10}>2500 mg^{-1}) and open stars for regions of suspected RPF events (CN_{Max10}>2500 mg^{-1}). Trajectory altitude profiles are shown for the segment of RF09 in (a) in McFarquhar et al. [2020 submitted].*

Outflow from cumulus congestus rising above the mean boundary layer is known to be a region of new particle formation in the SO [*Clarke et al.*, 1998]. SOCRATES sampled in or downwind of such regimes only infrequently. However, high particle concentrations, suggesting recent RPF events, were observed at all elevations of the free troposphere, as is shown in the following height-based separation analysis. SOCRATES data is split into sampling from the mid-

troposphere (MT: $Z \geq 4.5$ km, a and b), above-cloud (AC: $1.5 \leq Z \leq 4.5$ km, c and d), and sub-cloud (SC: $Z \leq 1.5$ km, e and f) regions (as in Figure 3-1b). At each level, normalized pdfs of cloud and drizzle screened CN and UHSAS100 are computed. Results are shown in Figure 3-3 along with CSET observations that will be discussed subsequently. In both the MT and AC sampling, a significant percentage of SOCRATES samples have CN well above 1000 mg^{-1} (Figure 3-3b, d). The UHSAS100 PDF at these levels shows infrequent concentrations in excess of 100 mg^{-1}, indicating these high CN concentrations are mainly Aitken mode particles (Figure 3-3a, c). Quantifying the 1000 mg^{-1} and above range gives us information about both the recently formed particles (bursts of which are captured by our stricter RPF event definition for statistical analysis, 2500 mg^{-1}) and the slightly lower concentrations of older, coagulated Aitken particles which still significantly contribute to the total aerosol amount. SC concentrations of CN in excess of 1000 mg^{-1} are less frequent but the PDF still retains significant probability near 1000 mg^{-1} (Figure 3-3f). As in the MT and AC sampling, the majority of particles SC are smaller than the accumulation mode size range (Figure 3-3e, f). However, we see a consistent shift with height in the UHSAS100 pdfs: at lower altitudes, the higher UHSAS100 concentrations become more common. The high CN concentrations become less common in the SC. This suggests that there is some coagulation and growth occurring as the aerosols descend into the boundary layer (subtly shifting UHSAS100 distributions to higher concentrations). However, CN is not significantly depleted until the SC which indicates cloud processing is key.

How different is the SO aerosol structure from the structure in subtropical marine regions and what does that information tell us about new particle production in the SO? We compare height-matched number concentration pdfs for UHSAS100 and CN from CSET at the same levels as in SOCRATES (Figure 3-3). At all altitude levels there is more accumulation mode aerosol and,

because total aerosol concentrations are lower, less Aitken mode aerosol in CSET than in SOCRATES. Accumulation mode aerosols have a wider range of high concentrations that can occur in the subtropics compared to the SO (Figure 3-3a, c, e), potentially affecting the variability in N_d and cloud albedo in these regions. Lower and less variable CN concentrations typify CSET compared to SOCRATES. SC CN campaign pdfs are the most separated (Figure 3-3f) while MT CN pdfs are the most similar (Figure 3-3b).

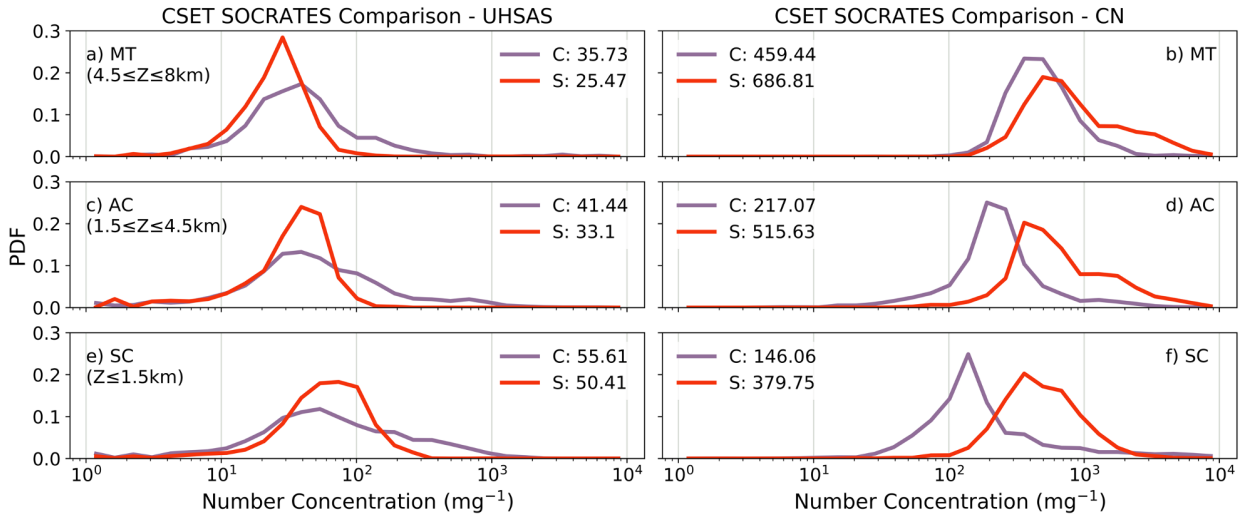

Figure 3-3 *PDFs of number concentrations for UHSAS100 (a, c, e) and CN (b, d, f) for different altitudes: mid-troposphere (a, b), above cloud (c, d), and sub-cloud (e, f). SOCRATES observations (orange) are contrasted with CSET observations (purple).*

If local wind-driven sea-spray production was primarily responsible for driving below cloud aerosol number production, we would expect a higher ratio of accumulation to Aitken mode aerosol concentration in SOCRATES where winds were stronger compared to CSET. However, this is opposite to our observations (Figure 3-3e, f) which suggests that primary aerosol production is not the largest contributor to the heightened aerosol concentrations in the SO. While number may not be linked to wind speed production, increased surface gas emissions associated with

higher wind speeds [*Lana et al.*, 2011] may still be assisting in secondary aerosol production and in growing SO aerosols.

In CSET, much more than in SOCRATES, the relative humidity was typically low (10-50%) at 6 km, implying a height of last saturation above 8 km, consistent with outflow from deep convective clouds [*Clarke et al.*, 1998; *Williamson et al.*, 2019] or midlatitude cyclones. Previous studies imply that particles generated in this outflow coagulate as they slowly descend [*Clarke et al.*, 1998; *Williamson et al.*, 2019], which may lead to the higher UHSAS100 concentrations aloft during CSET (Figure 3-3a). This aging process would also explain the lower frequency of high CN concentrations for CSET in the MT and AC compared to SOCRATES (Figure 3-3b, d). The higher SOCRATES concentrations indicate SO aerosol is more recently formed at these levels while CSET is sampling aging aerosols as they descend from nucleation events above 6 km. The vertical aerosol concentration gradients in CSET suggest coagulation and growth processes occur more significantly in the sub-tropics than the SO: UHSAS100 pdfs shift to larger concentrations and CN to smaller concentrations with descent during CSET. Hints of this process are seen in SOCRATES but they are muted compared to CSET (e.g. compare Figure 3-3c, d to e, f).

3.3.1.2 Evidence for Particle Generation through Synoptic Uplift Mechanism

We have established that there are frequent and remarkably high concentrations of small, Aitken mode aerosol particles occurring in the lower free troposphere over the Southern Ocean. But how are they forming? Based on previous studies in the SO [*Clarke et al.*, 1998], it is likely that the outflow regions from low, cumulus clouds are contributing to the high Aitken mode concentrations observed above cloud (~3 km) during SOCRATES. This mechanism does not explain the high Aitken mode concentrations observed in the mid-troposphere (~6 km) or the high concentration of particles observed at the surface. In the sub-tropics and mid-latitudes, new

particles have been observed in outflow regions of deep convection [*Kerminen et al.*, 2018]. However, high concentrations of small particles were observed on most SOCRATES flights and across a range of weather regimes with little evidence of recent penetrative congestus convection upstream. There was also little evidence of sub-cloud particle formation signatures during SOCRATES.

Based on evidence gathered during SOCRATES and a synthesis of evidence presented in the literature (1), we propose that a novel variant of the cloud-outflow mechanism for particle formation is at work in the SO: new particles are formed and dispersed after boundary-layer air is lifted and processed through precipitating clouds forming in regions of synoptic scale ascent. Two vital steps for gas to particle formation are occurring in this synoptic-uplift mechanism: i) the total surface area of the particles in the air is being reduced through uplift and rain out associated with clouds and ii) DMS lofted from the surface is given the opportunity to undergo photochemical reactions and nucleate into new particles rather than depositing onto existing aerosol particles. Increased actinic flux and cold temperatures experienced aloft in cloud outflows also assist the photochemical processing of DMS oxidation products and encourages particle formation. This mechanism is consistent with earlier observations of new particles and sulfuric acid vapors in the outflow of a frontal system off of Tasmania at ~6 km during ACE-1 [*Weber et al.*, 2001].

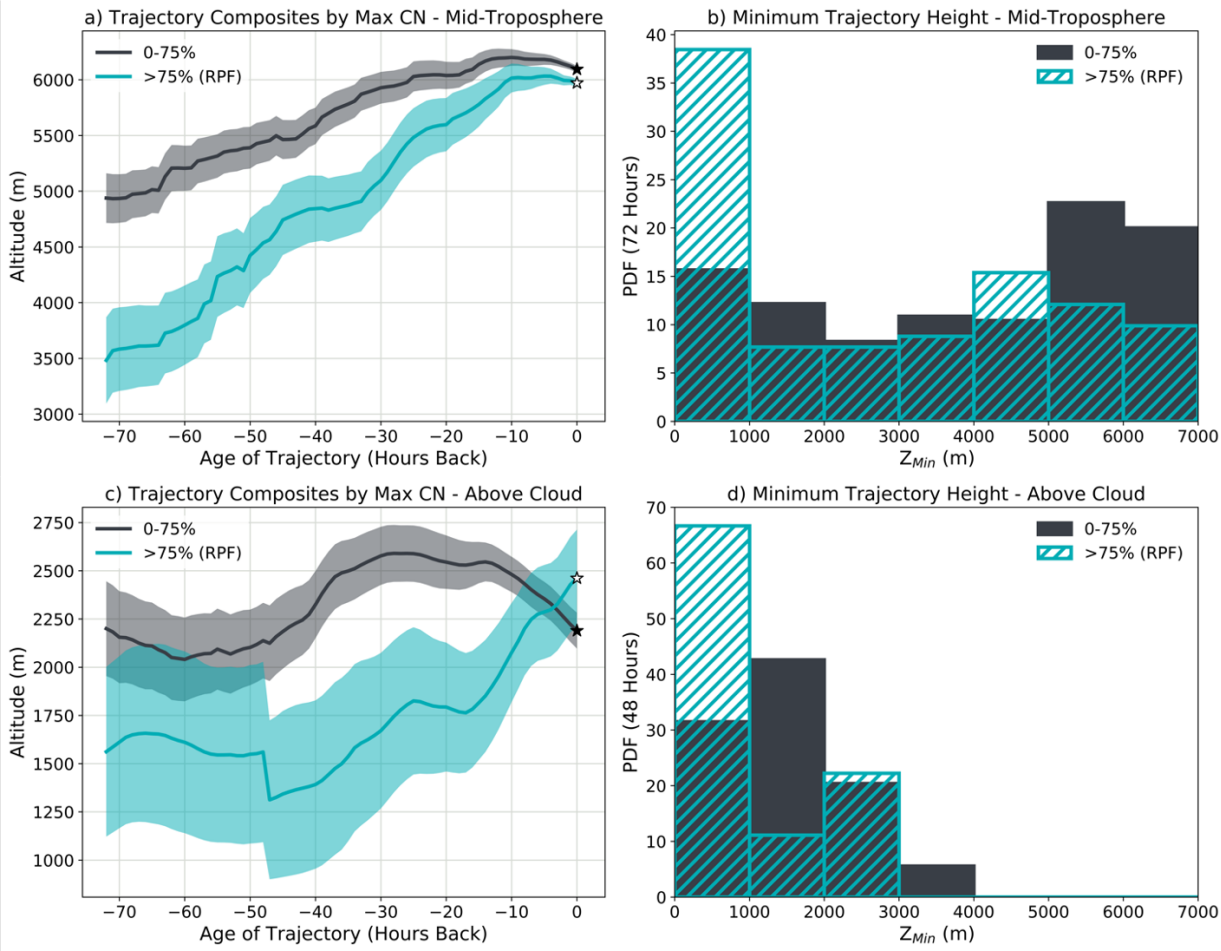

Figure 3-4 *Mean (line) and corresponding standard error (shading) of ascent profiles for HYSPLIT trajectories initiated in the mid-troposphere (a) and above cloud (c). Corresponding distribution of minimum height over proceeding time where altitude profiles are statistically distinct: 72-hours for mid-troposphere (b) and 48-hours for above cloud (d). Trajectories are composited by* CN_{Max10} *into RPF events (blue,* CN_{Max10}*>75%) and non-RPF events (gray, 0-75%* CN_{Max10}*). Number of RPF vs non-RPF cases per SOCRATES research flight for mid-troposphere and above-cloud are shown in Figure SI 3- 1.*

To test the synoptic uplift mechanism, we examine the altitude history of the mid-tropospheric air masses sampled in SOCRATES using RPF and non-RPF identified HYSPLIT 72-hour back trajectories (Figure 3-4a, b) (3.2.2). RPF air masses typically have a much steeper composite ascent profile over the past 72-hours compared to the non-RPF composite profile

(Figure 3-4a). During the ascent period (10 to 70 hours back), the rate of ascent of the RPF cases (1.1 cm s^{-1}) is comparable with the characteristic vertical velocity for mid-latitude synoptic systems (~1 cm s^{-1}) [*Hakim*, 2013] while the non-RPF cases are slower (0.6 cm s^{-1}). The depth and the steepness of the ascent is a marker of uplift through clouds, which will result in cloud processing and precipitation removal of accumulation and coarse mode aerosol in the air masses. RPF cases also come from below 1 km more frequently in the proceeding 72 hours compared to non-RPF cases (Figure 3-4b). This indicates that RPF trajectories are able to source the necessary precursor gases (e.g. DMS) from the boundary-layer for gas to particle conversion to take place.

Above cloud RPF events are similarly examined (Figure 3-4c, d). There is a clear distinction between the RPF and non-RPF cases in the 48 hours prior to sampling: RPF cases have rapid synoptic (1 cm s^{-1} in the last 20 hours) and presumably saturated ascent profiles (Figure 3-4c) and come from below 1km (Figure 3-4d). On average, the non-RPF trajectories undergo less total ascent, do not come from as near the surface, and ascend earlier. The latter results in longer residence time in the boundary layer where Aitken aerosols grow and coagulate to accumulation mode sizes, depleting their CN.

What are the large-scale synoptic patterns leading to rapid uplift over the SO? We employ ECMWF ERA-5 reanalysis to understand the large-scale motions associated with the HYSPLIT trajectory ascents. RF07 is used as an example case for identifying synoptic patterns because many RPF back-trajectories were identified from the 6 km survey leg during RF07, each with a rapid ascent profile (Figure 3-5a). Rapid ascent from the boundary layer occurred in two periods, one at ~60 hours (Figure 3-5b) and the other at ~36 hours (Figure 3-5c) prior to GV sampling. We use vertical velocity and geopotential height fields at 700 hPa (chosen as a representative mid-level altitude) to identify the cause of uplift: a warm conveyor belt (WCB). A representative geopotential

height contour traces the backbone of the eastward propagating Rossby wave occurring in the Southern Ocean during this case. The complete 72-hour evolution of this case is included as an animation of maps in 3 hourly snapshots (Movie SI 3- 1). At 60 hours back (Figure 3-5b), a tongue of warm, moist air from the sub-tropics is advected up and poleward ahead of the cold front, lifting the boundary layer air up towards the mid-troposphere (42°S, 54°E). At 36 hours back (Figure 3-5c), trajectories near the phytoplankton-rich ocean off the edge of Antarctica (60°S, 100°E) undergo uplift associated with the remains of the WCB that has traveled along the Rossby wave.

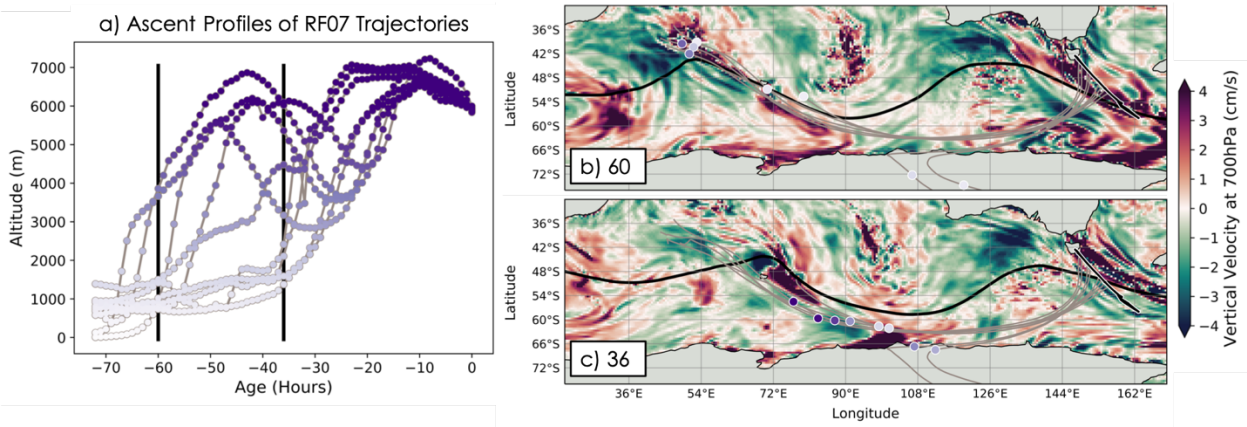

Figure 3-5 *Illustration of synoptic scale patterns influencing mid-tropospheric RPF identified air masses sampled by RF07 (black line from Tasmania, b and c). Two times of uplift are highlighted in the ascent profiles (black lines, a) and shown in reanalysis snap shots: 60 (b) and 36 (c) hours back from time of GV sampling. ERA5 reanalysis maps include 700 hPa vertical velocity (colors) with a 700 hPa geopotential height contour of 2.9 km for reference (black contour). In general, the contour separates warmer, moister sub-tropical air from cooler, drier polar air. RPF trajectories (gray lines) with air mass locations (circles) colored by their altitude (white to purple, as in the ascent profiles in a). Ascent of the first set of trajectories at 60-hr (b) occurs off the tip of Africa while ascent of the 36-hr trajectories (c) occurs off the coast of Antarctica, both driven by the advance of a warm-conveyor belt towards the south east (i.e. along the height contour). Note sub-polar vortices affecting the vertical velocity in c) at 60°S, 72°E and 54°S, 140° E. Animation of RF07 synoptic event included in supplemental material (Movie SI 3-1).*

The WCB during RF07 generated regions of potential vorticity anomalies resulting in upward motion. While they did not affect the trajectories sampled during RF07, sub-polar vortices (e.g. 60°S, 70°E and 54°S, 140°E, Figure 3-5c) lead to uplift of boundary layer air to the mid-troposphere in other research flight cases. We concluded from analysis of all SOCRATES flights that the uplift along RPF trajectories is typically associated with either warm conveyor belts or sub-polar vortices.

In the southern hemisphere, WCBs are not always associated with cyclones [*Catto et al.*, 2015]. Climatology of WCB features show a high frequency of events occurring off the tip of South America and South Africa [*Catto et al.*, 2015]. WCBs are also not as constrained in longitude in the Southern Hemisphere as in the Northern Hemisphere and occur frequently across a wide range of longitudes in the SO [*Eckhardt et al.*, 2004]. The behavior of mid-tropospheric RPF trajectories is consistent with both these characteristics of WCB behavior in the SO: i) the typical RPF trajectory path arcs down from South Africa towards Antarctica, funneling along the large-scale waves in the region, and ii) the geographic location of minimum RPF trajectory altitude is widespread across the SO (Figure SI 3- 2).

Synoptic-scale uplift is frequent over the Southern Ocean and can set the stage for new particle formation aloft. The pattern of minimum RPF trajectory altitude is similar to the pattern of climatological DMS fluxes for January and February, with particular hotspots occurring off the tip of Africa, edge of Antarctica, and, in general, to the west of Australia and up-wind of the SOCRATES sampling locations [*Lana et al.*, 2011]. The collocation of synoptic uplift regions and DMS-rich boundary-layer air provides the precursor gases and aerosol cleansing necessary for frequent occurrence of gas to particle formation in the free troposphere and ensures that RPF is widespread across the SO. We propose that this mechanism frequently produces new particles

throughout the lower free troposphere. Figure 3-6 presents a conceptual diagram for aerosol cycling over the SO associated with this uplift mechanism and the cumulus outflow mechanism, augmented from a similar diagram in *Clarke et al.* [1998].

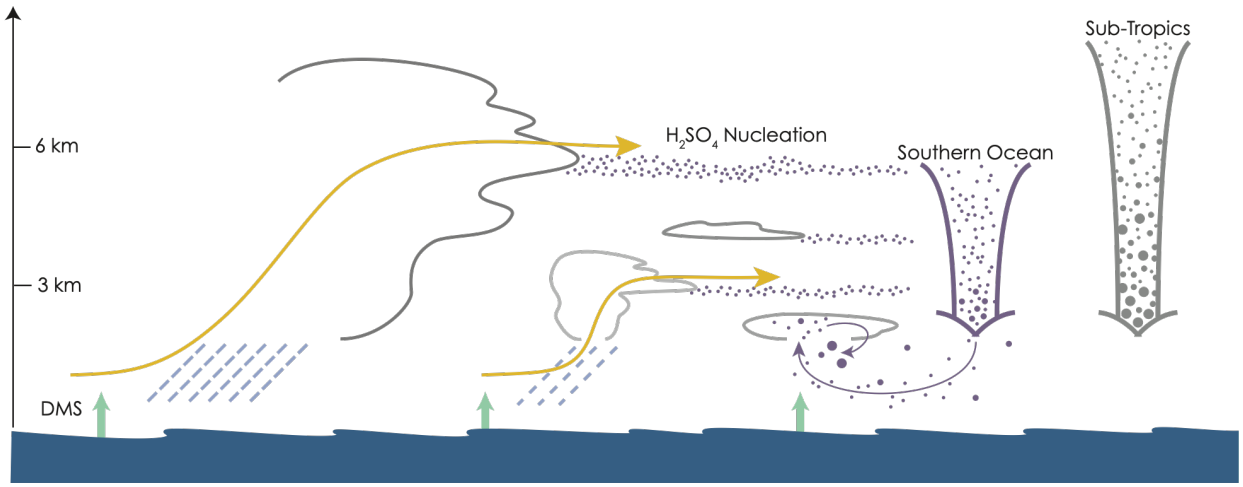

Figure 3-6 *Diagram of synoptic uplift mechanism for generating new particles. As in Clarke et al. [1998], differences in the distribution of aerosols between the Southern Ocean (purple) and sub-tropics (gray) are highlighted.*

3.3.1.3 Southern Ocean Summertime Aerosol Composition Estimations

If new particle formation generated through synoptic uplift (Figure 3-6) is significantly impacting the formation of free tropospheric aerosols, we expect to find signatures of DMS oxidation products in the particles sampled. In this section, we use ambient aerosol measurements from the CVI (3.2.1) to illuminate the likely composition of summertime SO aerosols sampled by SOCRATES. We draw two conclusions from this analysis: i) Aitken and small accumulation mode ($\leq$ 200 nm) particles occurring in high number concentration samples in the free troposphere are composed primarily of H_2SO_4 with possible contributions from more volatile DMS oxidation products like MSA, and ii) accumulation-mode particles (~100-500 nm diameter) sampled above, below, and in-cloud are primarily sulfur-based with limited sea spray influence.

Our first conclusion is based in part on a particle volatility estimate drawn from the temperature evolution of the ratio between the condensation nuclei number concentration measured behind a heated CVI (CN_{CVI}) and the unheated measurement from the CN (Figure 3-7). During the campaign there was limited sampling where both high aerosol concentrations occurred and CVI temperatures were cycled, so our analysis expands beyond RPF cases to all instances where CN ≥ 800 mg^{-1}. However, we limit our examination to the free troposphere (Z ≥ 1.5 km) because i) the majority of the CVI temperature cycling experiments occurred in this altitude range and ii) our interest is primarily in the Aitken-mode dominated environments. Median cumulative distributions (3.2.1) are calculated for each above cloud and mid-tropospheric level leg during the campaign (Figure SI 3- 3). These demonstrate that free-tropospheric altitudes are dominated by Aitken-mode aerosols (except for a few near-cloud contaminated samples marked by high relative humidity, Figure SI 3- 3b).

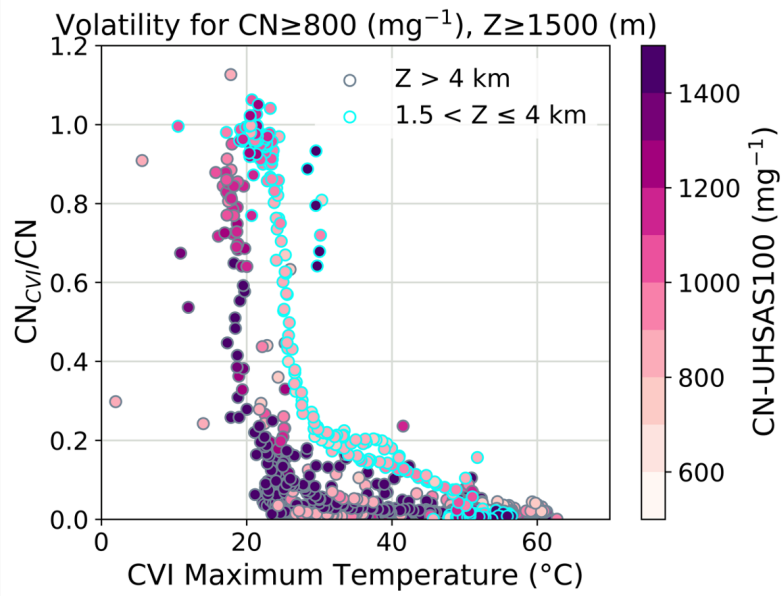

Figure 3-7 *Volatility curves from CVI analysis presented as the ratio between CN and CN_{CVI} versus the maximum temperature of the CVI instrument. Points are shown for CN ≥ 800 mg^{-1} above which the small particle concentration is large enough to mark RPF or slightly grown nucleation*

mode aerosol. Points are limited to free tropospheric samples (Z ≥ 1.5 km) due both to limited temperature cycling in the boundary layer and to targeting Aitken mode dominated environments. Outline colors denote altitude of sample: mid-troposphere (gray) and above cloud (blue). Points are colored by CN-UHSAS100 to estimate the number of particles in the Aitken mode (generally more in the mid-troposphere).

The free-tropospheric, Aitken dominated samples contain predominantly volatile particles. This is exhibited by the decrease in CN ratio with increasing CVI temperature (Figure 3-7) when the ambient particles (temperatures between -20 and -15°C in the mid-troposphere, -5 and 0°C above cloud) are exposed to CVI temperatures between ~25-60°C, taken as the maximum of several temperature measurements in different parts of the instrument configuration (3.2.1). The most dramatic number decrease in particles measured by CN_{CVI} occurs when maximum temperatures are above ~25-30°C. The volatilization of Aitken mode particles under this imposed CVI temperature range is consistent with previous volatility analysis for small particles primarily composed of sulfuric acid. *Orsini et al.* [1999] measured the volatility of H_2SO_4 as a function of particle size and found that small particles volatilize at much lower temperatures than larger particles, with a more than 30% decrease in diameter for 15 nm particles at 25ºC. *Clarke* [1991] observed that sulfuric acid particles with mass mean diameters of 300 nm began losing mass at about 30°C (disappearing completely by 125°C). Conversely, compounds like neutralized sulfate (e.g. ammonium sulfate) and sea spray aerosol (e.g., NaCl) volatilize at much higher temperatures (> ~200, ~300°C respectively) than H_2SO_4 [*Schmid et al.*, 2002] and thus are unlikely to contribute to the composition of the particles sampled here. This is consistent with other SO observations showing new particle formation largely produces sulfuric acid particles [*Clarke et al.*, 1998; *Weber et al.*, 2001; *Yu and Luo*, 2010] and suggests H_2SO_4 dominates particle composition in the SO free troposphere.

For the limited temperature range maintained over the CVI sample lines during SOCRATES (~25-60°C), we do not expect all sizes of particles to evaporate completely (i.e. shrink below the 11 nm detection threshold of the CN counter) if they are composed purely of sulfuric acid. *Orsini et al.* [1999] found that sulfuric acid particles initially ≥ 35 nm in diameter required exposures to temperatures over 90°C for ~0.2 seconds before their diameters were reduced below 11 nm. For the longer residence time during SOCRATES (~2 seconds), it is likely the temperature required for sub-detection limit volatilization will be reduced but not to below 35°C. Based on this and the strong volatility of Aitken-dominated samples at ~25-30°C (Figure 3-7), we conclude that if the Aitken mode particles are composed predominantly of sulfuric acid then the majority of particles must be ≤ 20 nm in diameter. This is similar to the size of particles *Orsini et al.* [1999] found evaporated below 30°C and is consistent with findings by *Schmid et al.* [2002] for very small sulfuric acid particles. Unfortunately, a more nuanced discussion of particle volatility by size is not possible for Aitken mode aerosols during SOCRATES due to instrument limitations.

Volatility signatures were also noted in the size-resolved accumulation mode UHSAS measurements during the campaign which provides some additional insight into particle composition. There are very few accumulation mode particles contributing to the Aitken-dominated free-tropospheric samples analyzed in this section (on the order of 50 mg^{-1} or less, Figure SI 3- 4b) and most are ≤ 200 nm (Figure SI 3- 3). However, enough UHSAS100 aerosols were sampled during CVI temperature cycles to conduct a limited examination of accumulation mode volatility using a matching ratio analysis to Figure 3-7 (Figure SI 3- 4). The UHSAS100 ratio is found to exhibit a decrease near ~25-30°C, similar to the CN ratio although likely noisier due to the small number of accumulation mode particles sampled. The similarity of the temperature inflection point for these two volatility ratio curves suggests that small accumulation mode

aerosols may share their composition with Aitken aerosols in these high aerosol concentration events and that volatile DMS oxidation products are likely the leading contributor to the composition of the few accumulation mode aerosols occurring in the FT (Figure 3-3a, c).

Intriguingly, the magnitude of the change in particle size in the small accumulation mode range (shrinking from 100-200 nm to below 100 nm) possibly signals the presence of aerosol species with even higher volatility than sulfuric acid [*Orsini et al.*, 1999]. The most likely candidate for an additional, volatile species contributing to particle composition over the SO is MSA, another DMS oxidation product and one with a higher vapor pressure than H_2SO_4 [*Mauldin et al.*, 1999; *Berresheim*, 2002]. Relatively large MSA particles (160-260 nm) have been found to volatilize at ~50-60°C [*O'Dowd et al.*, 1997]. It is thus possible for small, recently formed MSA particles to evaporate at 30-35°C with the increased SOCRATES CVI residence time. MSA may also be contributing to the separation between the above cloud and mid-tropospheric volatility curves (Figure 3-7, Figure SI 3- 4). The mid-tropospheric observations from SOCRATES found higher concentrations of Aitken particles (~CN-UHSAS100, colors in Figure 3-7, Figure SI 3- 4a), which may mark less coagulation and growth occurring after particle formation and resulting in smaller, more volatile particles. However, mid-tropospheric particles reside at lower ambient temperatures and slightly lower relative humidity (Figure SI 3- 3a) as well. If MSA is present, this environment could drive MSA to partition preferentially to the particulate phase [*Berresheim*, 2002] where it could dominate the volatility response. Future campaigns outfitted with instruments capable of measuring gas composition and aerosol concentrations with Aitken mode size resolution will help to further demystify these volatility signatures.

We can gain broader insight into accumulation mode particle composition across the SOCRATES campaign from STEM analysis of micro-impactor filters taken during ambient CVI

sampling [*Twohy et al.*, 2020 submitted]. Sulfur-based particles are found to dominate the number concentration in the accumulation mode (~100-500 nm) at all altitudes during the SO summer. The remaining number fraction (20-30%) is composed of salt-based sea spray, sometimes enriched with sulfur or other trace compositions, and have a smaller influence on particles sub- and in-cloud compared to the sulfur-based particles. If small amounts of organic material occur in these samples, they are not detectable on the carbon STEM substrate. The composition of these accumulation-mode particles is what one would expect to observe from the growth of sulfuric acid or other DMS oxidation product sourced Aitken mode aerosols and is consistent with our volatility analysis. Implications of Aitken particle growth into accumulation mode sizes will be discussed further in section 3.2.2.

3.3.2 *Controls on Southern Ocean Aerosol and Cloud Droplet Number Concentrations*

3.3.2.1 Average Southern Ocean Aerosol and N_d Structures

To better understand the factors influencing the generation and depletion of aerosols and cloud droplets in the SO and how synoptically generated Aitken particles influence the SO aerosol budget, it is useful to examine the spatial distribution of aerosol and cloud features. Using the altitude by latitude binning methodology (3.2.1), a multi-flight, campaign average composite is generated for aerosol and cloud droplet number concentrations (Figure 3-8).

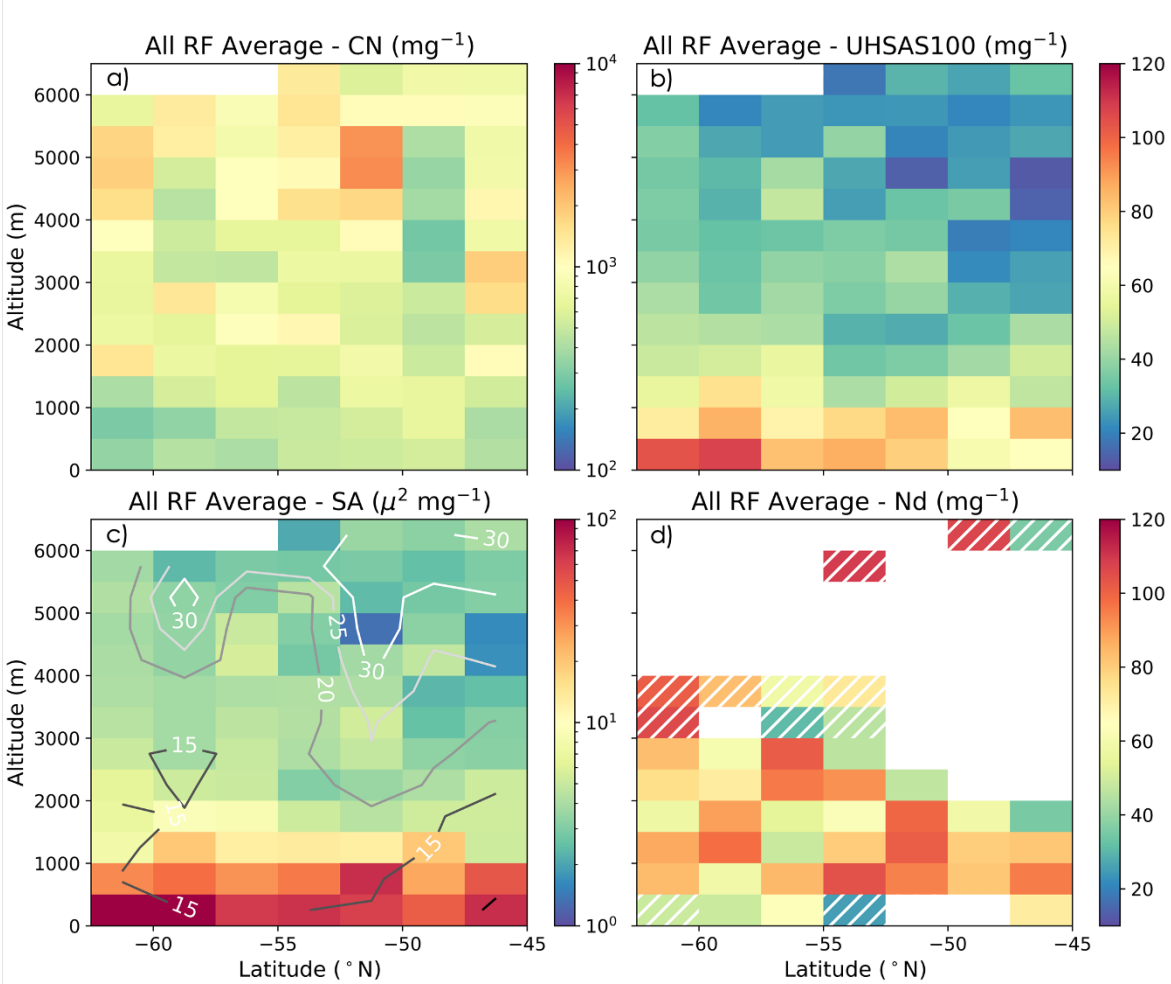

Figure 3-8 *All flight average composites of binned flight medians for 500m x 2.5° boxes. Aerosol variables are screened for cloud and rain contamination. Number concentrations for (a) total aerosol, (b) accumulation mode aerosol, and (d) cloud droplets are shown along with (c) the surface area concentration computed from accumulation and coarse mode size distributions. Contours of all flight average composite wind speed are also included (c). Bins where 2 or less flights sampled are hatched to indicate reliability of sampling. A companion plot to (d) of cloud droplet number concentration in cm^{-3} units is in Figure SI 3- 5.*

The mean SO CN does not vary significantly with latitude and maintains particle concentrations on the order of 1000 mg^{-1} above cloud (≥1.5 km) and 600 mg^{-1} in the boundary layer (<1.5 km) (Figure 3-8a). This is consistent with the altitude trend in the CN histograms

shown in Figure 3-3 (d, e, f). The prevalence of consistent high concentrations of CN in the free troposphere across all latitudes suggests that the synoptic generation mechanism (3.3.1) is influential to the Aitken mode concentration throughout the SO.

The accumulation mode aerosol (Figure 3-8b) and surface area derived from the UHSAS and CDP (Figure 3-8c) both decrease significantly with altitude and have the largest values in the near-surface bins. Aerosol surface area is higher near the surface due to sea spray production (Figure 3-8c). There is a slight increase in both surface area and UHSAS in the two most southerly surface bins potentially associated with enhanced wind speed (contours, Figure 3-8c). However, this does not appear to influence sub-cloud UHSAS (500-1000m).

Surface area is consistently low enough (SA< 10 μm^2 mg^{-1}) above 2 km to support gas to particle conversion [*Covert et al.*, 1996]. The one exception to this was during RF13 under an anticyclonic ridge, where a narrow rift of precipitating shallow cumuli was embedded in an extensive stratocumulus layer. In this instance, low SA and high, variable CN were observed in the rift but not the surrounding stratocumulus-capped MBL.

Droplet number concentration does not have a clear latitudinal dependence but varies with altitude (Figure 3-8c). A small latitudinal gradient in this portion of the SO is expected based on MODIS climatology (Figure 2-2) [*McCoy et al.*, 2020]. The observation number and spatial distribution of in-cloud sampling during SOCRATES may be insufficient to capture the nuances of cloud behavior, masking this gradient. Cloud observations occur in more altitude bins to the south, possibly a manifestation of the more frequent occurrence of multi-layered clouds in the south of the SO although, again, sampling uncertainties should be considered. Most bins average N_d between 60 and 100 mg^{-1} (approximately the same range in cm^{-3}, see Figure SI 3- 5), similar to climatological N_d from MODIS satellite retrievals in this region and season [*Grosvenor et al.*,

2018b; *Bodas-Salcedo et al.*, 2019; *McCoy et al.*, 2020]. This summertime concentration is much higher than the average boundary-layer N_d sampled in the austral winter slightly to the north of this region (~32 cm^{-3} between 43-45°S) [*Ahn et al.*, 2018]. This seasonality is consistent with previous work connecting N_d increases with more availability of DMS products and other biological aerosol sources in the SO summertime [*Ayers and Gras*, 1991; *Boers et al.*, 1998; *McCoy et al.*, 2015].

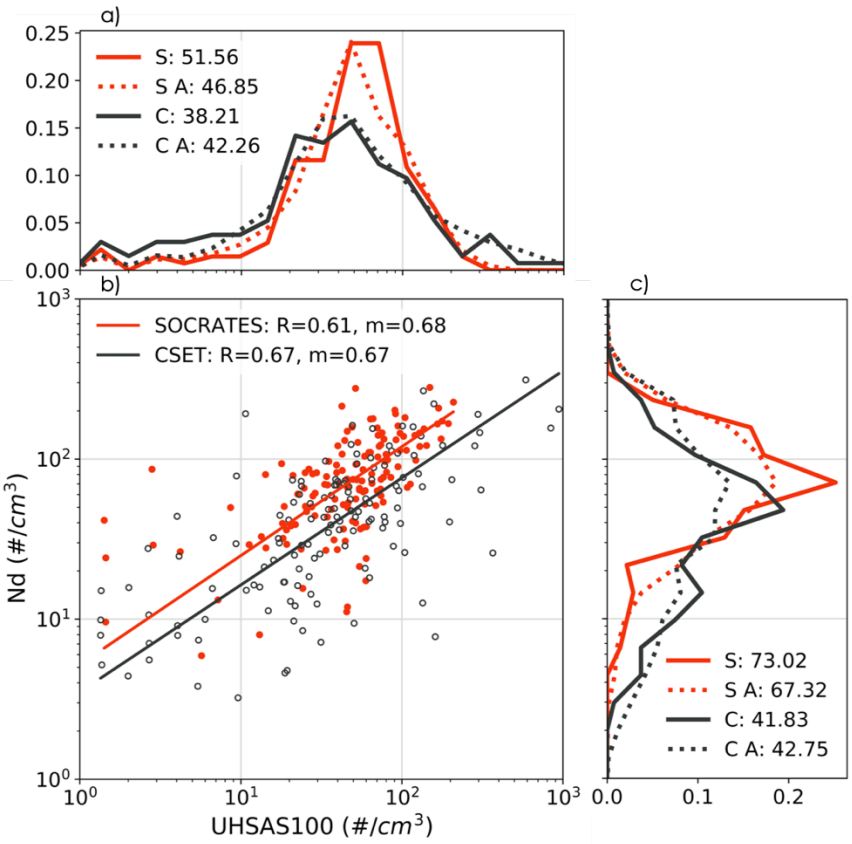

Figure 3-9 *Relationship between accumulation mode and cloud droplet number concentrations in SOCRATES (orange) and CSET (gray). (b) Altitude vs Latitude (SOCRATES) or Longitude' (CSET) 500m x 2.5° bin medians for N_d and UHSAS100 are computed for each flight and compared. PDFs of binned data are shown for (a) UHSAS100 and (c) N_d as solid lines. PDFs of raw flight data for the campaigns are shown as dashed lines (a, c) and agree with the behavior of the binned subset. Corresponding median values are included for reference. Few instances of precipitation-depleted N_d or N_d-UHSAS100 points occur (≤ 10 cm^{-3}) in SOCRATES. CSET has a greater number of precipitation depleted cloud and aerosol features (b, c).*

What is the source of aerosol influencing N_d? The campaign average N_d is comparable to the sub-cloud UHSAS100 accumulation-mode aerosol concentration (Figure 3-8b, d). Spatially and temporally matched bins from individual flight composites for N_d and UHSAS100 are well correlated (R=0.62, Figure 3-9b). Distributions of bin matched and raw flight data match for N_d and UHSAS100, indicating bin averages are representative of cloud and aerosol tendencies (Figure 3-9a, c). Level-leg median N_d measurements are additionally found to have a stronger relationship with median sub-cloud level leg UHSAS100 (R=0.64) than with above-cloud UHSAS100 (R=0.40). We conclude from these relationships that SO N_d is controlled by sub-cloud accumulation mode aerosol. Thus, a more appropriate question is: what is the source of *sub-cloud* aerosol in the SO that influences N_d?

For guidance in answering this question, we can look to another cloudy marine environment heavily influenced by mid-latitude storms and biologically active aerosols: the North East Atlantic (NEA). Recent observations in the NEA found free tropospheric Aitken mode particles descending into the boundary layer and subsequently growing to accumulation modes sizes through surface gas absorption and cloud processing [*Sanchez et al.*, 2018; *Zheng et al.*, 2018]. Similar behavior may be occurring in the SO. The pattern of CN and UHSAS concentrations as well as the heightened SA sub-cloud during SOCRATES suggests i) recent particle formation is the primary contributor to high CN in the free troposphere (UHSAS100 low, CN high) and ii) it is unlikely that there is a strong surface source of CN generating the Aitken particles seen above cloud (CN low sub-cloud, high above-cloud; SA sub-cloud too high for gas to particle conversion). We speculate that CN is depleted through in-cloud processing and growth to UHSAS sizes, reducing to the lower concentrations observed in the boundary layer (600 mg^{-1}). Observations of

particle movements during SOCRATES are limited due to the instantaneous nature of the GV sampling, but earlier literature discussed Aitken particles descending from the free troposphere and influencing SO boundary layer aerosol [*Covert et al.*, 1996; *Humphries et al.*, 2016]. Using a global chemical transport model, *Korhonen et al.* [2008] estimated that FT DMS-oxidation product based new particles (i.e. H_2SO_4) entrained into and grown in the MBL contributed between 43-65% of zonal mean CCN in the SH summertime oceans. This was also determined the dominant microphysical pathway for DMS to influence SH marine CCN. In the next section, we examine SOCRATES observations to further assess the importance of the FT Aitken source on SO summertime sub-cloud CCN concentrations.

3.3.2.2 Sources of Accumulation Mode Aerosol in the Southern Ocean

We have established that sub-cloud aerosol is significant in controlling cloud droplet number concentration. However, we do not as yet understand the source of this aerosol in the SO. We broadly expect accumulation mode aerosol to be developed from i) primary sea spray emissions from the surface or ii) growth from secondary aerosol emissions such as Aitken mode aerosols (either from the boundary layer or free troposphere). To understand which of these behaviors is dominating, we begin by calculating a cumulative size distribution for sub-cloud aerosol and examining its characteristics (Figure 3-10). A median cumulative distribution (3.2.1) is developed for each sub-cloud level leg on each flight and colored by the corresponding median wind speed. Wind speed is a common proxy for estimating sea spray production from waves and sea spray [*Grythe et al.*, 2014] as well as the magnitude of surface gas fluxes. Correlations are calculated between wind speed and the log of the cumulative number concentration at intervals to understand the importance of wind-speed mechanisms at different sizes.

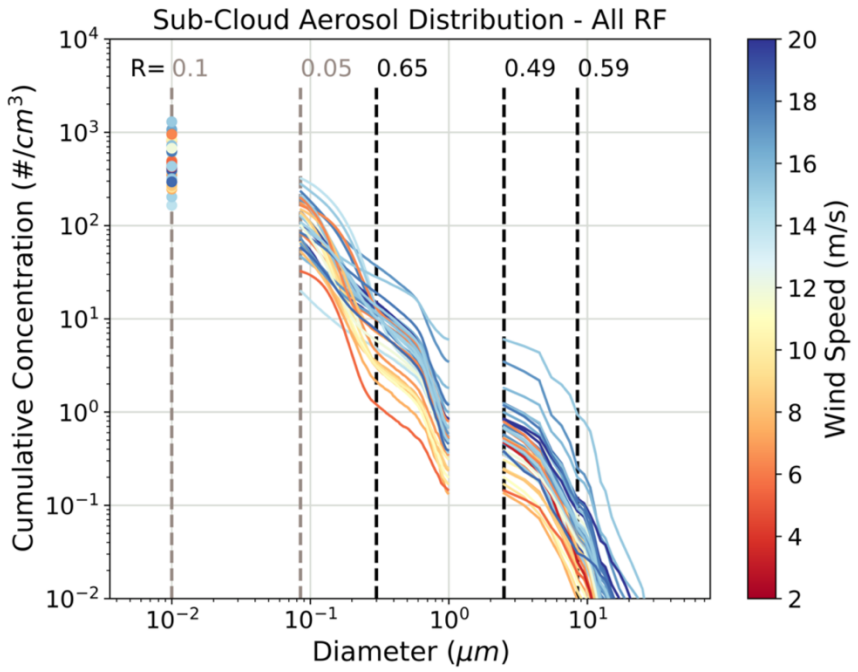

Figure 3-10 *Cumulative size distribution for sub-cloud aerosol sampling colored by wind speed at the aircraft (~150 m). Aerosol number concentrations from CN (dots), UHSAS (accumulation, middle curves), and CDP (coarse, right curves) are screened for cloud and drizzle. Cumulative distribution is summed from the right to the left where CN equals the total number concentration. Correlation coefficients computed between wind speed and the log of the cumulative number concentrations to the right of the dashed lines (gray for not significant and black for significant at 95% confidence) indicate weakening relationship between wind speed and log_{10}(cumulative aerosol number concentration) with a decrease in diameter.*

The most notable finding from these wind speed correlations is that wind-speed production mechanisms are an insignificant contribution to overall sub-cloud accumulation mode and Aitken mode concentrations. Coarse mode aerosol number (CDP, 3-30 μm) is positively correlated with wind speed, consistent with the larger SA at the surface and in the southerly bins in Figure 3-8c. Within the CDP range, the wind speed correlation weakens as aerosol sizes decrease to the accumulation mode range (UHSAS). They then increase again for the larger UHSAS sizes (0.3-1 μm). This suggests particles in these larger size ranges are linked to sea spray production

mechanisms, consistent with earlier studies [*Grythe et al.*, 2014]. Organics may become more significant in sea-spray in the large accumulation size range or sub- and in-cloud growth of Aitken particles could be enhanced by increased fluxes of DMS associated with high wind speeds [*Lana et al.*, 2011]. However, with the addition of the smaller UHSAS sizes and an order of magnitude growth in number, the correlation disappears. The total aerosol concentration (CN), which additionally includes a larger number of Aitken mode aerosols, has no statistically significant relationship with wind speed.

If wind-speed generation mechanisms are not the source of the bulk of the sub-cloud accumulation mode aerosol (the number between 0.08-0.3 μm), where is it coming from? With the elimination of primary emissions as the source, it is likely the central source of CCN is growth of secondary particles. These may come either from above the boundary layer or within the boundary layer. Based on our previous analysis, Aitken mode production is limited in the boundary layer which suggests they are coming from the free tropospheric Aitken reservoir. If these particles were grown into accumulation mode sizes, they would be a significant source and would have little correlation with wind-speed, as we see in Figure 3-10. Growth could occur either through in-cloud processing or sub-cloud gas absorption of DMS-oxidation products.

We conclude that it is unlikely that sea-spray aerosols are the primary driver of SO CCN number in summer months. Aerosol composition analysis (3.1.3) supports this as the majority of particles (diameters 0.1-0.5 μm) above, in, and sub-cloud are found to be sulfur-based [*Twohy et al.*, 2020 submitted]. Influences of sea-spray are seen in the sub- and in-cloud particle samples, but they are secondary and often sulfur enriched. The dominant, sulfur-based composition of the particles is consistent with aerosols grown from DMS-oxidation products. Growth of accumulation mode aerosol from sulfuric acid Aitken mode aerosols, as suggested by our volatility analysis

(3.1.3), are very likely a significant contributor to SO CCN in summer. This is consistent with model estimates from *Korhonen et al.* [2008].

3.3.2.3 Influence of Aitken Mode Aerosols on Southern Ocean Summertime Cloud Droplet Number Concentrations

Our analysis demonstrates that sulfur-based aerosols have a more significant impact on SO cloud droplet number concentrations than sea-spray particles. Understanding the origin and influence of these sulfur-based aerosols is of primary importance for understanding summertime SO cloud-aerosol interactions. From the pattern of CN, UHSAS, and SA (3.3.2.1), it is unlikely that these sulfur-based particles are generated from a surface source alone. Instead, free tropospheric Aitken mode particles descending into the boundary layer and growing into accumulation mode sizes could be the missing source of CCN that we observe influencing summertime SO N_d.

Because of the large quantity of Aitken mode aerosol present in the free troposphere, if these particles are an important CCN source they are difficult to deplete. This ability to be replenished has significant implications for SO N_d which is known to have a large precipitation sink of N_d and CCN associated with the mid-latitude storm track. Despite the magnitude of this sink, high SO droplet number concentrations are maintained (N_d ~80-100 cm^{-3}) [*McCoy et al.*, 2020]. It is likely that a large and continuous source of aerosol exists in the SO that is able to maintain clouds against persistent collision-coalescence processes that would otherwise rapidly deplete N_d.

We see evidence of a reduction in precipitation depleted cloud and aerosol features in the Southern Ocean relative to a typical sub-tropical marine environment (Figure 3-9). Both SOCRATES and CSET sampled intermittently precipitating shallow cumulus and stratocumulus clouds: SOCRATES in SO cyclone cold sectors and CSET in the NEP stratocumulus to trade

cumulus transition. Similar near-cloud median accumulation mode aerosol concentrations occurred for SOCRATES (~50 cm^{-3}) and CSET (~40 cm^{-3}) when sampling far from continents (Figure 3-9a). Median N_d is higher and less variable during SOCRATES compared to CSET (~70 to 40 cm^{-3}, Figure 3-9c). The N_d-UHSAS100 space captures the cloud-aerosol interactions occurring in the NEP and SO and, not too surprisingly, show that in cloud N_d is well correlated with near cloud CCN measured by UHSAS100 in both environments (Figure 3-9b).

The breadth of the N_d CSET pdf (Figure 3-9c) is driven by the frequent occurrence of precipitation depleted clouds ($N_d \leq$ 10 cm^{-3}) in the cumulus regime west of 140°W. In N_d-UHSAS100 space, these precipitation-depleted cloud features are frequently collocated with depleted CCN (UHSAS100 $\leq$ 10 cm^{-3}). These features, referred to as "veil" clouds or "ultra-clean" aerosol layers in the literature, occur primarily at the detraining tops of cumulus clouds and are developed through droplet and aerosol number removal by collision-coalescence [*O et al.*, 2018; *Wood et al.*, 2018]. SOCRATES N_d is noticeably missing these precipitation-depleted occurrences despite sampling similar cloud structures (Figure 3-9).

Why do SO clouds have less precipitation-depleted cloud features? Accumulation mode aerosol is similar in both environments and NEP number concentration encompasses that observed in the SO (Figure 3-3, Figure 3-9). However, Aitken mode aerosol concentration is significantly different in these two regimes (sub-cloud median 146 mg^{-1} compared to 380 mg^{-1}, Figure 3-3). Are free tropospheric Aitken aerosols providing a continuous source for CCN development and thus helping to prevent N_d depletion as a result of persistently drizzling boundary-layer clouds? And if so, how is this N_d-buffering accomplished? We hypothesize one possible mechanism (Figure 3-11):

I. *Marine biogenic outgassing leads to the generation of widespread high concentrations of small Aitken-mode aerosols in the free troposphere via lifting, scavenging, and cloud outflow nucleation mechanisms (3.3.1).*

II. *Aitken-mode aerosols make their way into the SO boundary layer through horizontal and vertical advection and turbulent mixing (3.3.2.1).*

III. *Once in the boundary layer, these small aerosols grow to accumulation mode sizes through in-cloud processing or below-cloud gas absorption (3.3.2.2).*

IV. *This source of accumulation mode aerosol buffers SO summertime boundary-layer clouds against precipitation-induced depletion of cloud condensation nuclei, resulting in very infrequent occurrences of precipitation-depleted cloud features in SO summertime low clouds. Cloud brightness and longevity are maintained and susceptibility to anthropogenic aerosols is reduced.*

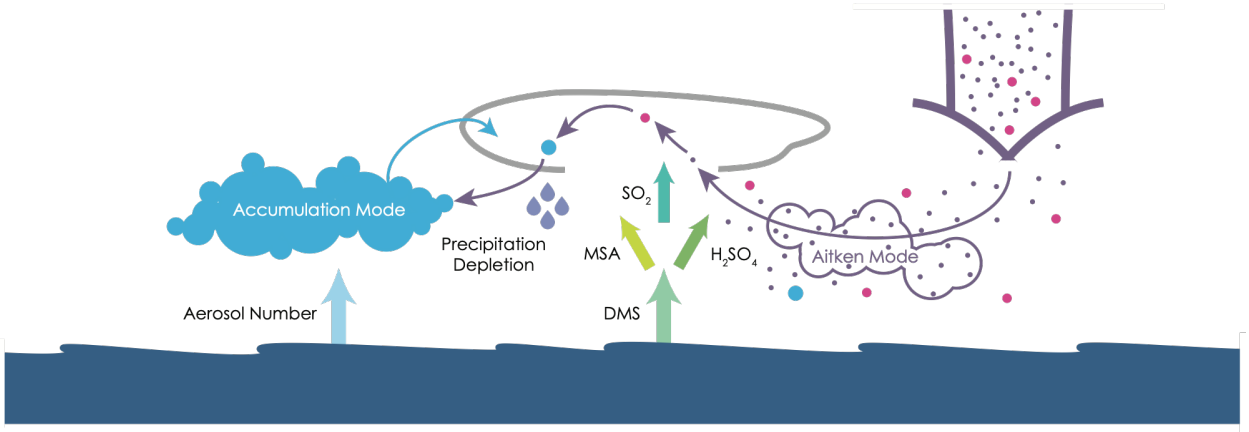

Figure 3-11 *Diagram illustrating hypothetical buffering mechanism for how Aitken mode aerosols influence Southern Ocean clouds and reduce precipitation depletion.*

We suggest that the summertime SO is a more aerosol-buffered environment than the summertime NEP, leading to elevated N_d during SOCRATES and a lack of precipitation-depleted features compared to CSET. The evidence presented in this and preceding sections support this

mechanism and, more broadly, are strongly suggestive of a more complex cloud-aerosol interaction taking place in the summertime SO than hitherto discussed. However, we acknowledge that more observational analysis and process modeling is required to determine whether high Aitken mode aerosol concentrations are an important driver of SO N_d characteristics. A further assessment of the validity of these steps and the observations still needed to test this mechanism is presented in the discussion.

3.3.2.4 Evaluating Southern Ocean Cloud-Aerosol Interactions in Global Climate Models

Recent satellite comparisons revealed that many state of the art climate models under-predict N_d over the Southern Ocean [*Mulcahy et al.*, 2018; *Bodas-Salcedo et al.*, 2019; *Revell et al.*, 2019; *McCoy et al.*, 2020]. Identifying where there are significant inconsistencies between observed and modeled cloud and aerosol characteristics will help in diagnosing the underlying cause of this bias. With this purpose, we compare meteorologically nudged CAM6 hindcasts that use prognostic aerosols and cloud droplet concentrations (3.2.3) with matched *in situ* observations from the SOCRATES flights. We include an additional model-observation comparison with CSET flights for a sub-tropical baseline of model ability. Testing GCMs using this nudged framework helps us to understand what mechanisms may be contributing to the current N_d bias in models and other discrepancies in cloud-aerosol interactions while ensuring that differences in the large-scale meteorology are small between the simulation and reality.

The Aitken buffering mechanism (3.3.2.3) is a useful framework for interpreting cloud-aerosol interactions in CAM6 and comparing to observed tendencies. We utilize the N_d-UHSAS100 space previously introduced for observing cloud-aerosol interaction tendencies (Figure 3-9b) to test cloud responses to adjacent aerosol in CAM6 hindcasts for CSET and SOCRATES (Figure 3-12c, d). Observations and collocated CAM6 output for each flight during

CSET and SOCRATES are binned into 500 m by 2.5° bins (3.2.1). Comparisons are for bin-matched data where Z ≤ 4 km, samples are at a distance from continental effects, and both observations and model data are available.

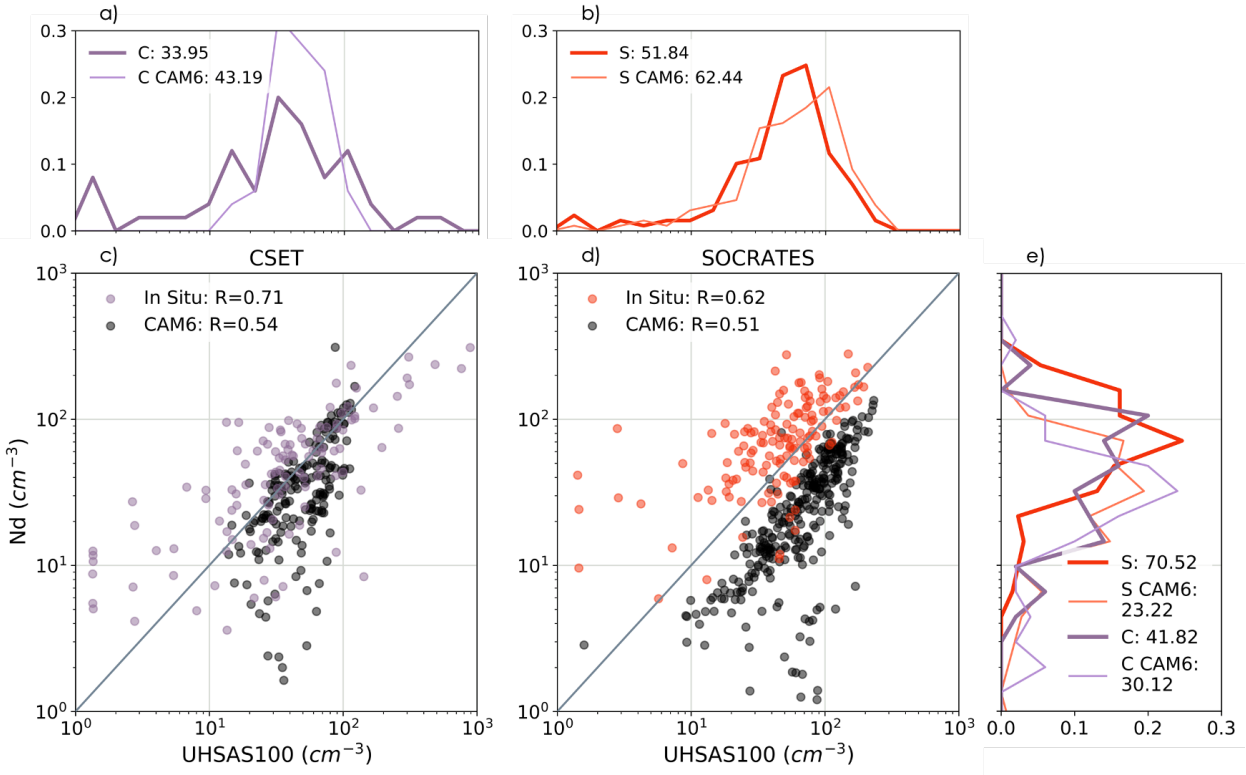

Figure 3-12 *CAM6 (black) and observational (color) comparison for N_d-UHSAS100 relationship from collocated binned composite values for each flight during CSET (c) and SOCRATES (d). Data is taken for Z ≤ 4 km and in pristine regions: Latitude south of 45°S (SOCRATES) and Longitude' west of 130°W. Corresponding PDFs of aerosol-droplet occurrence for matched binned values occurring for the model and observational data are shown along with median values for UHSAS100 (a, b) and N_d (e).*

CAM6 consistently underpredicts SOCRATES N_d (model median 23 compared to observed median 70 cm^{-3}, Figure 3-12e) with little linear correlation to bin matched observations (R=0.26, Figure SI 3- 6). Surprisingly, the pdf for bin-matched accumulation mode concentrations is very similar to the observations (62 to the observed 52 cm^{-3}, Figure 3-12b). However, CAM6

poorly captures the observed relationship between N_d and UHSAS100 during SOCRATES (log-log correlation of 0.51 is lower than the observed 0.62) (Figure 3-12d). This is both due to the low N_d bias and over-produced precipitation-depleted cloud features ($N_d \leq 10$ cm^{-3}) in the model.

CAM6 is closer to observed tendencies during CSET than during SOCRATES. CAM6 N_d is slightly more correlated with observations (R=0.36, Figure SI 3- 6) and is less biased (30 to observed 42 cm^{-3}, Figure 3-12e). As in the SO, CAM6 captures the average observed CSET aerosol concentrations (43 to 34 cm^{-3}, Figure 3-12a) although it produces a much narrower range of likely concentrations compared to observations. CAM6 captures the majority of the observed CSET N_d-UHSAS relationship (Figure 3-12c), except for cases with low N_d. The narrower aerosol concentration range may be reducing the correlation of CAM6 relative to the observations (0.54 to 0.71) but the model still performs better than in SOCRATES. While CAM6 produces precipitation-depleted cloud features ($N_d \leq 10$ cm^{-3}), it does not produce these features concurrently with ultra-clean aerosol (UHSAS100 ≤ 10 cm^{-3}).

The better agreement between modeled and observed N_d for CSET compared to SOCRATES suggests that the mechanisms responsible for producing N_d in the SO are likely incomplete in CAM6 and unique to that pristine environment. N_d is developed through a balance of sources and sinks and leads to high and persistent values in the SO [*McCoy et al.*, 2020]. The interplay of the mechanisms producing and depleting CCN and thus N_d is complex. The too frequent occurrence of precipitation-depleted N_d in CSET and SOCRATES CAM6 simulations may indicate that precipitation removal processes are too active in the model, as has been seen in other GCMs [*Stephens et al.*, 2010]. This hypothesis is examined for SOCRATES in *Zhou et al.* [2020 submitted] but no consistent tendency in CAM6 precipitation is found connected to low-N_d bias across the campaign. Phase partitioning, particularly production of super-cooled clouds,

generally agrees with SOCRATES observations so may not play a large role in the low N_d bias [*Gettelman et al.*, 2020 submitted; *Zhou et al.*, 2020 submitted]. Activation of CCN into cloud droplets is dependent both on CCN availability and turbulent updrafts. However, there is no consistent turbulent updraft bias in CAM6 across the SOCRATES campaign: CAM6 tends to under-produce turbulence in stable and neutral boundary layers but match turbulence in unstable regimes [*Atlas et al.*, 2020 submitted]. There are noticeable cloud-regime dependent differences in CAM6 precipitation bias as well, with over-production in cumulus-like clouds and under-production in stratocumulus clouds [*Zhou et al.*, 2020 submitted]. Tendencies in precipitation and turbulent updrafts may have competing, regime dependent influences on N_d in CAM6, obscuring the overall impact these biases have on the CAM6 SOCRATES N_d bias.

The largest remaining and uninvestigated contributor to this N_d bias is CCN and its production in CAM6. We have already observed that the number concentrations of CCN are roughly consistent with the observed bin matched aerosol in CSET and SOCRATES (Figure 3-12a, b). CAM6's simulation of cloud-aerosol interactions in the less biologically active sub-tropics is also more promising as it better resembles the observed relationship and is considerably less biased than in the SO. One possible reason for this is that under-production of biological aerosol, particularly the Aitken aerosols that may be buffering the clouds against precipitation removal, is resulting in an under production of N_d in the SO. In the remainder of this section, we will use our expanded knowledge of the mechanisms impacting aerosol production in the SO to illuminate any discrepancies in modeled aerosol characteristics that may be influencing N_d.

As a first assessment of CAM6's skill in producing aerosol, we compare the observed and simulated number concentrations observed in the subtropics and SO. Extracting total aerosol and CCN (0.6% super-saturation) number concentrations along the flight paths for CSET and

SOCRATES, we formulate companion CAM6 altitude pdfs to those in Figure 3-3 (Figure 3-13). CAM6 during CSET reproduces the observed aerosol number concentrations for both CN and UHSAS100 with some accuracy, only underestimating the free tropospheric values (Figure 3-13a, b). CAM6 during SOCRATES reproduces observed aerosol number concentrations in the sub-cloud and above-cloud sampling but only for UHSAS100 (Figure 3-13a, c, e). The SOCRATES CN simulations for all the altitude pdfs, especially SC and AC, have a severe low-bias compared to observations (Figure 3-13b, d, and f). The flight matched CAM6 aerosol concentration pdfs for CSET and SOCRATES are strikingly similar despite the large differences in the observational pdfs for these two campaigns. This along with the larger discrepancy with observed CN during SOCRATES suggests that CAM6 may be missing mechanisms specific to the more biologically active summertime SO that are key in generating Aitken aerosols.

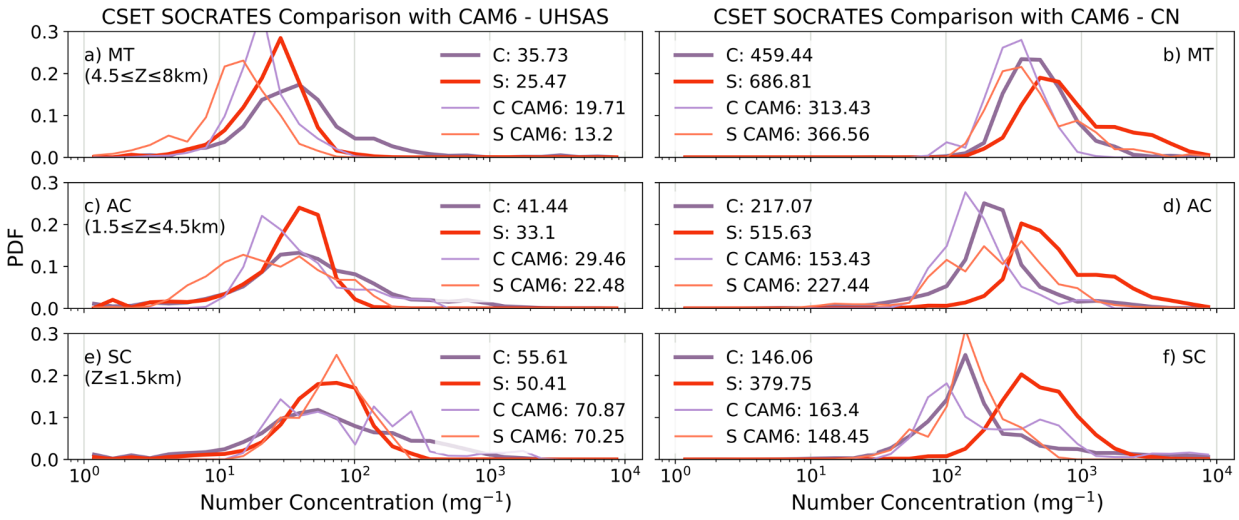

Figure 3-13 *As in Figure 3-3 but including CAM6 aerosol concentrations extracted along the flight tracks.*

While the modeled accumulation number concentrations are consistent with observations during both CSET and SOCRATES, it is possible that this is due more to an imbalance in sea-spray production rather than an accurate depiction of all aerosol in these environments. Recent

analysis of the HadGEM3 model found an overly active sea spray-wind speed mechanism which produced too much CCN [*Revell et al.*, 2019]. An examination of aerosol composition and the relationship between wind speed and number concentration suggests a similar problem may exist with CAM6. The MAM4 aerosol scheme produces four modes of aerosol: accumulation, Aitken, coarse, and insoluble coarse. Aerosol size is the same for all aerosols in each mode and mixing ratios are used to denote composition. To understand the relative contribution of aerosol type, we examine the magnitudes of the aerosol constituent mixing ratios for each mode. Representative mean vertical profiles of number concentration and composition mixing ratio are calculated for each mode and each flight along with a campaign average profile for SOCRATES and CSET (Figure SI 3- 7, Figure SI 3- 8). Sub-cloud ($Z \leq 1500$ m) coarse and accumulation mode aerosol mixing ratios are dominated by sea salt in the SO (Figure SI 3- 7a). Sulfate (SO_4) is the secondary contributor to accumulation mode and dominates Aitken mode in the SO (Figure SI 3- 7a, b). However, the sub-tropics see an equal contribution in accumulation mode between sea salt and sulfate (Figure SI 3- 8a). Coarse mode is still driven by sea salt and Aitken by SO_4 in CSET (Figure SI 3- 8b, c).

We would expect that if sea-spray is overproduced in CAM6 then it would dominate in an environment with higher wind speeds, such as the SO (e.g. Figure SI 3- 7a). However, observationally we have evidence that the sub-cloud and in-cloud aerosols are not dominated by sea-spray (3.3.1.3). We can additionally test the nature of aerosol production in CAM6 by comparing, as we did in 3.3.2.2, the log of the number concentration with the wind speed. In an approximate analog of the cumulative correlation coefficients in Figure 3-10, we correlate $\log_{10}$ number concentration and wind speed near the surface ($Z \leq 500$ m) for total number ($R=0.01$, not significant at 95%), accumulation and coarse ($R=0.16$, significant), and coarse mode ($R= 0.42$,

significant) aerosols. In contrast to the SOCRATES observations where only coarse mode aerosol was significantly correlated with wind speed, both coarse and accumulation mode number concentrations are significantly correlated with wind speed in CAM6.

Ultimately, aerosol enabled GCMs need to be able to capture the differences in N_d between the sub-tropics and the biologically active SO in order to accurately simulate the radiative impacts of clouds in these regions. Producing an observationally consistent number concentration for CCN but from an incorrect aerosol production pathway may lead to a masking of other biases that subsequently influence N_d. In particular, over-producing sea salt and under-producing sulfate in the SO could explain why there are larger discrepancies observed in SOCRATES N_d than in the less biologically active sub-tropics (Figure 3-9). We have also shown that CAM6 has difficulty in producing enough Aitken particles (Figure 3-13b, d, and f). Because this is a biologically dominated mode (Figure SI 3- 7), it is likely that this under-production is linked to insufficient DMS production, distribution, or oxidation into viable pre-cursor gases for particle formation. A simple comparison between the roughly equal January and February mid-tropospheric sampling during SOCRATES indicates that while observational pdfs of CN are consistent between the two months, CAM6 Aitken mode is hugely different (Figure SI 3- 9). This is likely linked to the discrete DMS climatology used in CAM6 which decreases sharply from January to February [*Lana et al.*, 2011]. Note that even though January is closer to the observed pdf, CAM6 still under-produces the high CN concentrations that we link to RPF. While there are some immediate fixes that can be used to improve simulated biological activity and sources important for aerosol production (e.g. developing a higher time resolution climatology or an interactive DMS production model), the mechanisms controlling how and where aerosol is produced and grown to CCN are likely incomplete or missing in CAM6. This paper illustrates some of the complexities of these

production and growth mechanisms and underlines the importance of understanding and capturing these mechanisms in GCMs in order to advance the simulation of SO cloud-aerosol interactions and thereby reduce SO radiative biases.

3.4 Conclusions and Discussion

We present evidence of widespread and frequent recent particle formation (RPF) in the summertime Southern Ocean free troposphere. Signatures of free tropospheric RPF observed during *in situ* airborne sampling from the SOCRATES field campaign included: high concentrations of total aerosol number concentrations (CN> 1000 mg^{-1}) typically accompanied by large and rapid spatial CN variability, low accumulation and coarse mode aerosol surface area (<10 μm^2 mg^{-1}), and small accumulation-mode aerosol concentrations (UHSAS100 < 80 mg^{-1}). These primarily Aitken mode particles volatilized when heated to ~60°C, suggesting they are composed from sulfuric acid or an even more volatile DMS-oxidation product. Back-trajectory analysis of SOCRATES sampled air masses revealed RPF classified events (CN ≥ 2500 mg^{-1}) recently underwent ascent from below 1 km to free-tropospheric altitudes. Ascent was driven by diverse synoptic mechanisms across the campaign but primarily was associated with uplift through warm-conveyor belts or sub-polar vortices.

Our results provide evidence supporting a hypothesized particle production mechanism: boundary-layer air parcels rich in marine biogenic gases (i.e. DMS) are swept up into stratiform clouds, precipitation scavenges large aerosols from the air parcel and reduces aerosol surface area, DMS oxidizes into precursor gases (e.g. SO_2, H_2SO_4, and MSA) upon the air parcel exiting the cloud, and gas to particle conversion is enabled in the free troposphere. This newly identified synoptic mechanism is a variant on other cloud-outflow associated particle formation [*Kerminen et al.*, 2018]. Specifically, in the SO, this mechanism acts in addition to the particle formation

generated in outflow from overshooting cumulus congestus clouds [*Clarke et al.*, 1998]. Synoptic scale ascent over the SO is deeper and more widespread than cumulus outflow and helps explain the high Aitken mode concentrations observed frequently throughout the SO summertime free troposphere. Both mechanisms assume outgassing of DMS from a biologically active ocean and are expected to operate much more frequently in summer than in winter.

Aitken-mode aerosol concentrations are nearly as high in the SO boundary layer as in the free troposphere. They are substantially higher than those typically measured in and above cloudy boundary layers over remote parts of the marine subtropics. We find a negligible relationship between sub-cloud wind speed and aerosol concentrations for both Aitken and accumulation mode sizes, suggesting that sea spray aerosol does not control CCN number over the summertime SO. Sea-spray is likely more important for large aerosols, as exhibited by stronger correlations between wind speed and large accumulation and coarse mode sizes. STEM analysis [*Twohy et al.*, 2020 submitted] shows above, in, and sub-cloud particle (0.1-0.5 μm) compositions are dominantly sulfur-based. We conclude that sea-spray particles are of secondary importance to sulfur-based particles in controlling the CCN budget and influencing summertime SO cloud droplet number concentrations.

The missing source of sub-cloud, sulfur-based particles maintaining CCN in the SO may be the reservoir of free tropospheric Aitken mode aerosol. Previous work has demonstrated descent of free tropospheric Aitken particles into the boundary layer is possible [*Covert et al.*, 1996; *Humphries et al.*, 2016] and that this is an important CCN source in the NEA [*Sanchez et al.*, 2018; *Zheng et al.*, 2018]. A global chemical transport model showed entrainment of free tropospheric H_2SO_4 particles into the MBL may be the dominant mechanism for DMS influence on CCN and that these FT Aitken particles are the dominant contributor to CCN in the SH summertime oceans

[*Korhonen et al.*, 2008]. Droplet number concentrations are consistently high in the SO and the occurrence of precipitation depleted cloud features are infrequent. This leads us to hypothesize that the summertime SO is a buffered system in which there are copious small aerosol particles that are inefficiently scavenged by precipitation but can nucleate into droplets under suitable conditions, sustaining the droplet concentration of SO clouds against precipitation removal processes. Evidence supporting our hypothesized buffering mechanism is presented along with a contrasting sub-tropical analysis to understand the significance of SO cloud-aerosol behavior.

Our hypothesized aerosol lifecycle would involve large spatial scales as it requires lofting of DMS, production of Aitken mode aerosols in the free troposphere from DMS-oxidation products, Aitken particle descent into the boundary layer, and Aitken particle growth into accumulation mode sizes below cloud. This is consistent with stronger correlations found between DMS fluxes and droplet number concentration over large spatial scales [*Andreae et al.*, 1995; *Covert et al.*, 1996; *McCoy et al.*, 2015] and limited local correlations [*Covert et al.*, 1996].

In this study, we utilize the buffering mechanism as a framework for interpreting cloud-aerosol interactions in nudged simulations from CAM6. Despite capturing cloud-aerosol interactions in the sub-tropics, we find a persistent low-bias in SO N_d relative to SOCRATES observations. This regional discrepancy and our preliminary aerosol composition investigations suggest that i) biological aerosol is under-produced in CAM6 and ii) that it is likely there is a compensating bias of sea-spray over-production as has been seen in other GCMs [*Revell et al.*, 2019]. Despite capturing the magnitude of SO CCN number, the composition of these aerosols is significantly different from the biologically dominated aerosols observed during SOCRATES. CAM6 exhibits systematically low numbers of CN that, in better keeping with observations, are primarily sulfur-based. These two inconsistencies suggest that the low CAM6 N_d exhibited across

the campaign may be connected with an underproduction of biological aerosol. To completely understand how a CN and composition bias in CCN is driving the low bias in N_d, however, the regime dependent biases in precipitation [*Zhou et al.*, 2020 submitted] and turbulence (e.g. aerosol activation) [*Atlas et al.*, 2020 submitted] should be examined in concert. Once the CCN production is corrected, the relative influence of precipitation and activation on N_d as well as the potential role of buffering by Aitken aerosols will become clearer. While the exact role is unclear, our results strongly suggest that CAM6 may have incomplete or missing radiatively-important aerosol production and growth mechanisms associated with biological aerosol, something other state of the art GCMs suffer from in the Southern Ocean [*Bodas-Salcedo et al.*, 2019; *Revell et al.*, 2019; *McCoy et al.*, 2020]. Both mechanisms introduced in this text (i.e. particle production through synoptic-uplift and aerosol buffering against precipitation depletion) are potential candidates for improving CAM6 representation of biologically driven aerosol-cloud interactions. Neglecting natural new particle formation in GCMs will lead to an underestimation of the strength of the radiative forcing associated with aerosol-cloud interactions [*Gordon et al.*, 2017], further supporting the importance of understanding and capturing these mechanisms.

The proposed buffering mechanism and its influence on SO and other pristine environments needs more in-depth investigation. LES simulations and additional observations of the SO aerosol-cloud system will be important in assessing mechanism robustness. One important aspect that has not been addressed here but could be examined though LES simulations of the SO environment is the time scale over which these processes occur. The feasibility of free tropospheric Aitken particles buffering the CCN budget will be determined by the balance between the rate of SO N_d depletion by precipitation compared to the rate of Aitken mode particle growth to cloud affecting sizes. Examining the role of mixed-phase and super-cooled cloud physics on aerosol

cloud interactions in the SO should be considered as well for a complete understanding of this mechanism and its generalizability to other pristine environments. The influence of the buffering mechanism may differ across regions, a key consideration in understanding how pristine clouds respond to anthropogenic aerosol [*Carslaw et al.*, 2013] and in constraining radiative forcing associated with cloud-aerosol interactions [*Bellouin*, 2019].

Additional observations from the Southern Ocean can help us understand the influence of the synoptic particle production mechanism and the validity of the buffering hypothesis. We know that small particles may be playing an important role in the SO, thus it is critical to sample a size distribution that includes the Aitken and nucleation mode ranges and understand its evolution with altitude, geography, and near clouds. Aerosol composition and trace gas species measured concurrently with this size distribution will reveal the origins of the aerosols important to the CCN budget. Knowledge of the particle composition as well as the availability of DMS and pre-cursor gases in the Southern Ocean at the surface and aloft would enable rate calculations and estimates of processing time for aerosol formation, growth, and depletion. Such estimates would help determine how phytoplankton and their DMS emissions exert long-range influence on clouds and aerosols in the Southern Ocean. New particle production is expected to be seasonal due to its biological dependence. Repeating the same statistical sampling methodology from SOCRATES in a shoulder season (i.e. austral spring or fall) will help us to understand the degree of fluctuation in the aerosol budget with biological activity and the subsequent influence on N_d. Seasonal examinations of cloud and aerosol characteristics as well as characterization of pristine aerosol sources and sinks will further help to correct current GCM discrepancies [*Bodas-Salcedo et al.*, 2019; *McCoy et al.*, 2020].

Before beginning a separate investigation of the Southern Ocean, however, we suggest that pre-existing datasets from flight, ship, satellite, and ground stations should be leveraged to their fullest extent to determine the ubiquity of the buffering mechanism and the role that it plays in modulating cloud-aerosol interactions across the globe. Measurements of other pristine regions of the world can help us to understand the uniqueness of the SO as well as the role of the buffering mechanism in controlling cloud susceptibility in diverse environments. Determining the degree of susceptibility in pristine environments will have important implications for the pre-industrial state and constraining the radiative effect of aerosol-cloud interactions under industrialization.

Chapter 4. CONCLUSIONS

In Chapter 2, I present results from an observational method developed to constrain global climate model (GCM) estimations of the change in droplet number concentration (N_d) from pre-industrial and the radiative forcing associated with aerosol cloud interactions. The constraint is developed from the hemispheric contrast between oceanic N_d in the polluted Northern Hemisphere (NH) and the pristine Southern Hemisphere (SH), $\Delta N_{d(NH-SH)}$. This hemispheric difference is correlated with the change from pre-industrial N_d, $\Delta N_{d(PD-PI)}$, estimated from a variety of GCMs: models participating in the Aerocom phase II indirect experiment [*Ghan et al.*, 2016], sensitivity experiments conducted in the development of HadGEM3-GA7.1 [*Mulcahy et al.*, 2018], and a perturbed parameter ensemble (PPE) within HadGEM3-GA4-UKCA [*Yoshioka et al.*, 2019]. Based on MODIS satellite derived $\Delta N_{d(NH-SH)}$ and output from GCMs, $\Delta N_{d(PD-PI)}$ is constrained to be between 8 and 24 cm^{-3}. RF_{aci} is constrained to be between -1.2 and -0.6 Wm^{-2}. This constraint on RF_{aci} agrees with the most probable range of -1.2 to -0.3 Wm^{-2} developed in *Bellouin* [2019] from different observational constraints (i.e. studies relating aerosol variance to N_d variance).

Models examined in Chapter 2 generally simulate larger hemispheric N_d differences than are calculated from satellite retrievals. Satellite derived $\Delta N_{d(NH-SH)}$ is relatively low partly due to high local summertime N_d over the SH midlatitudes, which is observationally supported from multiple datasets. The pattern and magnitude of summertime N_d in SH oceans is developed through a complex balance of dominantly biological aerosol sources and low removal rates from precipitation scavenging on the poleward flank of the mid-latitude storm track. This is demonstrated using a simple budget model for cloud condensation nuclei (CCN) and rain rates estimated from CloudSat retrievals. None of the GCMs surveyed here or the 235 original PPE ensemble members come near to reproducing the high near-Antarctic values in summertime,

suggesting models are missing key processes and/or emission sources important for CCN near Antarctica and potentially across the SH. Understanding these pristine aerosol cloud interaction mechanisms will be essential for accurately estimating our climates response to industrialization. This work is summarized in *McCoy et al.* [2020].

In Chapter 3, I delve into a more detailed examination of pristine aerosol cloud interactions and aerosol sources in the summertime Southern Ocean. I use two sets of aircraft observations in this examination: the 2018 summertime Southern Ocean Clouds, Radiation, Aerosol Transport Experimental Study (SOCRATES) [*McFarquhar et al.*, 2020 submitted] and, as a sub-tropical contrast, the 2015 summertime Cloud Systems Evolution in the Trades (CSET) [*Albrecht et al.*, 2019]. I present evidence of widespread, frequent recent particle formation (RPF) in the summertime SO which dominates free tropospheric aerosol. Back-trajectory analysis of SOCRATES sampled air masses and volatility composition calculations revealed RPF classified events likely follow a novel synoptic uplift mechanism for particle generation: Boundary-layer air parcels rich in marine biogenic gases (i.e. DMS) are swept up through clouds associated with synoptic uplift, precipitation scavenges large aerosols from the air parcel and reduces aerosol surface area, DMS oxidizes into precursor gases (e.g. SO_2, H_2SO_4, and MSA) upon the air parcel exiting the cloud, and gas to particle conversion is enabled in the free troposphere. Ascent of these parcels was driven by diverse synoptic mechanisms across the campaign but primarily was associated with uplift through warm-conveyor belts or sub-polar vortices. This mechanism acts in addition to the particle formation generated in outflow from overshooting cumulus congestus clouds [*Clarke et al.*, 1998] but is both deeper and more widespread, better explaining the high Aitken mode concentrations observed frequently throughout the SO summertime free troposphere.

Sea-spray particles are of secondary importance to sulfur-based particles in controlling the CCN budget and influencing summertime SO cloud droplet number concentrations. This is shown by the negligible relationship between sub-cloud wind speed and aerosol concentrations for both Aitken and accumulation mode sizes and the dominance of sulfur-based accumulation mode aerosol (100-500 nm) sub, in, and above cloud [*Twohy et al.*, 2020 submitted]. The missing source of sub-cloud, sulfur-based particles maintaining CCN in the SO is likely the reservoir of free tropospheric Aitken mode aerosol. Descent of free tropospheric Aitken particles into the boundary layer is possible [*Covert et al.*, 1996; *Humphries et al.*, 2016] and similar descent is an important CCN source in the North East Atlantic [*Sanchez et al.*, 2018; *Zheng et al.*, 2018]. My observational results further support the important *Korhonen et al.* [2008] modeling study that found entrainment of free tropospheric sulfuric acid particles into the boundary layer was both the dominant mechanism for DMS influence on CCN and the dominant contributor to CCN in the SH summertime oceans. I further hypothesize, based on the persistently high SO summertime Nd and lack of precipitation-depleted cloud features, that the summertime SO is a buffered system. That is, copious Aitken mode aerosol particles from the free troposphere and sub-cloud are inefficiently scavenged by precipitation but help to nucleate into droplets under suitable conditions, sustaining the high SO N_d clouds against precipitation removal processes.

The buffering mechanism is further used as a framework for interpreting cloud-aerosol interactions in nudged simulations from CAM6. Despite capturing cloud-aerosol interactions in the sub-tropics, we find a persistent low-bias in SO N_d relative to SOCRATES observations. This regional discrepancy and our preliminary aerosol composition investigations suggest that i) biological aerosol is under-produced in CAM6 and ii) that it is likely there is a compensating bias of sea-spray over-production as has been seen in other GCMs [*Revell et al.*, 2019]. Further, CAM6

may have incomplete or missing radiatively-important aerosol production and growth mechanisms associated with biological aerosol, something other state of the art GCMs suffer from in the Southern Ocean [*Bodas-Salcedo et al.*, 2019; *Revell et al.*, 2019; *McCoy et al.*, 2020]. Both mechanisms introduced in Chapter 3 (i.e. particle production through synoptic-uplift and aerosol buffering against precipitation depletion) are potential candidates for improving CAM6 representation of biologically driven aerosol-cloud interactions. Neglecting natural new particle formation in GCMs will lead to an underestimation of the strength of the radiative forcing associated with aerosol-cloud interactions [*Gordon et al.*, 2017], further supporting the importance of understanding and capturing these mechanisms as was motivated in Chapter 2. The work in Chapter 3 is summarized in *McCoy and Toohey* [2020 submitted].

BIBLIOGRAPHY

Ahn, E., Huang, Y., Siems, S. T., and Manton, M. J. (2018), A Comparison of Cloud Microphysical Properties Derived From MODIS and CALIPSO With In Situ Measurements Over the Wintertime Southern Ocean, *Journal of Geophysical Research: Atmospheres*, *123*(19), 11,120-111,140, doi:10.1029/2018jd028535.

Albrecht, B. A. (1989), Aerosols, cloud microphysics, and fractional cloudiness, *Science*, *245*(4923), 1227-1230, doi:10.1126/science.245.4923.1227.

Albrecht, B. A., et al. (2019), Cloud System Evolution in the Trades (CSET): Following the Evolution of Boundary Layer Cloud Systems with the NSF–NCAR GV, *Bulletin of the American Meteorological Society*, *100*(1), 93-121, doi:10.1175/bams-d-17-0180.1.

Andreae, M. O., Elbert, W., and Demora, S. J. (1995), Biogenic Sulfur Emissions and Aerosols over the Tropical South-Atlantic .3. Atmospheric Dimethylsulfide, Aerosols and Cloud Condensation Nuclei, *Journal of Geophysical Research-Atmospheres*, *100*(D6), 11335-11356, doi:Doi 10.1029/94jd02828.

Andreae, M. O., Jones, C. D., and Cox, P. M. (2005), Strong present-day aerosol cooling implies a hot future, *Nature*, *435*(7046), 1187-1190, doi:10.1038/nature03671.

Andrews, T. (2014), Using an AGCM to Diagnose Historical Effective Radiative Forcing and Mechanisms of Recent Decadal Climate Change, *Journal of Climate*, *27*(3), 1193-1209, doi:10.1175/jcli-d-13-00336.1.

Atlas, R. L., Bretherton, C. S., Blossey, P. N., Gettelman, A., Bardeen, C., Lin, P., and Ming, Y. (2020 submitted), How well do large-eddy simulations and global climate models represent observed boundary layer structures and low clouds over the summertime Southern Ocean?, *J. Adv. Model. Earth Syst.*

Ayers, G. P., Cainey, J. M., Gillett, R. W., and Ivey, J. P. (1997), Atmospheric sulphur and cloud condensation nuclei in marine air in the Southern Hemisphere, *Philosophical Transactions of the Royal Society of London Series B-Biological Sciences*, *352*(1350), 203-211.

Ayers, G. P., and Gillett, R. W. (2000), DMS and its oxidation products in the remote marine atmosphere: implications for climate and atmospheric chemistry, *Journal of Sea Research*, *43*(3), 275-286, doi:https://doi.org/10.1016/S1385-1101(00)00022-8.

Ayers, G. P., and Gras, J. L. (1991), Seasonal relationship between cloud condensation nuclei and aerosol methanesulphonate in marine air, *Nature*, *353*(6347), 834-835, doi:10.1038/353834a0.

Bellouin, N., Quaas, J., Gryspeerdt, E., Kinne, S., Stier, P., Watson-Parris, D., Boucher, O., Carslaw, K. S., Christensen, M., Daniau, A.-L., Dufresne, J.-L., Feingold, G., Fiedler, S., Forster, P., Gettelman, A., Haywood, J.M., Lohmann, U., Malavelle, F., Mauritsen, T., McCoy, D.T., Myhre, G., Muelmenstaedt, J., Neubauer, D., Possner, A., Rugenstein, M., Sato, Y., Schulz, M.,

Schwartz, S.E., Sourdeval, O., Storelvmo, T., Toll, V., Winker, D. and Stevens, B. (2019), Bounding global aerosol radiative forcing of climate change, *Reviews of Geophysics*.

Bender, F.-M., Frey, L., McCoy, D. T., Grosvenor, D. P., and Mohrmann, J. K. (2019), Assessment of aerosol–cloud–radiation correlations in satellite observations, climate models and reanalysis, *Climate Dynamics*, *52*(7-8), 4371-4392.

Bennartz, R., and Rausch, J. (2017), Global and regional estimates of warm cloud droplet number concentration based on 13 years of AQUA-MODIS observations, *Atmos. Chem. Phys.*, *17*(16), 9815-9836, doi:10.5194/acp-17-9815-2017.

Berresheim, H. (2002), Gas-aerosol relationships of H2SO4, MSA, and OH: Observations in the coastal marine boundary layer at Mace Head, Ireland, *Journal of Geophysical Research*, *107*(D19), doi:10.1029/2000jd000229.

Bigg, E. K. (2007), Sources, nature and influence on climate of marine airborne particles, *Environmental Chemistry*, *4*(3), 155-161, doi:10.1071/en07001.

Bigg, E. K., and Leck, C. (2008), The composition of fragments of bubbles bursting at the ocean surface, *Journal of Geophysical Research-Atmospheres*, *113*(D11), doi:10.1029/2007jd009078.

Bodas-Salcedo, A., Hill, P. G., Furtado, K., Williams, K. D., Field, P. R., Manners, J. C., and Hyder, P. (2016), Large Contribution of Supercooled Liquid Clouds to the Solar Radiation Budget of the Southern Ocean, *Journal of Climate*, *29*(11), 4213-4228, doi:10.1175/jcli-d-15-0564.1.

Bodas-Salcedo, A., Williams, K. D., Field, P. R., and Lock, A. P. (2012), The Surface Downwelling Solar Radiation Surplus over the Southern Ocean in the Met Office Model: The Role of Midlatitude Cyclone Clouds, *Journal of Climate*, *25*(21), 7467-7486, doi:10.1175/jcli-d-11-00702.1.

Bodas-Salcedo, A., Williams, K. D., Ringer, M. A., Beau, I., Cole, J. N. S., Dufresne, J. L., Koshiro, T., Stevens, B., Wang, Z., and Yokohata, T. (2014), Origins of the Solar Radiation Biases over the Southern Ocean in CFMIP2 Models, *Journal of Climate*, *27*(1), 41-56, doi:10.1175/jcli-d-13-00169.1.

Bodas-Salcedo, A., Mulcahy, J. P., Andrews, T., Williams, K. D., Ringer, M. A., Field, P. R., and Elsaesser, G. S. (2019), Strong dependence of atmospheric feedbacks on mixed-phase microphysics and aerosol-cloud interactions in HadGEM3, *J. Adv. Model. Earth Syst.*, *11*(6), 1735-1758, doi:10.1029/2019ms001688.

Boers, R., Jensen, J. B., and Krummel, P. B. (1998), Microphysical and short-wave radiative structure of stratocumulus clouds over the Southern Ocean: Summer results and seasonal differences, *Quarterly Journal of the Royal Meteorological Society*, *124*(545), 151-168, doi:10.1002/qj.49712454507.

Boucher, O., D. Randall, P. Artaxo, C. Bretherton, G. Feingold, P. Forster, V.-M. Kerminen, Y. Kondo, H. Liao, U. Lohmann, P. Rasch, S.K. Satheesh, S. Sherwood, B. Stevens and X.Y.

Zhang, (2013), Clouds and Aerosols*Rep.*, Cambridge University Press, Cambridge, United Kingdom and New York, NY, USA.

Boucher, O., and Lohmann, U. (1995), The sulfate-CCN-cloud albedo effect, *Tellus B*, *47*(3), 281-300, doi:10.1034/j.1600-0889.47.issue3.1.x.

Bretherton, C. S., McCoy, I. L., Mohrmann, J., Wood, R., Ghate, V., Gettelman, A., Bardeen, C. G., Albrecht, B. A., and Zuidema, P. (2019), Cloud, Aerosol, and Boundary Layer Structure across the Northeast Pacific Stratocumulus-Cumulus Transition as Observed during CSET, *Monthly Weather Review*, *147*(6), 2083-2103, doi:10.1175/Mwr-D-18-0281.1.

Burrows, S. M., Ogunro, O., Frossard, A. A., Russell, L. M., Rasch, P. J., and Elliott, S. M. (2014), A physically based framework for modeling the organic fractionation of sea spray aerosol from bubble film Langmuir equilibria, *Atmos. Chem. Phys.*, *14*(24), 13601-13629, doi:10.5194/acp-14-13601-2014.

Carslaw, K. S., Gordon, H., Hamilton, D. S., Johnson, J. S., Regayre, L. A., Yoshioka, M., and Pringle, K. J. (2017), Aerosols in the Pre-industrial Atmosphere, *Current Climate Change Reports*, *3*(1), 1-15, doi:10.1007/s40641-017-0061-2.

Carslaw, K. S., L. A. Lee, L. A. Regayre, J. S. Johnson (2018), Climate models are uncertain, but we can do something about it, in *Eos*, edited, doi:https://doi.org/10.1029/2018EO093757.

Carslaw, K. S., et al. (2013), Large contribution of natural aerosols to uncertainty in indirect forcing, *Nature*, *503*(7474), 67-+, doi:10.1038/nature12674.

Catto, J. L., Madonna, E., Joos, H., Rudeva, I., and Simmonds, I. (2015), Global Relationship between Fronts and Warm Conveyor Belts and the Impact on Extreme Precipitation, *Journal of Climate*, *28*(21), 8411-8429, doi:10.1175/Jcli-D-15-0171.1.

Chan, K. M., and Wood, R. (2013), The seasonal cycle of planetary boundary layer depth determined using COSMIC radio occultation data, *Journal of Geophysical Research: Atmospheres*, *118*(22), 12,422-412,434.

Chand, D., Wood, R., Ghan, S. J., Wang, M., Ovchinnikov, M., Rasch, P. J., Miller, S., Schichtel, B., and Moore, T. (2012), Aerosol optical depth increase in partly cloudy conditions, *Journal of Geophysical Research: Atmospheres*, *117*(D17), n/a-n/a, doi:10.1029/2012jd017894.

Charlson, R. J., Lovelock, J. E., Andreae, M. O., and Warren, S. G. (1987), Oceanic Phytoplankton, Atmospheric Sulfur, Cloud Albedo and Climate, *Nature*, *326*(6114), 655-661, doi:DOI 10.1038/326655a0.

Clarke, A. D. (1991), A thermo-optic technique for in situ analysis of size-resolved aerosol physicochemistry, *Atmospheric Environment. Part A. General Topics*, *25*(3), 635-644, doi:https://doi.org/10.1016/0960-1686(91)90061-B.

Clarke, A. D. (1993), Atmospheric nuclei in the Pacific midtroposphere: Their nature, concentration, and evolution, *Journal of Geophysical Research: Atmospheres*, *98*(D11), 20633-20647, doi:10.1029/93jd00797.

Clarke, A. D., Varner, J. L., Eisele, F., Mauldin, R. L., Tanner, D., and Litchy, M. (1998), Particle production in the remote marine atmosphere: Cloud outflow and subsidence during ACE 1, *Journal of Geophysical Research-Atmospheres*, *103*(D13), 16397-16409, doi:10.1029/97jd02987.

Clement, C. F., Ford, I. J., Twohy, C. H., Weinheimer, A., and Campos, T. (2002), Particle production in the outflow of a midlatitude storm, *Journal of Geophysical Research: Atmospheres*, *107*(D21), AAC 5-1-AAC 5-9, doi:10.1029/2001jd001352.

Collins, M., Booth, B. B. B., Bhaskaran, B., Harris, G. R., Murphy, J. M., Sexton, D. M. H., and Webb, M. J. (2010), Climate model errors, feedbacks and forcings: a comparison of perturbed physics and multi-model ensembles, *Climate Dynamics*, *36*(9-10), 1737-1766, doi:10.1007/s00382-010-0808-0.

Covert, D. S., Kapustin, V. N., Bates, T. S., and Quinn, P. K. (1996), Physical properties of marine boundary layer aerosol particles of the mid-Pacific in relation to sources and meteorological transport, *101*(D3), 6919-6930, doi:doi:10.1029/95JD03068.

Dall Osto, M., et al. (2017), Arctic sea ice melt leads to atmospheric new particle formation, *Sci Rep*, *7*(1), 3318, doi:10.1038/s41598-017-03328-1.

Donlon, C. J., Martin, M., Stark, J., Roberts-Jones, J., Fiedler, E., and Wimmer, W. (2012), The Operational Sea Surface Temperature and Sea Ice Analysis (OSTIA) system, *Remote Sensing of Environment*, *116*, 140-158, doi:https://doi.org/10.1016/j.rse.2010.10.017.

Dunne, E. M., et al. (2016), Global atmospheric particle formation from CERN CLOUD measurements, *Science*, *354*(6316), 1119-1124, doi:10.1126/science.aaf2649.

Eckhardt, S., Stohl, A., Wernli, H., James, P., Forster, C., and Spichtinger, N. (2004), A 15-Year Climatology of Warm Conveyor Belts, *Journal of Climate*, *17*(1), 218-237, doi:10.1175/1520-0442(2004)017<0218:Aycowc>2.0.Co;2.

Feng, Y., and Ramanathan, V. (2010), Investigation of aerosol–cloud interactions using a chemical transport model constrained by satellite observations, *Tellus B: Chemical and Physical Meteorology*, *62*(1), 69-86, doi:10.1111/j.1600-0889.2009.00444.x.

Fitzgerald, J. W. (1991), Marine aerosols: A review, *Atmospheric Environment. Part A. General Topics*, *25*(3), 533-545, doi:https://doi.org/10.1016/0960-1686(91)90050-H.

Forster, P. M. (2016), Inference of Climate Sensitivity from Analysis of Earth's Energy Budget, *Annual Review of Earth and Planetary Sciences*, *44*(1), 85-106, doi:10.1146/annurev-earth-060614-105156.

Fossum, K. N., et al. (2018), Summertime Primary and Secondary Contributions to Southern Ocean Cloud Condensation Nuclei, *Sci Rep*, *8*(1), 13844, doi:10.1038/s41598-018-32047-4.

Gelaro, R., et al. (2017), The Modern-Era Retrospective Analysis for Research and Applications, Version 2 (MERRA-2), *Journal of Climate*, *30*(14), 5419-5454, doi:10.1175/jcli-d-16-0758.1.

Gettelman, A., Bardeen, C. G., McCluskey, C. S., J□arvinen, E., Stith, J., Bretherton, C., McFarquhar, G., Twohy, C., D'Alessandro, J., and Wu, W. (2020 submitted), Simulating Observations of Southern Ocean Clouds and Implications for Climate, *Journal of Geophysical Research: Atmospheres*.

Ghan, S., et al. (2016), Challenges in constraining anthropogenic aerosol effects on cloud radiative forcing using present-day spatiotemporal variability, *Proceedings of the National Academy of Sciences*, doi:10.1073/pnas.1514036113.

Gordon, H., et al. (2017), Causes and importance of new particle formation in the present-day and preindustrial atmospheres, *Journal of Geophysical Research: Atmospheres*, *122*(16), 8739-8760, doi:10.1002/2017jd026844.

Gordon, H., et al. (2016), Reduced anthropogenic aerosol radiative forcing caused by biogenic new particle formation, *Proceedings of the National Academy of Sciences*, *113*(43), 12053-12058, doi:10.1073/pnas.1602360113.

Granier, C., et al. (2011), Evolution of anthropogenic and biomass burning emissions of air pollutants at global and regional scales during the 1980–2010 period, *Climatic Change*, *109*(1-2), 163-190, doi:10.1007/s10584-011-0154-1.

Grosvenor, D. P., Sourdeval, O., and Wood, R. (2018a), Parameterizing cloud top effective radii from satellite retrieved values, accounting for vertical photon transport: quantification and correction of the resulting bias in droplet concentration and liquid water path retrievals, *Atmospheric Measurement Techniques*, *11*(7), 4273-4289, doi:10.5194/amt-11-4273-2018.

Grosvenor, D. P., et al. (2018b), Remote Sensing of Droplet Number Concentration in Warm Clouds: A Review of the Current State of Knowledge and Perspectives, *Rev Geophys*, *56*(2), 409-453, doi:10.1029/2017RG000593.

Grosvenor, D. P., and Wood, R. (2014), The effect of solar zenith angle on MODIS cloud optical and microphysical retrievals within marine liquid water clouds, *Atmospheric Chemistry and Physics*, *14*(14), 7291-7321, doi:10.5194/acp-14-7291-2014.

Grosvenor, D. P. W., R. (2018), Daily MODIS (MODerate Imaging Spectroradiometer) derived cloud droplet number concentration global dataset for 2003-2015, edited, Centre for Environmental Data Analysis.

Gryspeerdt, E., Goren, T., Sourdeval, O., Quaas, J., Mülmenstädt, J., Dipu, S., Unglaub, C., Gettelman, A., and Christensen, M. (2019), Constraining the aerosol influence on cloud liquid water path, *Atmospheric Chemistry & Physics*, *19*(8), 5331-5347, doi:10.5194/acp-19-5331-2019.

Gryspeerdt, E., Quaas, J., and Bellouin, N. (2016), Constraining the aerosol influence on cloud fraction, *Journal of Geophysical Research: Atmospheres*, n/a-n/a, doi:10.1002/2015JD023744.

Grythe, H., Ström, J., Krejci, R., Quinn, P., and Stohl, A. (2014), A review of sea-spray aerosol source functions using a large global set of sea salt aerosol concentration measurements, *Atmospheric Chemistry and Physics*, *14*(3), 1277-1297, doi:10.5194/acp-14-1277-2014.

Hakim, J. R. H. G. J. (2013), *An Introduction to Dynamic Meteorology*, Fifth ed., Elseveir, Academic Press, doi:https://doi.org/10.1016/C2009-0-63394-8.

Hamilton, D. S., Hantson, S., Scott, C., Kaplan, J., Pringle, K., Nieradzik, L., Rap, A., Folberth, G., Spracklen, D., and Carslaw, K. (2018), Reassessment of pre-industrial fire emissions strongly affects anthropogenic aerosol forcing, *Nature communications*, *9*(1), 3182.

Hamilton, D. S., Lee, L. A., Pringle, K. J., Reddington, C. L., Spracklen, D. V., and Carslaw, K. S. (2014), Occurrence of pristine aerosol environments on a polluted planet, *Proceedings of the National Academy of Sciences of the United States of America*, *111*(52), 18466-18471, doi:10.1073/pnas.1415440111.

Han, Q., Rossow, W. B., and Lacis, A. A. (1994), Near-Global Survey of Effective Droplet Radii in Liquid Water Clouds Using ISCCP Data, *7*(4), 465-497, doi:10.1175/1520-0442(1994)007<0465:Ngsoed>2.0.Co;2.

Haynes, J. M., L'Ecuyer, T. S., Stephens, G. L., Miller, S. D., Mitrescu, C., Wood, N. B., and Tanelli, S. (2009), Rainfall retrieval over the ocean with spaceborne W-band radar, *Journal of Geophysical Research: Atmospheres*, *114*(D8).

Herenz, P., Wex, H., Mangold, A., Laffineur, Q., Gorodetskaya, I. V., Fleming, Z. L., Panagi, M., and Stratmann, F. (2019), CCN measurements at the Princess Elisabeth Antarctica research station during three austral summers, *Atmospheric Chemistry and Physics*, *19*(1), 275-294, doi:10.5194/acp-19-275-2019.

Hobbs, P. V. (1971), Simultaneous Airborne Measurements of Cloud Condensation Nuclei and Sodium-Containing Particles over Ocean, *Quarterly Journal of the Royal Meteorological Society*, *97*(413), 263-&, doi:DOI 10.1256/smsqj.41301.

Hoskins, B. J., and Hodges, K. I. (2005), A New Perspective on Southern Hemisphere Storm Tracks, *Journal of Climate*, *18*(20), 4108-4129, doi:10.1175/jcli3570.1.

Humphries, R. S., Klekociuk, A. R., Schofield, R., Keywood, M., Ward, J., and Wilson, S. R. (2016), Unexpectedly high ultrafine aerosol concentrations above East Antarctic sea ice, *Atmospheric Chemistry and Physics*, *16*(4), 2185-2206, doi:10.5194/acp-16-2185-2016.

Jang, E., Park, K.-T., Yoon, Y. J., Kim, T.-W., Hong, S.-B., Becagli, S., Traversi, R., Kim, J., and Gim, Y. (2019), New particle formation events observed at the King Sejong Station, Antarctic Peninsula – Part 2: Link with the oceanic biological activities, *Atmospheric Chemistry and Physics*, *19*(11), 7595-7608, doi:10.5194/acp-19-7595-2019.

Johnson, J. S., Regayre, L. A., Yoshioka, M., Pringle, K. J., Lee, L. A., Sexton, D. M. H., Rostron, J. W., Booth, B. B. B., and Carslaw, K. S. (2018), The importance of comprehensive parameter sampling and multiple observations for robust constraint of aerosol radiative forcing, *Atmospheric Chemistry and Physics*, *18*(17), 13031-13053, doi:10.5194/acp-18-13031-2018.

Johnson, J. S., et al. (2019), Robust observational constraint of uncertain aerosol processes and emissions in a climate model and the effect on aerosol radiative forcing, *Atmos. Chem. Phys. Discuss.*, *2019*, 1-51, doi:10.5194/acp-2019-834.

Katoshevski, D., Nenes, A., and Seinfeld, J. H. (1999), A study of processes that govern the maintenance of aerosols in the marine boundary layer, *Journal of Aerosol Science*, *30*(4), 503-532, doi:Doi 10.1016/S0021-8502(98)00740-X.

Kazil, J., Wang, H., Feingold, G., Clarke, A. D., Snider, J. R., and Bandy, A. R. (2011), Modeling chemical and aerosol processes in the transition from closed to open cells during VOCALS-REx, *Atmospheric Chemistry and Physics*, *11*(15), 7491-7514, doi:10.5194/acp-11-7491-2011.

Kerminen, V.-M., Chen, X., Vakkari, V., Petäjä, T., Kulmala, M., and Bianchi, F. (2018), Atmospheric new particle formation and growth: review of field observations, *Environmental Research Letters*, *13*(10), doi:10.1088/1748-9326/aadf3c.

Kim, J., Yoon, Y. J., Gim, Y., Choi, J. H., Kang, H. J., Park, K.-T., Park, J., and Lee, B. Y. (2019), New particle formation events observed at King Sejong Station, Antarctic Peninsula – Part 1: Physical characteristics and contribution to cloud condensation nuclei, *Atmospheric Chemistry and Physics*, *19*(11), 7583-7594, doi:10.5194/acp-19-7583-2019.

Kim, J., Yoon, Y. J., Gim, Y., Kang, H. J., Choi, J. H., Park, K.-T., and Lee, B. Y. (2017), Seasonal variations in physical characteristics of aerosol particles at the King Sejong Station, Antarctic Peninsula, *Atmospheric Chemistry and Physics*, *17*(21), 12985-12999, doi:10.5194/acp-17-12985-2017.

King, M. D., Menzel, W. P., Kaufman, Y. J., Tanre, D., Bo-Cai, G., Platnick, S., Ackerman, S. A., Remer, L. A., Pincus, R., and Hubanks, P. A. (2003), Cloud and aerosol properties, precipitable water, and profiles of temperature and water vapor from MODIS, *Geoscience and Remote Sensing, IEEE Transactions on*, *41*(2), 442-458, doi:10.1109/TGRS.2002.808226.

Korhonen, H., Carslaw, K. S., Forster, P. M., Mikkonen, S., Gordon, N. D., and Kokkola, H. (2010), Aerosol climate feedback due to decadal increases in Southern Hemisphere wind speeds, *Geophysical Research Letters*, *37*, doi:10.1029/2009gl041320.

Korhonen, H., Carslaw, K. S., Spracklen, D. V., Mann, G. W., and Woodhouse, M. T. (2008), Influence of oceanic dimethyl sulfide emissions on cloud condensation nuclei concentrations and seasonality over the remote Southern Hemisphere oceans: A global model study, *J Geophys Res-Atmos*, *113*(D15), doi:D15204

10.1029/2007jd009718.

Kupc, A., Williamson, C., Wagner, N. L., Richardson, M., and Brock, C. A. (2018), Modification, calibration, and performance of the Ultra-High Sensitivity Aerosol Spectrometer for particle size distribution and volatility measurements during the Atmospheric Tomography Mission (ATom) airborne campaign, *Atmospheric Measurement Techniques*, *11*(1), 369-383, doi:10.5194/amt-11-369-2018.

Laboratory, U. N.-E. O. (2017), Low Rate (LRT - 1 sps) Navigation, State Parameter, and Microphysics Flight-Level Data, edited, doi:https://doi.org/10.5065/D65Q4T96.

Laboratory, U. N.-E. O. (2018), Low Rate (LRT - 1 sps) Navigation, State Parameter, and Microphysics Flight-Level Data. Version 1.1, edited by U. N.-E. O. Laboratory, doi:https://doi.org/10.5065/d65t3hwr.

Laboratory, U. N.-E. O. (2019), Low Rate (LRT - 1 sps) Navigation, State Parameter, and Microphysics Flight-Level Data, edited, doi: https://doi.org/10.5065/D6M32TM9

Lachlan-Cope, T., Beddows, D., Brough, N., Jones, A. E., Harrison, R. M., Lupi, A., Yoon, Y. J., Virkkula, A., and Dall'Osto, M. (2019), On the annual variability of Antarctic aerosol size distributions at Halley research station, *Atmos. Chem. Phys. Discuss.*, *2019*, 1-39, doi:10.5194/acp-2019-847.

Lachlan-Cope, T., Listowski, C., and O'Shea, S. (2016), The microphysics of clouds over the Antarctic Peninsula – Part 1: Observations, *Atmos. Chem. Phys.*, *16*(24), 15605-15617, doi:10.5194/acp-16-15605-2016.

Lana, A., et al. (2011), An updated climatology of surface dimethlysulfide concentrations and emission fluxes in the global ocean, *Global Biogeochemical Cycles*, *25*, doi:10.1029/2010gb003850.

Lee, L. A., Reddington, C. L., and Carslaw, K. S. (2016), On the relationship between aerosol model uncertainty and radiative forcing uncertainty, *Proc Natl Acad Sci U S A*, *113*(21), 5820-5827, doi:10.1073/pnas.1507050113.

Liu, J., Dedrick, J., Russell, L. M., Senum, G. I., Uin, J., Kuang, C., Springston, S. R., Leaitch, W. R., Aiken, A. C., and Lubin, D. (2018), High summertime aerosol organic functional group concentrations from marine and seabird sources at Ross Island, Antarctica, during AWARE, *Atmospheric Chemistry and Physics*, *18*(12), 8571-8587, doi:10.5194/acp-18-8571-2018.

Liu, X., Ma, P. L., Wang, H., Tilmes, S., Singh, B., Easter, R. C., Ghan, S. J., and Rasch, P. J. (2016), Description and evaluation of a new four-mode version of the Modal Aerosol Module (MAM4) within version 5.3 of the Community Atmosphere Model, *Geoscientific Model Development*, *9*(2), 505-522, doi:10.5194/gmd-9-505-2016.

Malavelle, F. F., et al. (2017), Strong constraints on aerosol–cloud interactions from volcanic eruptions, *Nature*, *546*(7659), 485-491, doi:10.1038/nature22974

http://www.nature.com/nature/journal/v546/n7659/abs/nature22974.html#supplementary-information.

Mauldin, R. L., Tanner, D. J., Heath, J. A., Huebert, B. J., and Eisele, F. L. (1999), Observations of H2SO4and MSA during PEM-Tropics-A, *Journal of Geophysical Research: Atmospheres*, *104*(D5), 5801-5816, doi:10.1029/98jd02612.

McCoy, D. T., Bender, F. A. M., Grosvenor, D. P., Mohrmann, J. K., Hartmann, D. L., Wood, R., and Field, P. R. (2018), Predicting decadal trends in cloud droplet number concentration using reanalysis and satellite data, *Atmospheric Chemistry and Physics*, *18*(3), 2035-2047, doi:10.5194/acp-18-2035-2018.

McCoy, D. T., Burrows, S. M., Wood, R., Grosvenor, D. P., Elliott, S. M., Ma, P.-L., Rasch, P. J., and Hartmann, D. L. (2015), Natural aerosols explain seasonal and spatial patterns of Southern Ocean cloud albedo, *Science Advances*, *1*(6), doi:10.1126/sciadv.1500157.

McCoy, I. L., Bretherton, C. S., Wood, R., Twohy, C. H., Gettleman, A., Bardeen, C. , and Toohey, D. W. (2020 submitted), Recent Particle Formation and Aerosol Variability Near Southern Ocean Low Clouds, *Journal of Geophysical Research: Atmospheres*, doi:10.1002/essoar.10503719.1.

McCoy, I. L., et al. (2020), The hemispheric contrast in cloud microphysical properties constrains aerosol forcing, *Proc Natl Acad Sci U S A*, *117*(32), 18998-19006, doi:10.1073/pnas.1922502117.

McFarquhar, G., et al. (2020 submitted), Observations of clouds, aerosols, precipitation, and surface radiation over the Southern Ocean: An overview of CAPRICORN, MARCUS, MICRE and SOCRATES, *Bull. Amer. Meteorol. Soc.*

Meskhidze, N., and Nenes, A. (2006), Phytoplankton and Cloudiness in the Southern Ocean, *Science*, *314*(5804), 1419-1423, doi:10.1126/science.1131779.

Mohrmann, J., Wood, R., McGibbon, J., Eastman, R., and Luke, E. (2018), Drivers of Seasonal Variability in Marine Boundary Layer Aerosol Number Concentration Investigated Using a Steady State Approach, *Journal of Geophysical Research: Atmospheres*, *123*(2), 1097-1112, doi:10.1002/2017jd027443.

Mulcahy, J. P., et al. (2018), Improved Aerosol Processes and Effective Radiative Forcing in HadGEM3 and UKESM1, *J. Adv. Model. Earth Syst.*, *10*(11), 2786-2805, doi:10.1029/2018ms001464.

Myhre, G., et al. (2013), Radiative forcing of the direct aerosol effect from AeroCom Phase II simulations, *Atmospheric Chemistry and Physics*, *13*(4), 1853-1877, doi:10.5194/acp-13-1853-2013.

Noone, K. J., Ogren, J. A., Heintzenberg, J., Charlson, R. J., and Covert, D. S. (1988), Design and Calibration of a Counterflow Virtual Impactor for Sampling of Atmospheric Fog and Cloud Droplets, *Aerosol Science and Technology*, *8*(3), 235-244, doi:10.1080/02786828808959186.

O, K.-T., Wood, R., and Bretherton, C. S. (2018), Ultraclean Layers and Optically Thin Clouds in the Stratocumulus-to-Cumulus Transition. Part II: Depletion of Cloud Droplets and Cloud

Condensation Nuclei through Collision-Coalescence, *Journal of the Atmospheric Sciences*, *75*(5), 1653-1673, doi:10.1175/Jas-D-17-0218.1.

O'Dowd, C. D., Facchini, M. C., Cavalli, F., Ceburnis, D., Mircea, M., Decesari, S., Fuzzi, S., Yoon, Y. J., and Putaud, J. P. (2004), Biogenically driven organic contribution to marine aerosol, *Nature*, *431*(7009), 676-680, doi:10.1038/nature02959.

O'Dowd, C. D., Lowe, J. A., Smith, M. H., Davison, B., Hewitt, N., and Harrison, R. M. (1997), Biogenic sulphur emissions and inferred non-sea-salt-sulphate cloud condensation nuclei in and around Antarctica, *Journal of Geophysical Research-Atmospheres*, *102*(11D), 12839-12854, doi:10.1029/96jd02749.

Orsini, D. A., Wiedensohler, A., Stratmann, F., and Covert, D. S. (1999), A New Volatility Tandem Differential Mobility Analyzer to Measure the Volatile Sulfuric Acid Aerosol Fraction, *Journal of Atmospheric and Oceanic Technology*, *16*(6), 760-772, doi:10.1175/1520-0426(1999)016<0760:Anvtdm>2.0.Co;2.

Painemal, D., Minnis, P., Ayers, J. K., and O'Neill, L. (2012), GOES-10 microphysical retrievals in marine warm clouds: Multi-instrument validation and daytime cycle over the southeast Pacific, *Journal of Geophysical Research: Atmospheres*, *117*(D19), n/a-n/a, doi:10.1029/2012jd017822.

Painemal, D., and Zuidema, P. (2011), Assessment of MODIS cloud effective radius and optical thickness retrievals over the Southeast Pacific with VOCALS-REx in situ measurements, *Journal of Geophysical Research-Atmospheres*, *116*, doi:10.1029/2011jd016155.

Pandis, S. N., Russell, L. M., and Seinfeld, J. H. (1994), The relationship between DMS flux and CCN concentration in remote marine regions, *Journal of Geophysical Research*, *99*(D8), 16945-16957, doi:10.1029/94jd01119.

Petrou, K., Kranz, S. A., Trimborn, S., Hassler, C. S., Ameijeiras, S. B., Sackett, O., Ralph, P. J., and Davidson, A. T. (2016), Southern Ocean phytoplankton physiology in a changing climate, *J Plant Physiol*, *203*, 135-150, doi:10.1016/j.jplph.2016.05.004.

Quinn, P. K., Kapustin, V. N., Bates, T. S., and Covert, D. S. (1996), Chemical and optical properties of marine boundary layer aerosol particles of the mid-Pacific in relation to sources and meteorological transport, *Journal of Geophysical Research: Atmospheres*, *101*(D3), 6931-6951, doi:10.1029/95jd03444.

Reddington, C., Carslaw, K., Stier, P., Schutgens, N., Coe, H., Liu, D., Allan, J., Pringle, K., Lee, L., and Yoshioka, M. (2017), The Global Aerosol Synthesis and Science Project (GASSP): measurements and modelling to reduce uncertainty.

Regayre, L. A., Johnson, J. S., Yoshioka, M., Pringle, K. J., Sexton, D. M., Booth, B. B., Lee, L. A., Bellouin, N., and Carslaw, K. S. (2018), Aerosol and physical atmosphere model parameters are both important sources of uncertainty in aerosol ERF, *Atmospheric Chemistry and Physics*, *18*(13), 9975-10006.

Regayre, L. A., Pringle, K. J., Booth, B. B. B., Lee, L. A., Mann, G. W., Browse, J., Woodhouse, M. T., Rap, A., Reddington, C. L., and Carslaw, K. S. (2014), Uncertainty in the magnitude of aerosol-cloud radiative forcing over recent decades, *Geophysical Research Letters*, *41*(24), 9040-9049, doi:10.1002/2014gl062029.

Regayre, L. A., Schmale, J., Johnson, J. S., Tatzelt, C., Baccarini, A., Henning, S., Yoshioka, M., Stratmann, F., Gysel-Beer, M., and Carslaw, K. S. (2019), The value of remote marine aerosol measurements for constraining radiative forcing uncertainty, *Atmos. Chem. Phys. Discuss.*, *2019*, 1-11, doi:10.5194/acp-2019-1085.

Revell, L. E., et al. (2019), The sensitivity of Southern Ocean aerosols and cloud microphysics to sea spray and sulfate aerosol production in the HadGEM3-GA7.1 chemistry–climate model, *Atmos. Chem. Phys.*, *19*(24), 15447-15466, doi:10.5194/acp-19-15447-2019.

Sanchez, K. J., et al. (2018), Substantial Seasonal Contribution of Observed Biogenic Sulfate Particles to Cloud Condensation Nuclei, *Sci Rep*, *8*(1), 3235, doi:10.1038/s41598-018-21590-9.

Sato, Y., Goto, D., Michibata, T., Suzuki, K., Takemura, T., Tomita, H., and Nakajima, T. (2018), Aerosol effects on cloud water amounts were successfully simulated by a global cloud-system resolving model, *Nature Communications*, *9*(1), 985.

Schmale, J., et al. (2019), Overview of the Antarctic Circumnavigation Expedition: Study of Preindustrial-like Aerosols and Their Climate Effects (ACE-SPACE), *Bulletin of the American Meteorological Society*, *100*(11), 2260-2283, doi:10.1175/bams-d-18-0187.1.

Schmid, O., Eimer, B., Hagen, D. E., and Whitefield, P. D. (2002), Investigation of Volatility Method for Measuring Aqueous Sulfuric Acid on Mixed Aerosols, *Aerosol Science and Technology*, *36*(8), 877-889, doi:10.1080/02786820290038519.

Schulz, M., et al. (2006), Radiative forcing by aerosols as derived from the AeroCom present-day and pre-industrial simulations, *Atmos. Chem. Phys.*, *6*(12), 5225-5246, doi:10.5194/acp-6-5225-2006.

Seethala, C., and Horvath, A. (2010), Global assessment of AMSR-E and MODIS cloud liquid water path retrievals in warm oceanic clouds, *Journal of Geophysical Research-Atmospheres*, *115*, doi:10.1029/2009jd012662.

Seinfeld, J. H., and Pandis, S. N. (2006), *Atmospheric chemistry and physics from air pollution to climate change*, Second edition. ed., Hoboken, New Jersey : John Wiley & Sons, Inc.

Smith, W. O., and Nelson, D. M. (1986), Importance of Ice Edge Phytoplankton Production in the Southern Ocean, *BioScience*, *36*(4), 251-257, doi:10.2307/1310215.

Stein, A. F., Draxler, R. R., Rolph, G. D., Stunder, B. J. B., Cohen, M. D., and Ngan, F. (2015), NOAA's HYSPLIT Atmospheric Transport and Dispersion Modeling System, *Bulletin of the American Meteorological Society*, *96*(12), 2059-2077, doi:10.1175/bams-d-14-00110.1.

Stephens, B. B., et al. (2018), The O2/N2 Ratio and CO2 Airborne Southern Ocean Study, *Bulletin of the American Meteorological Society*, *99*(2), 381-402, doi:10.1175/bams-d-16-0206.1.

Stephens, G. L., L'Ecuyer, T., Forbes, R., Gettelmen, A., Golaz, J.-C., Bodas-Salcedo, A., Suzuki, K., Gabriel, P., and Haynes, J. (2010), Dreary state of precipitation in global models, *Journal of Geophysical Research: Atmospheres*, *115*(D24), doi:10.1029/2010jd014532.

Stier, P., Feichter, J., Kloster, S., Vignati, E., and Wilson, J. (2006), Emission-induced nonlinearities in the global aerosol system: Results from the ECHAM5-HAM aerosol-climate model, *Journal of climate*, *19*(16), 3845-3862.

Sullivan, C. W., McClain, C. R., Comiso, J. C., and Smith, W. O. (1988), Phytoplankton standing crops within an Antarctic ice edge assessed by satellite remote sensing, *Journal of Geophysical Research*, *93*(C10), 12487, doi:10.1029/JC093iC10p12487.

Telford, P. J., Braesicke, P., Morgenstern, O., and Pyle, J. A. (2008), Technical Note: Description and assessment of a nudged version of the new dynamics Unified Model, *Atmos. Chem. Phys.*, *8*(6), 1701-1712, doi:10.5194/acp-8-1701-2008.

Toll, V., Christensen, M., Gassó, S., and Bellouin, N. (2017), Volcano and Ship Tracks Indicate Excessive Aerosol-Induced Cloud Water Increases in a Climate Model, *Geophysical Research Letters*, *44*(24), 12,492-412,500, doi:10.1002/2017GL075280.

Toll, V., Christensen, M., Quaas, J., and Bellouin, N. (2019), Weak average liquid-cloud-water response to anthropogenic aerosols, *Nature*, *572*(7767), 51-55, doi:10.1038/s41586-019-1423-9.

Twohy, C. H., et al. (2013), Impacts of aerosol particles on the microphysical and radiative properties of stratocumulus clouds over the southeast Pacific Ocean, *Atmospheric Chemistry and Physics*, *13*(5), 2541-2562, doi:10.5194/acp-13-2541-2013.

Twohy, C. H., et al. (2002), Deep convection as a source of new particles in the midlatitude upper troposphere, *Journal of Geophysical Research: Atmospheres*, *107*(D21), AAC 6-1-AAC 6-10, doi:10.1029/2001jd000323.

Twohy, C. H., et al. (2020 submitted), Cloud-Nucleating Particles over the Southern Ocean in a Changing Climate, *Atmospheric Chemistry & Physics Discussion*.

Twohy, C. H., Schanot, A. J., and Cooper, W. A. (1997), Measurement of Condensed Water Content in Liquid and Ice Clouds Using an Airborne Counterflow Virtual Impactor, *Journal of Atmospheric and Oceanic Technology*, *14*(1), 197-202, doi:10.1175/1520-0426(1997)014<0197:Mocwci>2.0.Co;2.

Twomey, S. (1977), The Influence of Pollution on the Shortwave Albedo of Clouds, *Journal of the Atmospheric Sciences*, *34*(7), 1149-1152, doi:10.1175/1520-0469(1977)034<1149:Tiopot>2.0.Co;2.

Wang, Z., Siems, S. T., Belusic, D., Manton, M. J., and Huang, Y. (2015), A climatology of the precipitation over the Southern Ocean as observed at Macquarie Island, *Journal of Applied Meteorology and Climatology*, *54*(12), 2321-2337.

Watson-Parris, D., et al. (2020), Constraining uncertainty in aerosol direct forcing, *Geophysical Research Letters*, doi:10.1029/2020gl087141.

Weber, R. J., Chen, G., Davis, D. D., Mauldin, R. L., Tanner, D. J., Eisele, F. L., Clarke, A. D., Thornton, D. C., and Bandy, A. R. (2001), Measurements of enhanced H2SO4 and 3-4 nm particles near a frontal cloud during the First Aerosol Characterization Experiment (ACE 1), *Journal of Geophysical Research-Atmospheres*, *106*(D20), 24107-24117, doi:10.1029/2000jd000109.

Williams, K. D., Bodas-Salcedo, A., Déqué, M., Fermepin, S., Medeiros, B., Watanabe, M., Jakob, C., Klein, S. A., Senior, C. A., and Williamson, D. L. (2013), The Transpose-AMIP II Experiment and Its Application to the Understanding of Southern Ocean Cloud Biases in Climate Models, *Journal of Climate*, *26*(10), 3258-3274, doi:10.1175/jcli-d-12-00429.1.

Williamson, C. J., et al. (2019), A large source of cloud condensation nuclei from new particle formation in the tropics, *Nature*, *574*(7778), 399-403, doi:10.1038/s41586-019-1638-9.

Witte, M. K., Yuan, T., Chuang, P. Y., Platnick, S., Meyer, K. G., Wind, G., and Jonsson, H. H. (2018), MODIS Retrievals of Cloud Effective Radius in Marine Stratocumulus Exhibit No Significant Bias, *Geophysical Research Letters*, *45*(19), 10,656-610,664, doi:10.1029/2018gl079325.

Wood, R. (2006a), Rate of loss of cloud droplets by coalescence in warm clouds, *Journal of Geophysical Research: Atmospheres*, *111*(D21).

Wood, R. (2006b), Relationships between optical depth, liquid water path, droplet concentration, and effective radius in an adiabatic layer cloud.

Wood, R. (2012), Stratocumulus Clouds, *Monthly Weather Review*, *140*(8), 2373-2423, doi:10.1175/mwr-d-11-00121.1.

Wood, R., Leon, D., Lebsock, M., Snider, J., and Clarke, A. D. (2012), Precipitation driving of droplet concentration variability in marine low clouds, *Journal of Geophysical Research: Atmospheres*, *117*(D19), n/a-n/a, doi:10.1029/2012jd018305.

Wood, R., et al. (2018), Ultraclean Layers and Optically Thin Clouds in the Stratocumulus-to-Cumulus Transition. Part I: Observations, *Journal of the Atmospheric Sciences*, *75*(5), 1631-1652, doi:10.1175/jas-d-17-0213.1.

Wood, R., Wyant, M., Bretherton, C. S., Rémillard, J., Kollias, P., Fletcher, J., Stemmler, J., De Szoeke, S., Yuter, S., and Miller, M. (2015), Clouds, aerosols, and precipitation in the marine boundary layer: An arm mobile facility deployment, *Bulletin of the American Meteorological Society*, *96*(3), 419-440.

Yoshioka, M., et al. (2019), Ensembles of Global Climate Model Variants Designed for the Quantification and Constraint of Uncertainty in Aerosols and Their Radiative Forcing, *J. Adv. Model. Earth Syst.*, doi:10.1029/2019ms001628.

Yu, F., and Luo, G. (2010), Oceanic Dimethyl Sulfide Emission and New Particle Formation around the Coast of Antarctica: A Modeling Study of Seasonal Variations and Comparison with Measurements, *Atmosphere*, *1*(1), 34-50, doi:10.3390/atmos1010034.

Zheng, G., et al. (2018), Marine boundary layer aerosol in the eastern North Atlantic: seasonal variations and key controlling processes, *Atmospheric Chemistry and Physics*, *18*(23), 17615-17635, doi:10.5194/acp-18-17615-2018.

Zhou, X., Atlas, R., McCoy, I. L., Bretherton, C. S., Bardeen, C., Gettelman, A., Lin, P., and Ming, Y. (2020 submitted), Evaluation of cloud and precipitation simulations in CAM6 and AM4 using observations over the Southern Ocean, *Journal of Geophysical Research: Atmospheres*.

APPENDIX A: CHAPTER 2 SUPPLEMENTAL INFORMATION

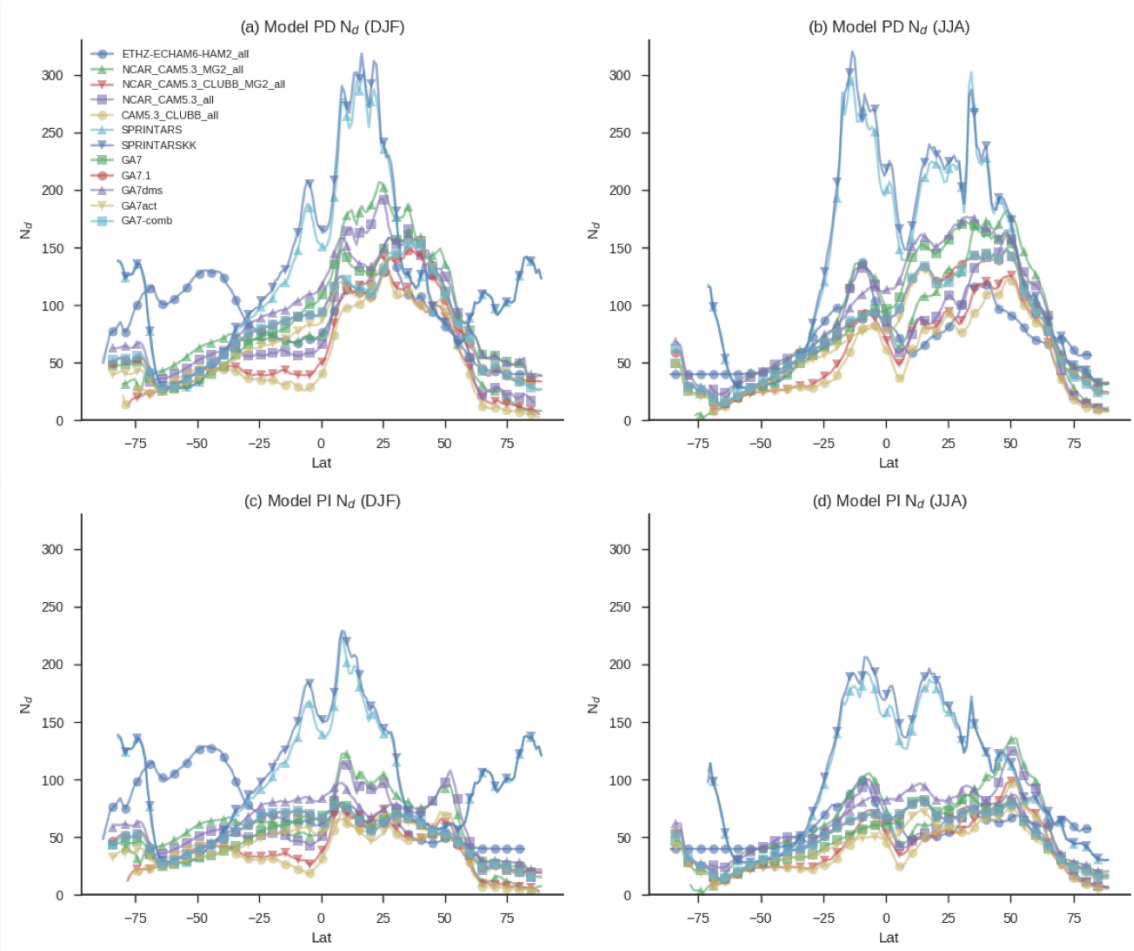

Figure SI 2- 3 *Oceanic Present Day (a, b) and Pre-Industrial (c, d) seasonal mean N_d from Aerocom-II models [Ghan et al., 2016] and HadGEM3-GA7.0 and GA7.1 [Mulcahy et al., 2018] models for DJF (a, c) and JJA (b, d).*

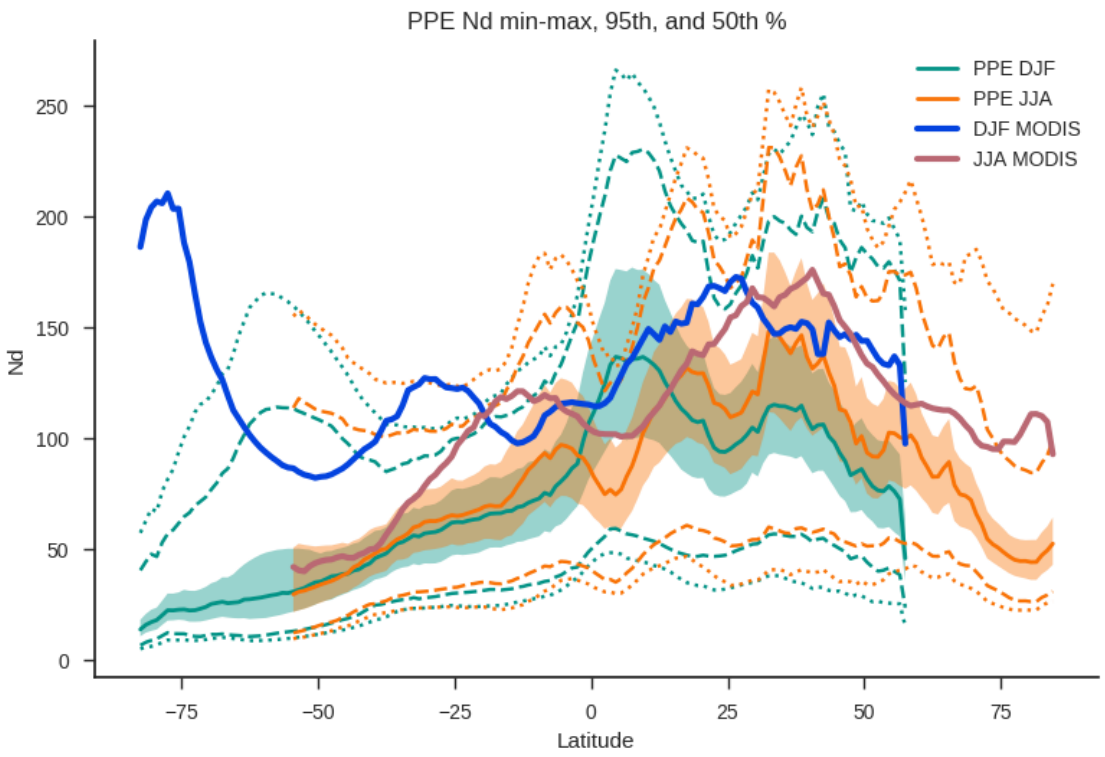

Figure SI 2- 4 *Zonal-mean oceanic PD N_d from PPE model members [Yoshioka et al., 2019]. The median (solid lines), 50th (shading) and 95th percentile (dashed lines), and minimum and maximum (dotted lines) of all ensemble members are shown for DJF and JJA. MODIS observations for DJF and JJA are shown for reference [Grosvenor, 2018]. Geographically resolved PI N_d was not archived from the PPE at the time of integration.*

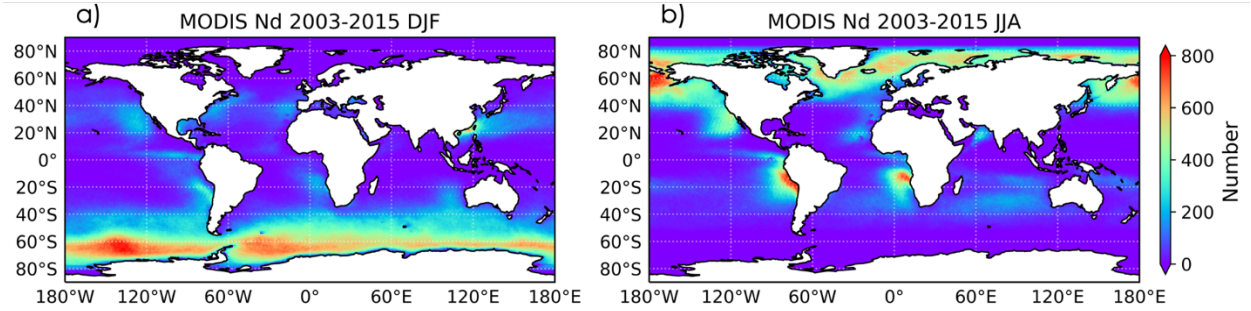

Figure SI 2- 5 *MODIS N_d number of observations over 2003-2015 for DJF (a) and JJA (b).*

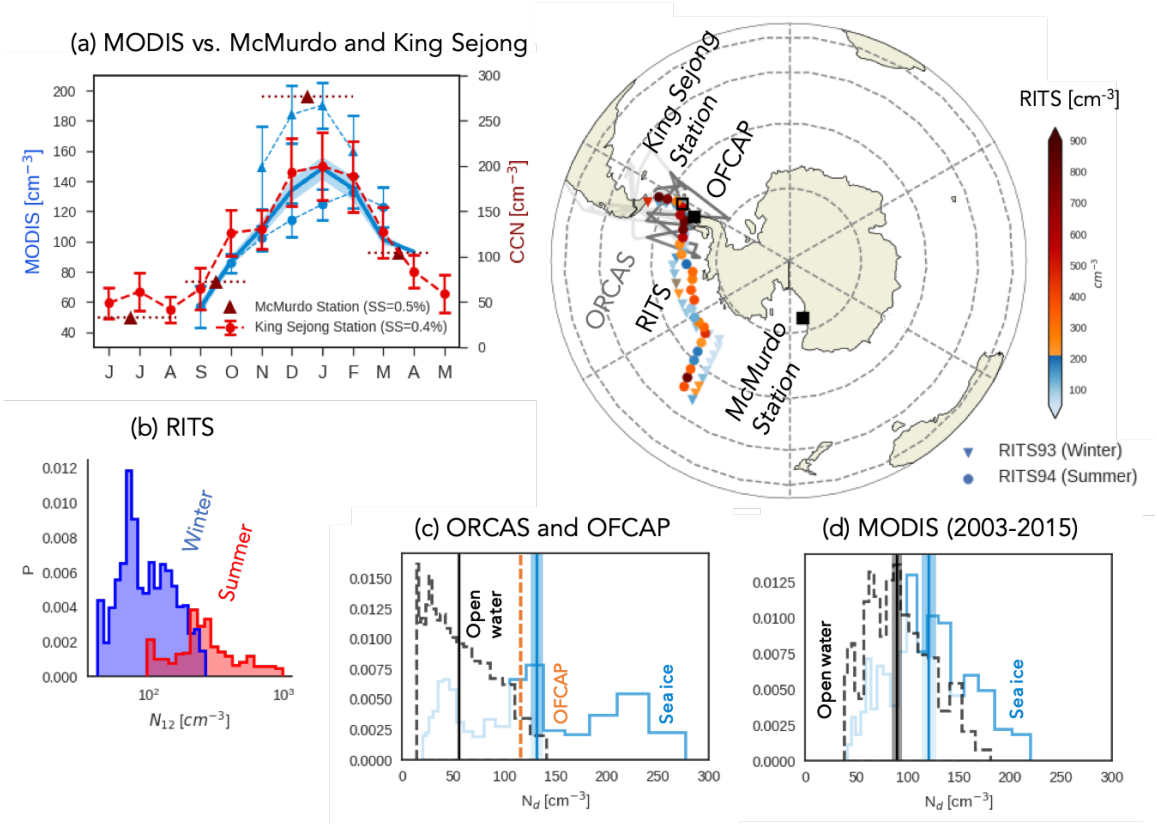

Figure SI 2- 6 *Map of Southern Ocean field campaign locations with colors marking RITS [Covert et al., 1996; Quinn et al., 1996] condensation nuclei (aerosol diameter > 12 nm) from Winter (triangles) and Summer (circles). Locations of the OFCAP [Lachlan-Cope et al., 2016] and ORCAS [Stephens et al., 2018] campaigns, McMurdo Station [Liu et al., 2018], and King Sejong Station [Kim et al., 2017] are also marked. (a) Seasonal cloud condensation nuclei concentrations from McMurdo Station (red triangle, 0.5% saturation) and King Sejong Station (red dots, 0.4% saturation). MODIS N_d poleward of 60°S (solid blue line) and in 4° boxes centered at McMurdo Station (blue triangles) and King Sejong Station (blue dots). The interannual standard deviation in the monthly mean MODIS N_d is shown as shading for the zonal mean poleward of 60°S and as error bars for station means. (b) PDF for RITS Winter '93 (blue), Summer '94 (red) CN concentration as in map. (c) PDFs of summertime N_d observations from ORCAS which have been separated into observations taken where some sea ice is present (blue) and over ice-free water (grey) based on OSTIA sea ice extent [Donlon et al., 2012] interpolated to the flight track. Mean values are shown with vertical lines. The OFCAP campaign mean N_d is shown for reference. (d) Summertime MODIS N_d from 2003-2015 following the ORCAS flight track are shown separated by OSTIA sea ice extent as in (c).*

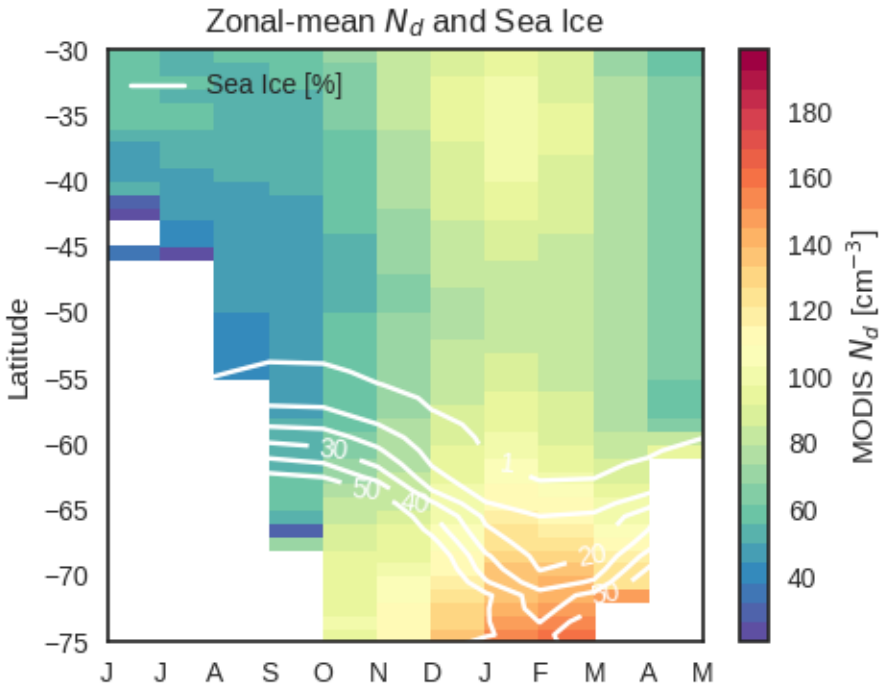

Figure SI 2- 7 *Seasonal cycle of Southern Ocean N_d from MODIS (colors) with OSTIA sea ice extent (white lines) included for reference. Data has been masked to remove land.*

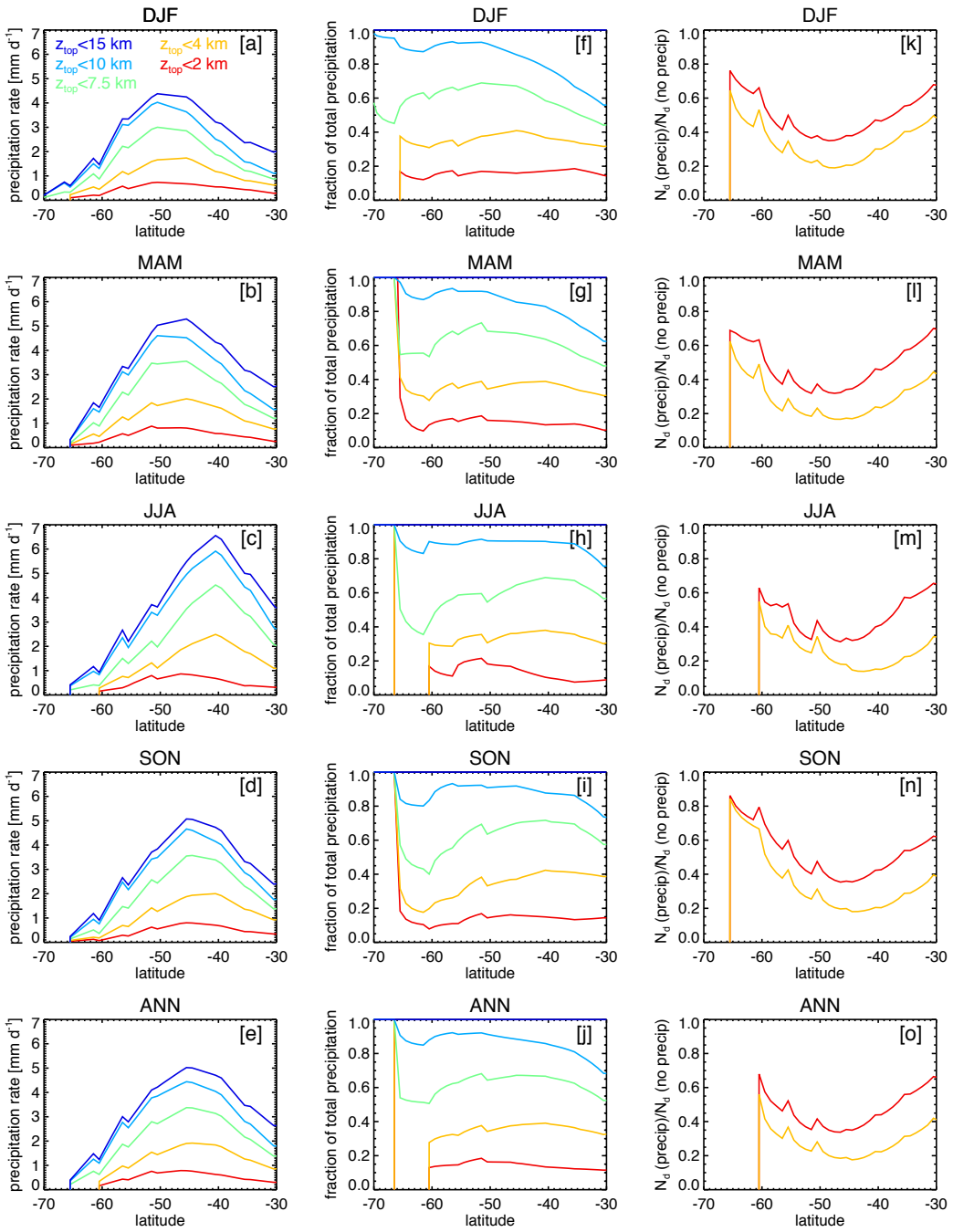

Figure SI 2- 8 *Seasonal (a-d) and annual (e) zonal mean area-averaged precipitation rates [Haynes et al., 2009] emanating from columns with maximum echo top heights lower than the color-coded values indicated on panel (a). Panels (f-j) show the same information but as a fraction of the total precipitation, with color coding the same as in panels (a-e). Panels (k-o) show the MBL CCN and N_d budget model [Wood et al., 2012] estimates of the relative suppression of N_d by coalescence scavenging (detailed in methods), using precipitation with echo*

tops below either 2 km (red) or 4 km (yellow) as a means to bound the expected impact of low cloud precipitation on N_d.

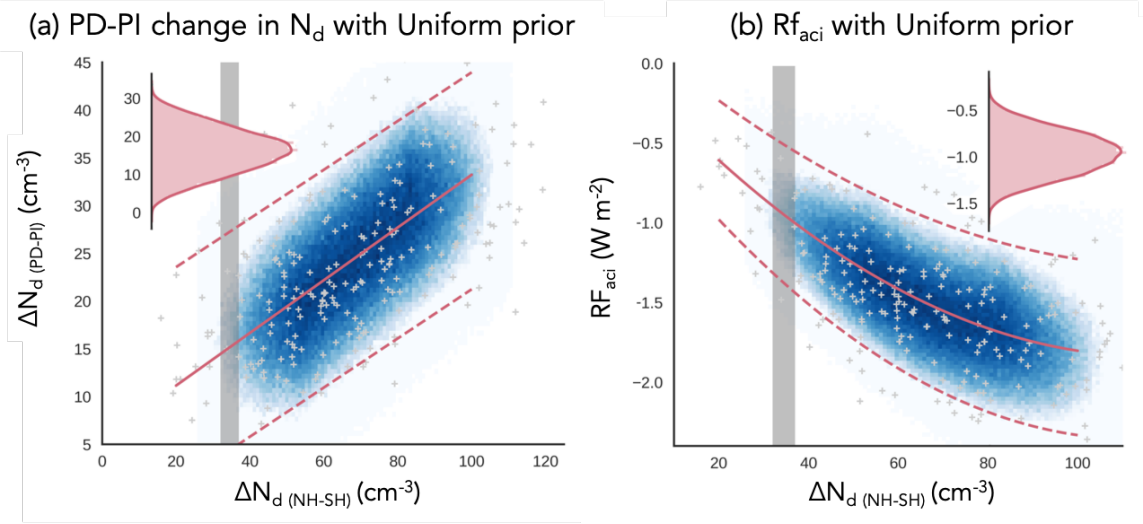

Figure SI 2- 9 *As in Figure 2-1b, c but assuming uniform pdf priors [Johnson et al., 2018; Regayre et al., 2018; Johnson et al., 2019; Regayre et al., 2019] to generate the PPE sample members (blue shading) from the individual model members (white crosses) [Watson-Parris et al., 2020]. (Insets) The PDF of the emulated PPE member values within the observationally constrained range of $\Delta N_{d(NH-SH)}$ (gray) is shown in the top left for $\Delta N_{d(PD-PI)}$ (a) and top right for RF_{aci} (b).*

APPENDIX B: CHAPTER 3 SUPPLEMENTAL INFORMATION

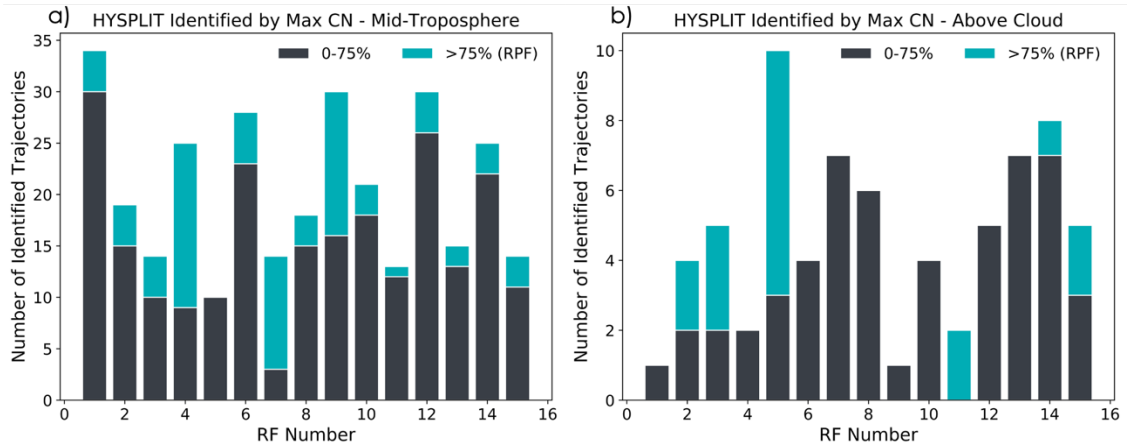

Figure SI 3- 1 *Number of RPF (blue) vs non-RPF identified HYSPLIT trajectories by research flight for trajectories initiated in the (a) mid-troposphere and (b) above cloud.*

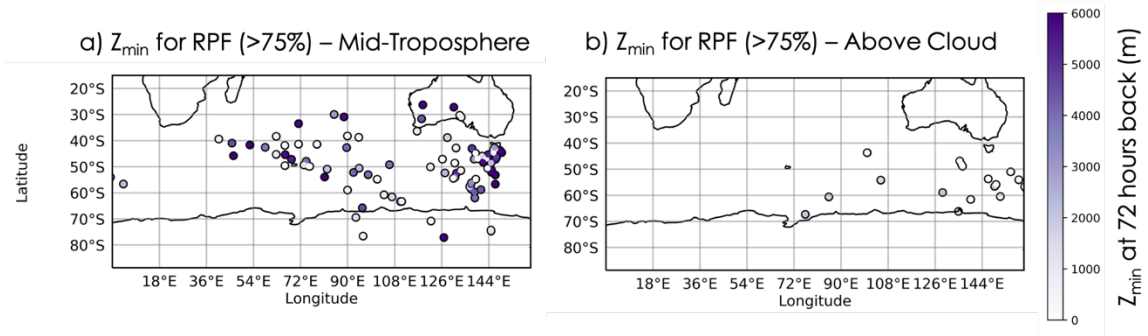

Figure SI 3- 2 *Location and altitude of minimum height that occurs over full 72 hours for RPF identified trajectories in (a) mid-troposphere and (b) above cloud.*

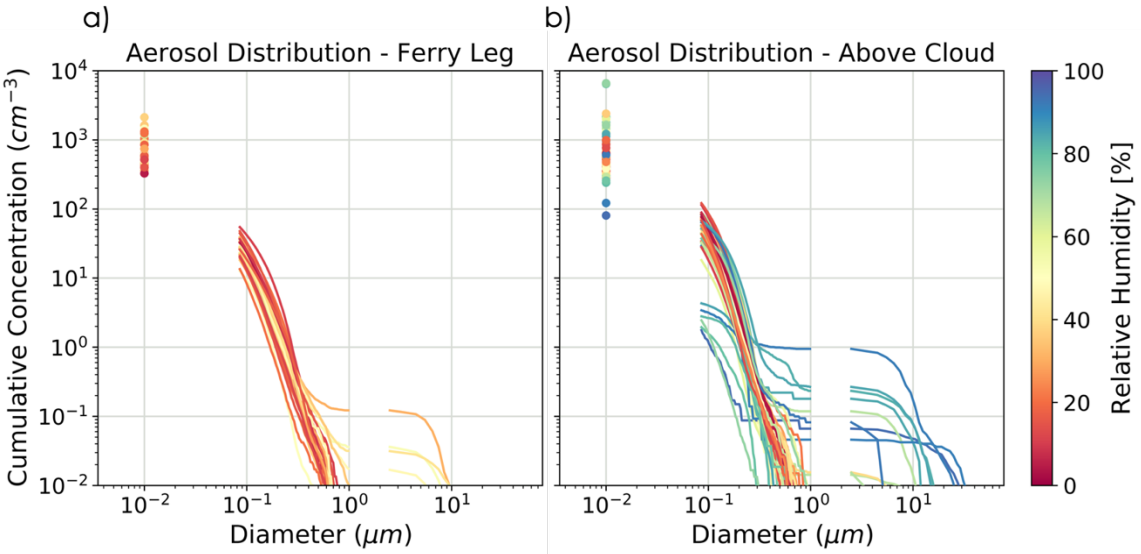

Figure SI 3- 3 *Median cumulative size distributions for each level leg in the mid-troposphere (a) and above cloud (b) sampled during the campaign. Each line is colored by the median relative humidity to indicate where near cloud contamination may be occurring. Note that concentrations are not adjusted for standard temperature and pressure.*

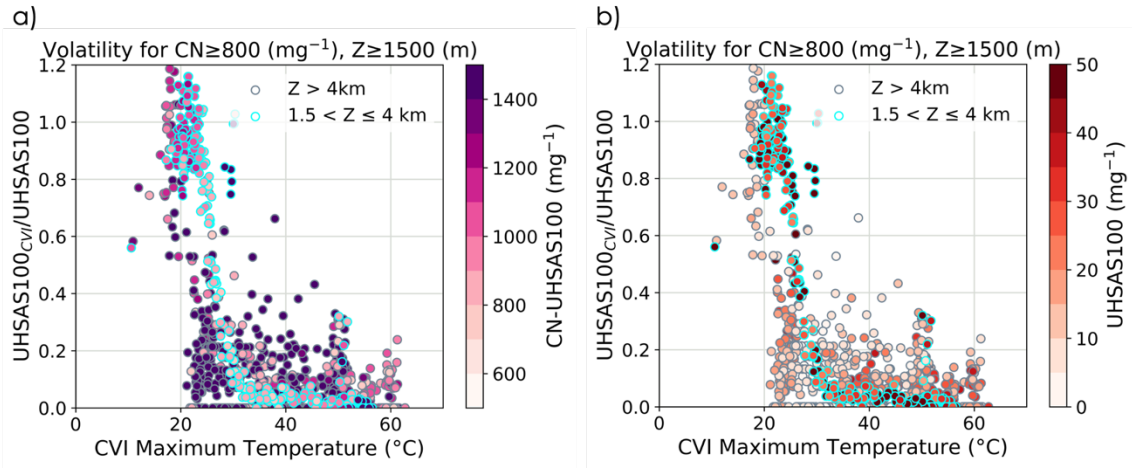

Figure SI 3- 4 *Volatility curves from CVI analysis as in Figure 3-7 but for the small number of accumulation mode particles captured in these Aitken-dominated samples. Accumulation mode volatilization is presented as ratio between UHSAS100 and $UHSAS100_{CVI}$ versus the maximum temperature of the CVI instrument. Points are shown for CN ≥ 800 mg^{-1} and limited to free troposphere samples (Z ≥ 1.5 km). Outline colors denote altitude of sample: mid-troposphere (gray) and above cloud (blue). Points are colored to estimate the number of particles in the (a, CN-UHSAS100) Aitken mode (generally more in the mid-troposphere) and (b, UHSAS100) accumulation mode. Note that accumulation number in these Aitken-dominated*

samples are rarely more than 30 mg^{-1} in mid-troposphere and increase only to ~50 mg^{-1} above cloud.

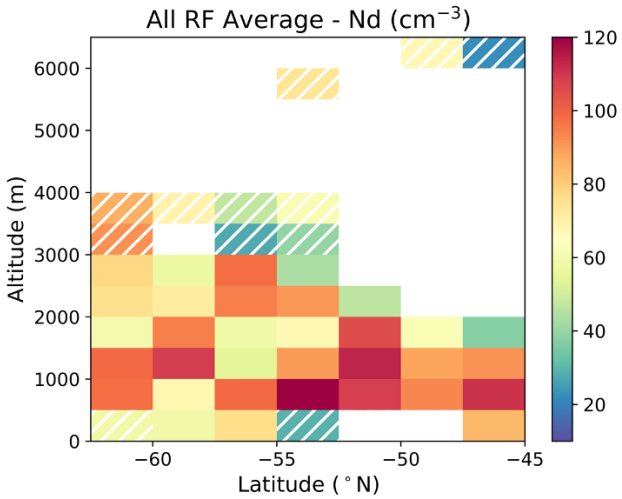

Figure SI 3- 5 *All flight average composite of binned flight medians (500 m x 2.5° boxes) for cloud droplet number concentration as in Figure 3-8d but using volume units (cm^{-3}) instead of standard temperature and pressure corrected units (mg^{-1}). Bins where 2 or less flights sampled are hatched to indicate reliability of sampling.*

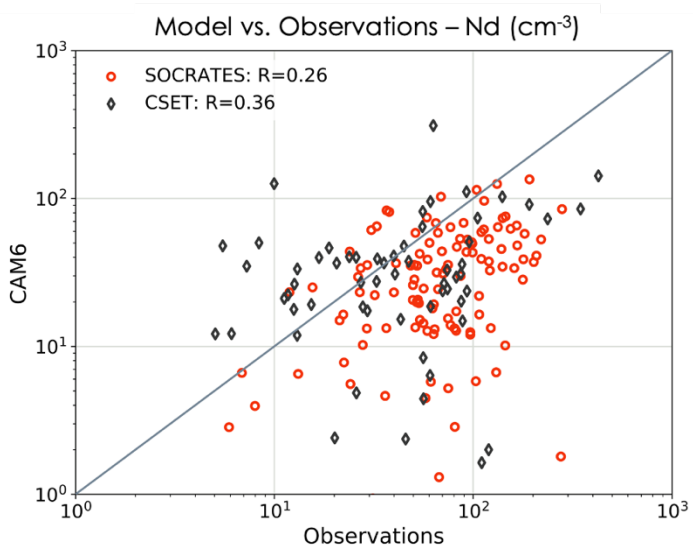

Figure SI 3- 6 *Comparison of N_d between CAM6 and observations from all CSET (gray) and SOCRATES (orange) flights. Each point used in the scatter represents a 500 m x 2.5° bin mean value for a given flight during the campaign. A reference 1:1 line is included along with correlation coefficients computed for the linear relationship between CAM6 and observations.*

CAM6 over produces precipitation-depleted clouds ($N_d \leq 10$ cm^{-3}) relative to SOCRATES observations and are not collocated with actual observations for either CSET or SOCRATES.

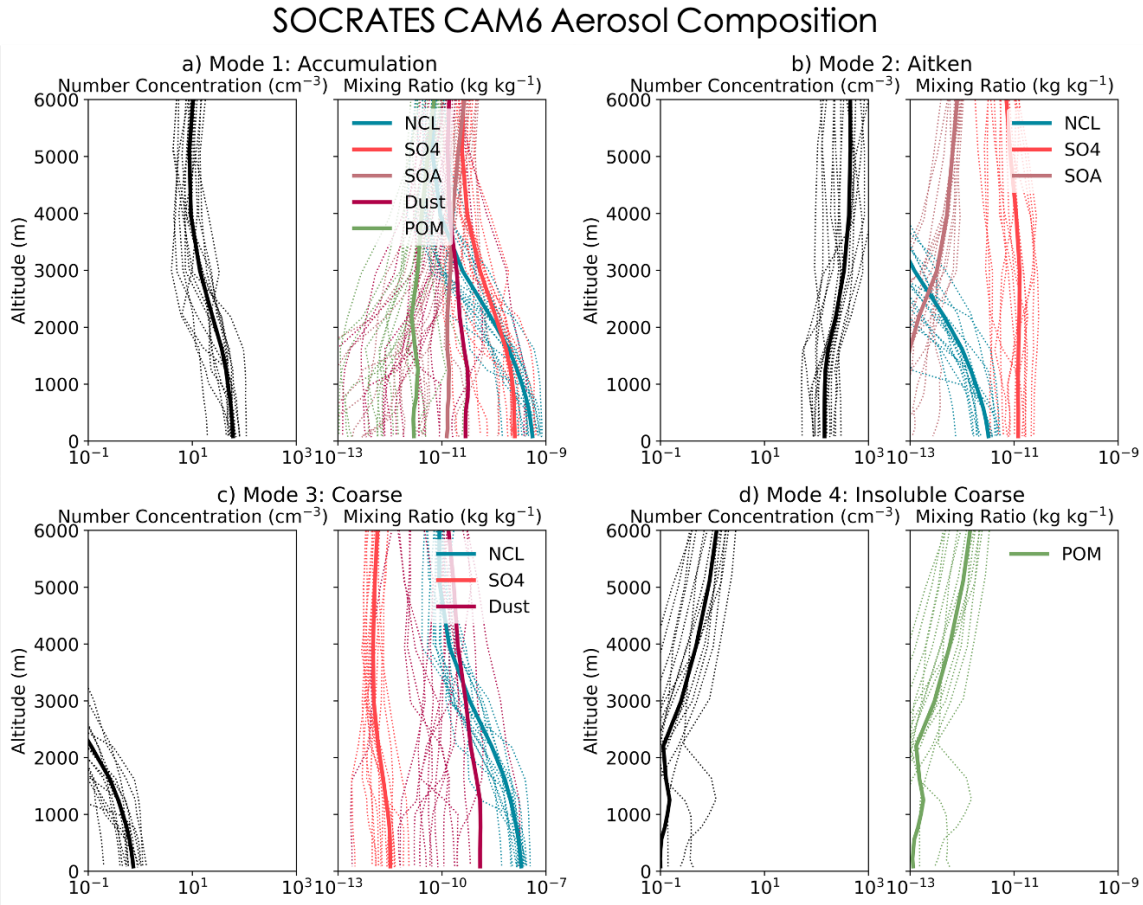

Figure SI 3- 7 *Aerosol Number Concentrations (left) and Mixing Ratios (right) for nudged SOCRATES CAM6 Aerosol Modes: Accumulation (a), Aitken (b), Coarse (c), and Insoluble Coarse (d). All levels and extent of model data extracted along the Latitude-Longitude flight path is included to understand overall model behavior. Dashed lines are individual flight means and solid line is campaign average tendency.*

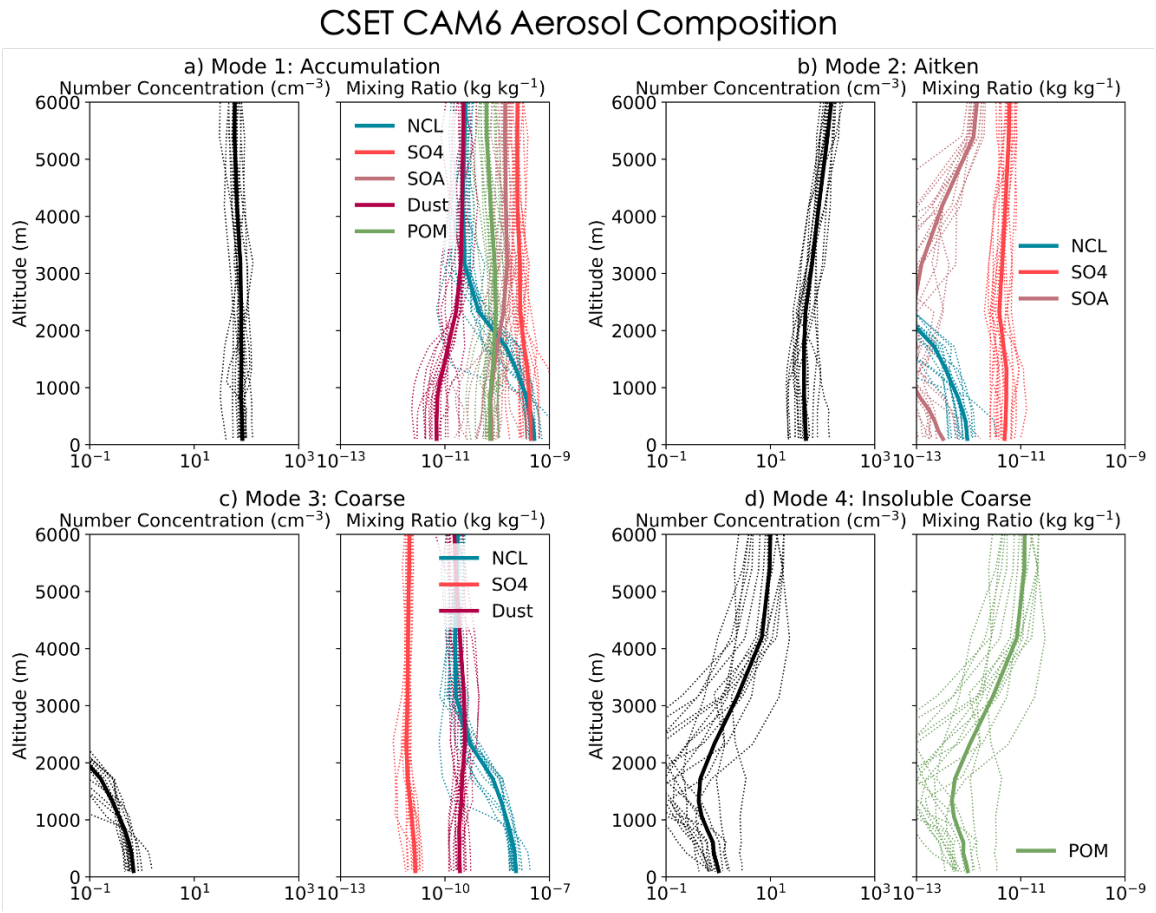

Figure SI 3- 8 *As in Figure SI 3- 7 but for nudged CSET CAM6 simulations.*

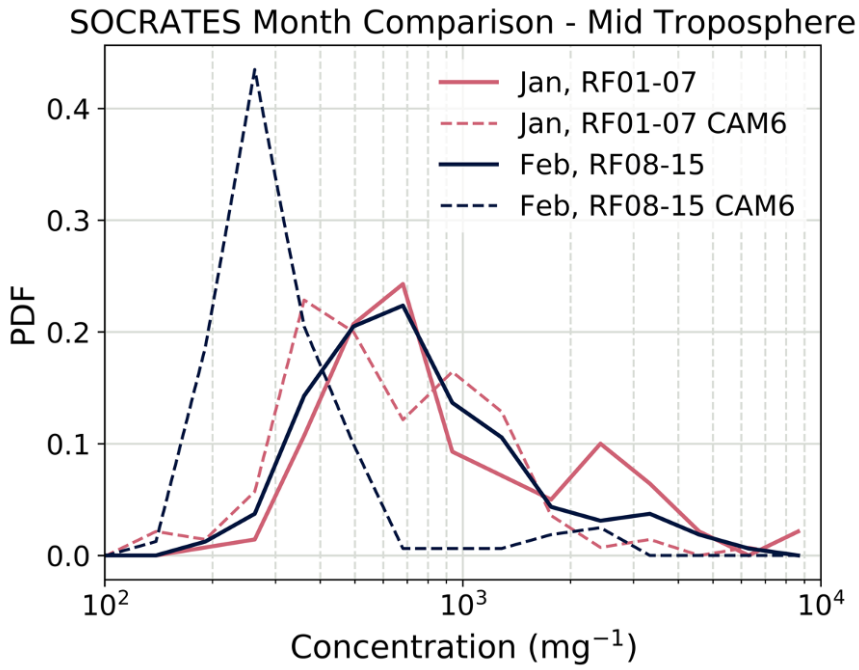

Figure SI 3- 9 *Observed CN number concentration in the mid-troposphere for January (RF01-07) and February (RF08-15) samples are found to have similar PDFs, suggesting statistically consistent CN concentrations across these months. CAM6 matched CN has distinctly different PDFs for January and February, with February producing much lower number concentrations than January and far too low relative to observations. Both CAM6 month PDFs under produce high concentrations of aerosol (CN ≥ 2000 mg^{-1}) relative to observations.*

Movie SI 3- 1 *Synoptic scale patterns influencing mid-tropospheric RPF identified air masses in the 72-hour period before sampling by RF07 (black line from Tasmania). ERA5 reanalysis maps include 700 hPa vertical velocity (colors) with a 700 hPa geopotential height contour of 2.9 km for reference (black contour). RPF trajectories (gray lines) with air mass locations (circles) colored by their altitude (white to purple, as in the ascent profiles in Figure 3-5a). Ascent of the first set of trajectories at ~60-hr occurs off the tip of Africa while ascent of the ~36-hr trajectories occurs off the coast of Antarctica, both driven by the advance of a warm-conveyor belt towards the south east (i.e. along the height contour).*

VITA

Isabel was born and raised in the village of Socorro in the southern part of New Mexico. She earned her B.S. in Physics from the New Mexico Institute of Mining and Technology in 2014. She first began working with Rob Wood during a research experience for undergraduates at the Joint Institute for the Study of the Atmosphere and Ocean (2012-2013) and continued working with him throughout her tenure at the University of Washington (2014-2020). After earning her M.S. in 2017, Isabel also began collaborating closely with Chris Bretherton (2017-2020). Isabel has had the opportunity to participate in several field campaigns while at the University of Washington: *the Cloud Systems Evolution in the Trades* (CSET, 2015), *the Southern Ocean Clouds, Radiation, Transport Experimental Study* (SOCRATES, 2018), and the joint campaign *Elucidating the role of clouds-circulation coupling in climate / the Atlantic Tradewind Ocean-Atmosphere Mesoscale Interaction* (EUREC^{4}A/ATOMIC, 2020). After earning her PhD in 2020, Isabel will continue her work on ATOMIC at the University of Miami with Paquita Zuidema as part of her National Oceanic and Atmospheric Administration Climate and Global Change Postdoctoral Fellowship.